FACULTY
OF MATHEMATICS
AND PHYSICS
Charles University

DOCTORAL THESIS

Martina Šimsová

Radiative Processes of Small Molecules

Department of Chemical Physics and Optics

Supervisor of the doctoral thesis:	doc. Ing. Pavel Soldán, Dr.
Study programme:	Physics
Study branch:	Biophysics, Chemical and Macromolecular Physics

Prague 2019

I declare that I carried out this doctoral thesis independently, and only with the cited sources, literature and other professional sources.

I understand that my work relates to the rights and obligations under the Act No. 121/2000 Sb., the Copyright Act, as amended, in particular the fact that the Charles University has the right to conclude a license agreement on the use of this work as a school work pursuant to Section 60 subsection 1 of the Copyright Act.

In ..... date ..... signature of the author

I would like to thank my supervisor doc. Ing. Pavel Soldán, Dr. for his support, time, patience and friendly behaviour towards me throughout all these years. Thank you also for suggesting an interesting topic for my PhD study. I appreciate that you allowed me to go for a six-month practical training and that you recommended prof. Gunnar Nyman from the University of Gothenburg. I am also grateful for your careful reading of the manuscript and suggesting corrections.

Thank you, Gunnar, for accepting me as a trainee in your group and for all your guidance and kind approach. I am thankful for introducing me to prof. Magnus Gustafsson from Luleå University of Technology, who became a part of our project.

Magnus, thank you for suggesting that project and for all your patient help, either through e-mails or Skype, or in person in a 10-day business trip to Luleå University of Technology.

I would like to thank Dr. Wolfgang P. Kraemer for his help that led us to our three articles.

I am blessed to have my dear parents that always stand by my side, whatever happens. I am elated to have you in my life.

Many thanks to my husband, Dan, for always believing in me. I am enormously grateful for your patience in my struggle. I also appreciate that you read my manuscript and suggested improvements.

Title: Radiative Processes of Small Molecules

Author: Martina Šimsová

Department: Department of Chemical Physics and Optics

Supervisor: doc. Ing. Pavel Soldán, Dr., Department of Chemical Physics and Optics

Abstract: Four types of astrochemically relevant radiative processes are studied: bound-bound, bound-free, free-bound and free-free. The former two together determine radiative lifetimes, which are calculated for the $HeLi^+$ molecular ion. Free-bound processes, also called radiative association, are studied on two systems: He in collisions with Li^+, and O in collision with C^+. Collisions of He and Li^+ are believed to have occurred during the recombination era of the Universe, while collisions of O with C^+ are considered to be relevant in SN 1987A. Altogether, 17 radiative association cross sections and rate coefficients are calculated for radiative association, and the effect of a stimulated emission is also illustrated. A free-free process, also called radiative charge transfer, is studied in collisions of He with Li^+.

Keywords: radiative association, radiative charge transfer, radiative lifetimes, $HeLi^+$, CO^+

Contents

Introduction

The Universe has amazed many generations throughout the human history. It started with twinkling stars, the Moon cycle, and the change of a day and night. Nowadays, we know the Universe is enormously huge containing more than just stars, planets and moons. The interstellar space contains **interstellar medium** (ISM) which consists of gas and dust.

This work deals with processes that have occurred in the Universe during the **recombination era**, which had started around 50 000 years after the Bing Bang [1]. During this era, free electrons started to occupy orbital shells of protons and nuclei forming thus stable bound systems. At the beginning of this era, the temperature was around 50 000 K [2], which is less than the first corresponding ionisation energies. The main reason why the formation of stable composed systems did not start at higher temperatures is that the amount of highly energetic photons capable of reionising the complex had been too large [3]. This recombination was accompanied by photon emission through which the Universe cooled down further. Even more cooling was done through the first chemical reactions that could happen with the existence of free neutral atoms, during which more photons were emitted and took away some kinetic energy of the matter. We are talking about emission processes through which temperature dropped to roughly 3 000 K during the recombination era (around 379 000 years after the Bing Bang) when the estimated fraction of neutral hydrogen was 90 % [4]. The studied processes here occurred after the creation of the first neutral He.

The current Universe mainly comprises of hydrogen; nevertheless, at the recombination era, the first stable nucleus-electron system to be formed was cation Li^{2+}. Then it was Li^+ and He^+. The order of formation was given by the ionisation energy that was 122.4 eV, 75.6 eV and 54.4 eV, respectively. After these first three atomic ions, the first neutral atom was created, which was He with the ionisation energy 24.6 eV. Interestingly, the most abundant element, hydrogen in the isotopic forms H and D (deuterium), was formed afterwards because its ionisation energy is 13.6 eV. After hydrogen isotopes, neutral Li with the ionisation energy 5.4 eV was created, but not as a product of the recombination of Li^+ with an electron. Another passages enabled the creation of Li, for instance dissociative electron attachments with $LiHe^+$ or LiH^+ [5].

When He, the first neutral atom, was created, the first chemical reactions could occur, although the bond that was between He and an atomic cation was weaker than the chemical bonds we commonly know today: covalent or ionic (which is often considered as a special case of a covalent bond). It is assumed that the first chemical reaction [5] was

$$\mathrm{He} + \mathrm{H}^+ \rightarrow \mathrm{HeH}^+ + \text{photon}.$$

Another two possible reactions in the recombination era were

$$\mathrm{He} + \mathrm{He}^+ \rightarrow \mathrm{He}_2^+ + \text{photon},$$
$$\mathrm{He} + \mathrm{Li}^+ \rightarrow \mathrm{HeLi}^+ + \text{photon},$$

which were less common in comparison with the first reaction because of the lower abundances of He^+ and Li^+. More examples of possible chemical reactions of the early Universe can be found in [5]. Because the temperature of the Universe was still very high (several thousands of kelvins), it is assumed that the first chemical reactions occurred in electronicly excited states. The emitted photon entails a deexcitation to a lower electronic state.

A deexcitation can occur also in a radiative charge transfer, for example,

$$\mathrm{He} + \mathrm{H}^+ \rightarrow \mathrm{He}^+ + \mathrm{H} + \mathrm{photon},$$

which was the most common radiative charge transfer process in the recombination era and still occurs nowadays. This process is common in ISM and, therefore, is of high astrochemical interest.

Emission processes can occur also in higher layers of atmospheres or cool stars, in comet tails and different interstellar environments. The temperatures in the atmospheres of cool stars are still large, around several thousand kelvins. The temperature of ISM can vary from 10 K up to 1 000 000 K [6].

The coldest are so-called **molecular clouds** or **molecular gas** that can typically have 10 or 20 K. These clouds can support star formation. Clouds that contain **dust grains** are called **dense clouds** [7]. The grains shield their surrounding from harmfull UV or X rays and give rise to the H_2 formation. Mediums with neutral atomic hydrogen have normally temperatures from 50 K to 100 K or from 6 000 K to 10 000 K. The former one is referred to as **cold neutral gas**, the latter as **warm neutral gas**. If species with ionisation energies below 13.6 eV are present in a cold neutral gas, other atoms with lower ionisation potentials are ionised, for example, C^+, Si^+, S^+ or Fe^+ may be present. Such a medium is then called **diffuse cloud** of the temperature around 80 K [7]. Protons can be present in **warm ionised gas** with temperatures around 8 000 K. This is possible in the vicinity of ionising sources. The most of these regions are called **H II regions** like the Orion Nebula or Eagel Nebula. H II regions contain partially ionised gas and star formation still occurs in them. For comparison, the corresponding temperature for the ionisation energy 13.598 4 eV roughly corresponds to 157 803 K. Above this temperature, neutral hydrogen is stable. Temperatures around 1 000 000 K are in the so-called **hot ionised gas**. The above classification can be found in [6] (Table 1 therein) and in [7].

Radiative processes concerning collisions of He and Li^+ are one of the two interests of this thesis. Namely, radiative association of $\mathrm{He}(2^3\mathrm{P}) + \mathrm{Li}^+$, radiative charge transfer in $\mathrm{He}(2^3\mathrm{S}) + \mathrm{Li}^+$, and radiative lifetimes of $\mathrm{HeLi}^+(\mathrm{b}^3\Sigma^+)$. The other interest is the radiative association of $\mathrm{O}(2^3\mathrm{P}) + \mathrm{C}^+(2^2\mathrm{P})$.

Previously, the collisions of He with Li^+ were studied in the continuum of the electronic ground state

$$\mathrm{X}^1\Sigma^+ \left[\mathrm{He}(1^1\mathrm{S}) + \mathrm{Li}^+(1^1\mathrm{S})\right] \rightarrow \mathrm{HeLi}^+(\mathrm{X}^1\Sigma^+) + \mathrm{photon},$$

in [8], where the radiative association of Li with He^+ was also shown. The corresponding He association with H^+ results were shown in [9] and $H+He^+$ process was studied in [10], where the authors explain in their Introduction that the formation of HeH^+ in ISM is believed to happen mainly through this association. Further, radiative association of He with Li^+ was studied also in the continua of electronic excited states

$$
\begin{aligned}
\mathrm{B}^1\Sigma^+\left[\mathrm{He}(2^1\mathrm{S}) + \mathrm{Li}^+(1^1\mathrm{S})\right] &\rightarrow \mathrm{HeLi}^+(\mathrm{X}^1\Sigma^+) + \text{photon},\\
&\rightarrow \mathrm{HeLi}^+(\mathrm{A}^1\Sigma^+) + \text{photon},\\
&\rightarrow \mathrm{HeLi}^+(\mathrm{B}^1\Sigma^+) + \text{photon},\\
\mathrm{b}^3\Sigma^+\left[\mathrm{He}(2^3\mathrm{S}) + \mathrm{Li}^+(1^1\mathrm{S})\right] &\rightarrow \mathrm{HeLi}^+(\mathrm{a}^3\Sigma^+) + \text{photon},\\
&\rightarrow \mathrm{HeLi}^+(\mathrm{b}^3\Sigma^+) + \text{photon},
\end{aligned}
$$

in [11, 12], where the corresponding studies for He+H^+ are also shown. In [12], the transitions when instead of H^+ a deuterium cation, D^+, is present are also shown. In [13], the $\mathrm{b}^3\Sigma^+[\cdots] \rightarrow \mathrm{HeH}^+(\mathrm{a}^3\Sigma^+)$ + photon process was studied together with the opposite process called photodissocation.

Radiative association of He + H^+ through stimulated photon emission was studied for ground-state transitions in [14], where the corresponding cross sections and rate coefficients were shown at several black-body (also called background) temperatures. The stimulated radiative association rate coefficients were obtained also for transitions within the $\mathrm{B}^1\Sigma^+$ state in [11]. For the completeness, the collisions of He with He^+ have been studied, for example, in [15, 16] where also the stimulated emission was taken into account. More about radiative association studies relevant for the early Universe and their detailed summary can be found in [17].

Currently, the most abundant molecule in the known Universe is H_2. The second most abundant is CO and it can occur, for instance, in diffuse molecular clouds [18] or in dense molecular clouds [7]. The ionic form CO^+, the first time detected in the M17SW ISM and NGC 7027 planetary nebula [19], can be present in environments with ionising radiation. Formation of CO and CO^+ by radiative association is believed to be slow in comparison to binary reactions [20]; however, in SN 1987A supernova, the main source of CO formation is the radiative association of C and O atoms [21, 22]. The significance of radiative association

$$\mathrm{O} + \mathrm{C}^+ \rightarrow \mathrm{CO}^+ + \text{photon}$$

in SN 1987A is questionable. It was considered significant [23], where the authors claimed that the rate coefficient of the CO^+ formation by radiative association either by collisions of O with C^+ or by collisions of C with O^+ is around 100 times larger than the rate coefficient for radiative association of neutral C and O. Next year, this route was suggested to be irrelevant in comparison to the C+O radiative association [21] in SN 1987A, which also meant that CO^+ could rather be produced by charge transfer

$$\mathrm{CO} + \mathrm{O}^+ \rightarrow \mathrm{CO}^+ + \mathrm{O}.$$

The radiative association of C and O atoms has been recently studied more thoroughly in the lowest electronic states [24, 25]. On this system, the isotopic effect was computationally studied [26]. More precise rate coefficients for formation of CO^+ by radiative association are, however, missing and we aim to clarify the situation.

The study of lifetimes adds to the final picture of abundances. The radiative lifetimes of $\mathrm{HeH}^+(\mathrm{b}^3\Sigma^+)$ is 1.60×10^{-8} s [27]. During the decay, the molecular ion

deexcitates to $a^3\Sigma^+$, where it is trapped for long time because the transitions to the lower singlet states are spin-forbidden. Correspondingly, the lifetime of the $a^3\Sigma^+$ state through the deexcitation to $X^1\Sigma^+$ is 149 s [28].

The radiative charge transfer process in collisions of He and H^+ has been studied in the continuum of $b^3\Sigma^+$ [29]. After the charge exchange and photon emission, the system finds itself in the continuum of $a^3\Sigma^+$.

This work is devoted specifically to small molecules by which we will always mean **a diatomic system**. The theory described in Chapter 1 is valid for a charged molecule, but it could be generalised for a neutral molecule. In Chapter 2, all the results for radiative association, radiative charge transfer and radiative lifetimes calculations are collected [30, 31, 32, 33, 34].

The radiative association is calculated for the following processes

$$\begin{aligned}
c^3\Sigma^+ \left[He(2^3P) + Li^+(1^1S)\right] &\to HeLi^+(a^3\Sigma^+) + \text{photon},\\
&\to HeLi^+(b^3\Sigma^+) + \text{photon},\\
&\to HeLi^+(c^3\Sigma^+) + \text{photon},\\
&\to HeLi^+(1^3\Pi\ ) + \text{photon},\\
1^3\Pi\ \left[He(2^3P) + Li^+(1^1S)\right] &\to HeLi^+(a^3\Sigma^+) + \text{photon},\\
&\to HeLi^+(b^3\Sigma^+) + \text{photon},\\
&\to HeLi^+(c^3\Sigma^+) + \text{photon},\\
&\to HeLi^+(1^3\Pi\ ) + \text{photon},
\end{aligned}$$

from which the $\Sigma \to \Sigma$ cross sections and rate coefficients were shown in [30] and the $\Pi \to \Sigma$ cross sections and rate coefficients in [31]. In Chapter 2, the results for the $\Sigma \to \Pi$ and $\Pi \to \Pi$ radiative associations are shown too.

The radiative association processes

$$\begin{aligned}
A^2\Pi\ \left[O(2^3P) + C^+(2^2P)\right] &\to CO^+(X^2\Sigma^+) + \text{photon},\\
D^2\Pi\ \left[O(2^3P) + C^+(2^2P)\right] &\to CO^+(A^2\Pi\ ) + \text{photon},\\
&\to CO^+(X^2\Sigma^+) + \text{photon},\\
1^2\Sigma^-\ \left[O(2^3P) + C^+(2^2P)\right] &\to CO^+(A^2\Pi\ ) + \text{photon},\\
C^2\Delta\ \left[O(2^3P) + C^+(2^2P)\right] &\to CO^+(A^2\Pi\ ) + \text{photon},\\
X^2\Sigma^+\ \left[O(2^3P) + C^+(2^2P)\right] &\to CO^+(A^2\Pi\ ) + \text{photon},\\
2^2\Sigma^-\ \left[O(2^3P) + C^+(2^2P)\right] &\to CO^+(A^2\Pi\ ) + \text{photon},
\end{aligned}$$

are studied in [34] for temperatures up to 10 000 K since the relevant temperatures for SN 1987A range from 2 000 K to 10 000 K.

The radiative charge transfer cross sections and rate coefficients for

$$b^3\Sigma^+ \left[He(2^3S) + Li^+(1^1S)\right] \to a^3\Sigma^+ \left[He^+(1^2S) + Li(2^2S)\right] + \text{photon}$$

are shown in [33].

The radiative lifetimes of $HeLi^+(b^3\Sigma^+)$ ro-vibrational bound states with $J = 0, 1, 2$ are published in [32].

1. Theory of Radiative Processes

1.1 Total Hamiltonian

A radiative process is a process accompanied by emission of at least one photon. In this work, we deal with only **one-photon emissions**. Photonic emission is a quantum phenomenon when a system is in its excited state at the beginning and deexcites itself to a lower state while emitting a photon. If this transition is within one electronic state, it is called **ro-vibrational**; if it is between two electronic states, it is called **ro-vibronic**. In a ro-vibronic transition, the frequency of the emitted photon is from radio- (for example, several GHz [35]), through visual-light to ultraviolet spectrum. A radiative ro-vibrational transition has often its photon frequency from infrared or microwave spectrum. Usually, if a system in a particular electronic state has a spin-allowed electronic transition to a lower electronic state, it "prefers" it rather than the ro-vibratonal deexcitation. As it will be shown later, it is due to two reasons: 1. within the one electronic state, the Franck-Condon (FC) overlap is zero because of the orthogonality of its ro-vibrational states; 2. the probability of a transition is cubicly proportionate to the emitted-photon energy.

The following theory can be studied in detail, for instance, in [36, 37, 38]. In quantum mechanics, a system can be in a state $|i\rangle$, where $|i\rangle$ is a state from the Hilbert space for particles and the electromagnetic field; $|i\rangle$ denotes also the state at the beginning of the process in question and it is an eigenstate of the Hamiltonian describing a system comprising from matter and electromagnetic field

$$\hat{H} = \hat{H}_0 + \hat{H}_{\text{int}}, \tag{1.1}$$

$$\hat{H}_0 = \hat{H}_{\text{mol}} + \hat{H}_{\text{EM}}, \tag{1.2}$$

where $\hat{H}_0$ is the unperturbed Hamiltonian taken as a sum of the Hamiltonian for a diatomic molecule $\hat{H}_{\text{mol}}$ and of the Hamiltonian of the electromagnetic field $\hat{H}_{\text{EM}}$. The interaction between the molecule and electromagnetic field is described by the interaction Hamiltonian $\hat{H}_{\text{int}}$.

The molecular Hamiltonian for a diatomic molecule can be expressed in the coordinate system centered in the nuclear center of mass as

$$\hat{H}_{\text{mol}} = \hat{T}_{\text{n}} + \hat{T}_{\text{e}} + \hat{U}_{\text{nn}} + \hat{U}_{\text{ee}} + \hat{U}_{\text{en}}, \tag{1.3}$$

$$\hat{T}_{\text{n}} = -\frac{\hbar^2}{2\mu}\Delta, \tag{1.4}$$

$$\hat{T}_{\text{e}} = -\frac{\hbar^2}{2m_{\text{e}}}\sum_{i=1}^{n_{\text{e}}}\Delta_i, \tag{1.5}$$

$$\hat{U}_{\text{nn}} = \frac{e^2}{4\pi\epsilon_0}\frac{Z_{\text{A}}Z_{\text{B}}}{R}, \tag{1.6}$$

$$\hat{U}_{\text{ee}} = \frac{e^2}{4\pi\epsilon_0}\frac{1}{2}\sum_{i=1}^{n_{\text{e}}}\sum_{j=1,j\neq i}^{n_{\text{e}}}\frac{1}{r_{ij}}, \tag{1.7}$$

$$\hat{U}_{\mathrm{en}} = -\frac{e^2}{4\pi\epsilon_0}\sum_{i=1}^{n_{\mathrm{e}}}\left(\frac{Z_{\mathrm{A}}}{|\mathbf{r}_i - \mathbf{R}_{\mathrm{A}}|} + \frac{Z_{\mathrm{B}}}{|\mathbf{r}_i - \mathbf{R}_{\mathrm{B}}|}\right), \tag{1.8}$$

where $\hat{T}_{\mathrm{n}}$ denotes the operator of the nuclear kinetic energy, $\hat{T}_{\mathrm{e}}$ is the operator of the electronic kinetic energy, $\hat{U}_{\mathrm{nn}}$ is the operator for the repulsive Coulomb interaction between nuclei, $\hat{U}_{\mathrm{ee}}$ is the operator for the repulsive Coulomb interaction between electrons, and $\hat{U}_{\mathrm{en}}$ denotes the operator for the attractive Coulomb interaction between nuclei and electrons. The sums go over n_{e} electrons with the electron mass denoted as m_{e}. For the reduced mass μ it is valid $\mu = M_{\mathrm{A}}M_{\mathrm{B}}/(M_{\mathrm{A}}+M_{\mathrm{B}})$, where M_{A} and M_{B} are the nuclear masses of atom/cation A and B, respectively. Then, R is the internuclear distance, Δ and Δ_i are

$$\Delta = \frac{\partial^2}{\partial X^2} + \frac{\partial^2}{\partial Y^2} + \frac{\partial^2}{\partial Z^2}, \tag{1.9}$$

$$\Delta_i = \frac{\partial^2}{\partial x_i^2} + \frac{\partial^2}{\partial y_i^2} + \frac{\partial^2}{\partial z_i^2}, \tag{1.10}$$

where $\mathbf{R} = \mathbf{R}_{\mathrm{B}} - \mathbf{R}_{\mathrm{A}} = (X, Y, Z)$ is the spatial vector with the length $R = |\mathbf{R}|$. In Equation (1.10), the Laplace operator for electron positions $\mathbf{r}_i = (x_i, y_i, z_i)$ is expressed. The index i here denotes that $\mathbf{r}_i$ is the spatial vector of the i-th electron. Then, $r_{ij} = |\mathbf{r}_i - \mathbf{r}_j|$ is the length of the spatial vector between the i-th and j-th electrons. The length of the spatial vector between the i-th electron and I-th nucleus is $|\mathbf{r}_i - \mathbf{R}_I|$. Lastly, eZ_{A} and eZ_{B} are charges of nuclei A and B, respectively, where Z_I is the atomic number of atom I and e is the elementary charge $e = 1.602\,176\,634 \times 10^{-19}$ C [39].

The Hamiltonian of the electromagnetic field $\hat{H}_{\mathrm{EM}}$ can be expressed as

$$\hat{H}_{\mathrm{EM}} = \int_0^\infty \sum_{\lambda=1}^{2} \hbar\omega \left[\hat{\mathrm{a}}^+(\mathbf{k},\lambda)\hat{\mathrm{a}}(\mathbf{k},\lambda) + \frac{1}{2}\right] \mathrm{d}^3k, \tag{1.11}$$

where ω is photon frequency, $\hat{\mathrm{a}}^+(\mathbf{k},\lambda)$ and $\hat{\mathrm{a}}(\mathbf{k},\lambda)$ are creation and annihilation operators for photons with the wave vector $\mathbf{k}$ and polarisation λ such that

$$\hat{a}(\mathbf{k},\lambda)\,|0\rangle_{\mathrm{EM}} = 0, \tag{1.12}$$

$$\left[\hat{\mathrm{a}}(\mathbf{k}',\lambda'), \hat{\mathrm{a}}^+(\mathbf{k},\lambda)\right] = \delta(\mathbf{k}' - \mathbf{k})\delta_{\lambda'\lambda}. \tag{1.13}$$

Here, $|0\rangle_{\mathrm{EM}}$ denotes the so-called vacuum state, which is the eigenstate of $\hat{H}_{\mathrm{EM}}$ with no photons.

As it has been indicated, the perturbation theory (PT) is used further with the perturbation denoted as the interaction Hamiltonian

$$\hat{H}_{\mathrm{int}} = -\sum_j \frac{q_j}{m_j}\hat{\mathbf{A}}_j \cdot \hat{\mathbf{p}}_j, \tag{1.14}$$

where q_j is the charge of the j-th charged particle (either electron or nucleus), m_j is the mass of the j-th charged particle, $\hat{\mathbf{A}}_j$ is the operator of the electromagnetic vector caused by the j-th charged particle, and $\hat{\mathbf{p}}_j$ is the operator of the momentum of the j-th charged particle. The term proportional to $\hat{\mathbf{A}}_j^2$ is neglected here.

For the earlier mentioned state $|i\rangle$, we can write an unperturbed state $|i\rangle^{(0)} = |i\rangle_{\text{mol}} |i\rangle_{\text{EM}}$ that is the eigenstate of Hamiltonian (1.2), $\hat{H}_0$. The $|i\rangle_{\text{mol}}$ state is the eigenstate of $\hat{H}_{\text{mol}}$ in Equation (1.3). This state can be expressed also in the coordinate representation through $\Psi_i(\mathbf{R}, \mathbf{r}) = \langle \mathbf{R}, \mathbf{r} | i \rangle_{\text{mol}}$. Lastly, $|i\rangle_{\text{EM}}$ is the eigenstate of $\hat{H}_{\text{EM}}$ in Equation (1.11).

1.2 Electromagnetic Hamiltonian

The operator of the electromagnetic vector can be expressed for the j-th charged particle (either electron or nucleus) as

$$\hat{\mathbf{A}}_j = \sqrt{\frac{\hbar}{2\epsilon_0 \omega V}} \sum_{\lambda=1}^{2} \mathbf{e}(\mathbf{k}, \lambda) \left[e^{i\mathbf{k}\cdot\mathbf{r}_j} \hat{\text{a}}^+(\mathbf{k}, \lambda) + e^{-i\mathbf{k}\cdot\mathbf{r}_j} \hat{\text{a}}(\mathbf{k}, \lambda) \right], \tag{1.15}$$

where $\mathbf{e}(\mathbf{k}, \lambda)$ is the polarisation vector in the direction perpendicular to the wave vector $\mathbf{k}$; thus, $\mathbf{e}(\mathbf{k}, \lambda) \cdot \mathbf{k} = 0$; then, $|\mathbf{e}(\mathbf{k}, \lambda)| = 1$ and $\mathbf{e}(\mathbf{k}, 1) \cdot \mathbf{e}(\mathbf{k}, 2) = 0$, where 1, 2 represent different photon polarisations. V denotes the normalisation volume. We will now use

$$\begin{aligned} \left[\hat{H}_{\text{mol}}, \mathbf{r}_k \right] &= \left[\sum_{j=1}^{n_{\text{e}}+2} \frac{\hat{\mathbf{p}}_j^2}{2m_j} + \hat{U}_{\text{ee}} + \hat{U}_{\text{nn}} + \hat{U}_{\text{en}}, \mathbf{r}_k \right] = \\ &= \frac{1}{2m_k} 2(-i\hbar)\hat{\mathbf{p}}_k = -\frac{i\hbar}{m_k} \hat{\mathbf{p}}_k \end{aligned} \tag{1.16}$$

for the k-th particle, where $n_{\text{e}} + 2$ denotes the sum is over the number of electrons and nuclei, which in the case of a diatomic system means the number of nuclei is 2. After substituting it into Equation (1.14), we get

$$\hat{H}_{\text{int}} = -\frac{i}{\hbar} \sqrt{\frac{\hbar}{2\epsilon_0 \omega V}} \sum_{j,\lambda} \mathbf{e}(\mathbf{k}, \lambda) \left[e^{i\mathbf{k}\cdot\mathbf{r}_j} \hat{\text{a}}^+(\mathbf{k}, \lambda) + e^{-i\mathbf{k}\cdot\mathbf{r}_j} \hat{\text{a}}(\mathbf{k}, \lambda) \right] \cdot \left[\hat{H}_{\text{mol}}, \mathbf{r}_j \right] q_j. \tag{1.17}$$

In the following, we will do several steps at a time:

- Use the **dipole approximation** valid for $\mathbf{k} \cdot \mathbf{r}_j \ll 1$ (i.e. $2\pi |r_j|/\lambda \ll 1$, λ is the wavelength of the photon),

$$e^{\pm i\mathbf{k}\cdot\mathbf{r}_j} = 1; \tag{1.18}$$

- Use the definition of the dipole-moment operator

$$\hat{\mathbf{d}} = Z_{\text{A}} e \mathbf{R}_{\text{A}} + Z_{\text{B}} e \mathbf{R}_{\text{B}} + \sum_{i=1}^{n_{\text{e}}} (-e) \mathbf{r}_i; \tag{1.19}$$

- Realise that $\hat{H}_{\text{mol}}$ commutes with $\hat{\text{a}}^+(\mathbf{k}, \lambda)$, $\hat{\text{a}}(\mathbf{k}, \lambda)$ and $\mathbf{e}(\mathbf{k}, \lambda)$.

Therefore,

$$\hat{H}_{\text{int}} = -i\sqrt{\frac{1}{2\epsilon_0\hbar\omega V}}\sum_{\lambda}\left[\hat{H}_{\text{mol}}, \mathbf{e}(\mathbf{k},\lambda)\cdot\hat{\mathbf{d}}\right]\left[\hat{\text{a}}^{+}(\mathbf{k},\lambda)+\hat{\text{a}}(\mathbf{k},\lambda)\right]. \tag{1.20}$$

A time-dependent wave function that describes a molecule in electromagnetic field and their mutual interaction can be written as a linear combination

$$|i\rangle = \sum_{i}\sum_{k,l} c_{i;k,l}\,|i\rangle_{\text{mol}}\,|k,l\rangle_{\text{EM}}\,e^{-\frac{i}{\hbar}E_i t}e^{-i\omega(k+l+1)t}, \tag{1.21}$$

where E_i is the eigenvalue of $\hat{H}_{\text{mol}}$, $\hbar\omega(k+l+1)$ is the eigenvalue of $\hat{H}_{\text{EM}}$ for a state of k photons with polarisation α and l photons with polarisation β. In other words,

$$\hat{H}_{\text{EM}}\,|k,l\rangle_{\text{EM}} = \left[\left(k+\frac{1}{2}\right)+\left(l+\frac{1}{2}\right)\right]\hbar\omega\,|k,l\rangle_{\text{EM}}\,. \tag{1.22}$$

We will multiply the time-dependent Schrödinger equation

$$i\hbar\frac{\partial\,|i\rangle}{\partial t} = \hat{H}\,|i\rangle\,, \tag{1.23}$$

from the left by $\langle f| = {}_{\text{EM}}\langle m,n|\,{}_{\text{mol}}\langle f|$ and get

$$\begin{aligned} i\hbar\dot{c}_{f;m,n} = &-i\sqrt{\frac{1}{2\epsilon_0\hbar\omega V}}\sum_{i}(E_f-E_i)e^{-i\frac{E_i-E_f}{\hbar}t}\times \\ &\times\Big[{}_{\text{mol}}\langle f|\,\mathbf{e}(\mathbf{k},1)\cdot\hat{\mathbf{d}}\,|i\rangle_{\text{mol}}\left(c_{i;m-1,n}\sqrt{m}e^{i\omega t}+c_{i;m+1,n}\sqrt{m+1}e^{-i\omega t}\right)+ \\ &+{}_{\text{mol}}\langle f|\,\mathbf{e}(\mathbf{k},2)\cdot\hat{\mathbf{d}}\,|i\rangle_{\text{mol}}\left(c_{i;m,n-1}\sqrt{n}e^{i\omega t}+c_{i;m,n+1}\sqrt{n+1}e^{-i\omega t}\right)\Big]\,. \end{aligned} \tag{1.24}$$

The first two terms in the round brackets correspond to the emission and the absorption for $\lambda = 1$ polarisation. The following two terms in the other round brackets correspond to the emission and absorption of photons with the other polarisation.

In this work, we are only interested in emission. Hence we will omit the absorption terms. We will also focus only on one polarisation. The same result we would get for the other polarisation. The equation can be solved with an empirical ansatz

$$c^{(0)}_{i;f} = \delta_{if}e^{-\Gamma_i^{'}t}, \tag{1.25}$$

where $\Gamma_i^{'}$ is an empirical constant for the initial state and it is practically the radiative width $\Gamma_i = 2\hbar\Gamma_i^{'}$, properly discussed later. Now, we will also define

$$\omega_{if} = \frac{E_i - E_f}{\hbar} \tag{1.26}$$

and write the solution

$$c_{f;m+1} = \sqrt{\frac{1}{2\epsilon_0\hbar\omega V}}\omega_{if}\sqrt{m+1}\,{}_{\text{mol}}\langle f|\,\mathbf{e}(\mathbf{k},1)\cdot\hat{\mathbf{d}}\,|i\rangle_{\text{mol}}\,\frac{e^{-i\left[(\omega_{if}-\omega)+\Gamma_i^{'}\right]t}-1}{-i(\omega_{if}-\omega)-\Gamma_i^{'}}. \tag{1.27}$$

Several steps were skipped between Equation (1.23) and Equation (1.27) (see [37]).

The probability to find a molecule in $|f\rangle_{\text{mol}}$ at t, when at $t = 0$ it was in $|i\rangle_{\text{mol}}$, is

$$|c_{f;m+1}|^2 = \frac{\left|{}_{\text{mol}}\langle f|\, \mathbf{e}(\mathbf{k},1)\cdot\hat{\mathbf{d}}\,|i\rangle_{\text{mol}}\right|^2 (m+1)}{2\epsilon_0\hbar\omega V}\frac{\omega_{if}^2}{(\omega_{if}-\omega)^2+(\Gamma_i')^2}, \tag{1.28}$$

where we can recognise the **Cauchy distribution** (also called Lorentzian function).

If we are interested in the probability regardless the angle of the emission, we need to integrate over the angular part:

$$\frac{1}{4\pi}\int_{\phi=0}^{2\pi}\int_{\theta=0}^{\pi}(|\mathbf{e}(\mathbf{k},\alpha)||\mathbf{d}_{fi}|\cos\theta)^2\sin\theta\mathrm{d}\theta\mathrm{d}\phi = \frac{d_{fi}^2}{3}, \tag{1.29}$$

where d_{fi} is the length of the dipole-moment matrix element

$$\mathbf{d}_{fi} = {}_{\text{mol}}\langle f|\,\hat{\mathbf{d}}\,|i\rangle_{\text{mol}}\,. \tag{1.30}$$

Then, the average power of an ensemble of photons with the wave vector $\mathbf{k}$ and polarisation $\lambda = 1$ is

$$\overline{|c_{f;m+1}|^2} = \langle|c_{f;m+1}|^2\rangle = \frac{d_{fi}^2(m+1)}{6\epsilon_0\hbar\omega V}\frac{\omega_{if}^2}{(\omega_{if}-\omega)+(\Gamma_i')^2}. \tag{1.31}$$

Further, we are interested in the probability of an emission regardless the wave vector and polarisation. The number of modes $N(\omega)$ and the energy density per volume unit $\rho(\omega)$ of m photons can be expressed as

$$N(\omega) = \frac{V\omega^2}{\pi^2c^3}, \tag{1.32}$$

$$\rho(\omega) = N(\omega)\frac{\hbar\omega m}{V}, \tag{1.33}$$

which assumes the homogenous diversity of energy among the modes. The total radiation probability for $i \to f$ at ω frequency is then

$$P_{i\to f}(\omega) = \overline{|c_{f;m+1}|^2}N(\omega) = \left[\frac{d_{fi}^2}{6\epsilon_0(\hbar\omega)^2}\rho(\omega) + \frac{d_{fi}^2\omega}{6\epsilon_0\hbar\pi^2c^3}\right]\frac{\omega_{if}^2}{(\omega_{if}-\omega)^2+(\Gamma_i')^2}. \tag{1.34}$$

The average probability per second for $i \to f$ is then

$$\frac{\mathrm{d}\bar{P}_{i\to f}}{\mathrm{d}t} = \frac{1}{\tau_i}\int_0^\infty P_{i\to f}(\omega)\mathrm{d}\omega, \tag{1.35}$$

where $\tau_i = \hbar/\Gamma_i$ is the radiative lifetime of the initial state, properly discussed later. During the integration, it is assumed for narrow spectroscopic lines that $\omega = \omega_{if}$ except for the factor

$$\int_0^\infty \frac{\mathrm{d}\omega}{(\omega_{if}-\omega)^2+(\Gamma_i')^2}. \tag{1.36}$$

After integrating the last equation over ω, we can write for the average probability per second for $i \to f$

$$\frac{\mathrm{d}\bar{P}_{i\to f}}{\mathrm{d}t} = \frac{\pi d_{fi}^2}{3\epsilon_0 \hbar^2}\rho(\omega_{if}) + \frac{d_{fi}^2}{3\epsilon_0 \hbar \pi}\left(\frac{\omega_{if}}{c}\right)^3. \tag{1.37}$$

From the last equation, one can determine the **Einstein A coefficient** for the spontaneous emission

$$A_{i,f} = \frac{1}{4\pi\epsilon_0}\frac{4}{3\hbar}p_i\left(\frac{\omega_{if}}{c}\right)^3 \left|{}_{\mathrm{mol}}\langle f|\hat{\mathbf{d}}|i\rangle_{\mathrm{mol}}\right|^2. \tag{1.38}$$

As we can see, the transition probability of the spontaneous emission depends on an interplay of the cubic frequency of the emitted photon ω_{if} and the squared (transition) dipole-moment element. The last undefined quantity, p_i, is the probability of approach in the given initial electronic state

$$p_i = \frac{(2S+1)(2-\delta_{0,\Lambda})}{(2L_{\mathrm{A}}+1)(2S_{\mathrm{A}}+1)(2L_{\mathrm{B}}+1)(2S_{\mathrm{B}}+1)}, \tag{1.39}$$

where $(2S+1)$ and Λ are the multiplicity and the projection of the electronic angular momentum of the initial electronic state; in the denominator lower indices A and B denote two atoms in a diatomic system AB. Then, L_{A} and L_{B} are atomic orbital quantum momenta, S_{A} and S_{B} are atomic spin quantum momenta. Further, $A_{i,f}$ is expressed here only for **dipole-moment transitions**. Throughout the whole work we will only deal with dipole-moment transitions.

Stimulated emission is described by the **Einstein B coefficient** for the stimulated emission

$$B_{i,f} = \frac{\pi d_{fi}^2}{3\epsilon_0\hbar^2}\frac{1}{2\pi} = \frac{\pi}{2\hbar}\left(\frac{c}{\omega_{if}}\right)^3\frac{p_f}{p_i}A_{f,i} \tag{1.40}$$

between an initial state i and a final state f that can be determined also from Equation (1.37). If $E_i < E_f$, $B_{i,f}$ is the coefficient for absorption. The Einstein B coefficient has units of volume/energy/(time)^2 and the Einstein A coefficient has units of 1/time.

1.3 Molecular Hamiltonian

Molecular systems are often treated within the so-called **Born-Oppenheimer** (BO) **approximation**. This approach takes into account the large mass differences between nuclei and electrons. Hence nuclear configuration can be considered fixed while the electronic movement is solved. Mathematically expressed, we can write

$$|i\rangle_{\mathrm{mol}} = |i\rangle_{\mathrm{n}}\,|i\rangle_{\mathrm{e}} \tag{1.41}$$

$$\Psi(\mathbf{R},\mathbf{r}) = \Psi(\mathbf{R})\psi(\mathbf{r};\mathbf{R}), \tag{1.42}$$

$$= \langle\mathbf{R},\mathbf{r}|i\rangle_{\mathrm{mol}} = \langle\mathbf{R}|i\rangle_{\mathrm{n}}\,\langle\mathbf{r};\mathbf{R}|i\rangle_{\mathrm{e}}\,, \tag{1.43}$$

where in $\psi(\mathbf{r};\mathbf{R})$ $\mathbf{R}$ is a parameter, and solve the Schrödinger equation of a diatomic system separately for electrons

$$\left[\hat{T}_\mathrm{e} + \hat{U}_\mathrm{ee} + \hat{U}_\mathrm{en} + \hat{U}_\mathrm{nn}\right]\psi(\mathbf{r};\mathbf{R}) = V(R)\psi(\mathbf{r};\mathbf{R}), \tag{1.44}$$

where $\hat{T}_\mathrm{e}$ is the operator of the kinetic energy of electrons from Equation (1.5), $\hat{U}_\mathrm{ee}$ is the operator of the potential energy from all electrons from Equation (1.7), $\hat{U}_\mathrm{en}$ is the operator of the potential energy from the interaction between electrons and nuclei from Equation (1.8), and $\hat{U}_\mathrm{nn}$ is the operator of the potential energy between the two nuclei of a diatomic system from Equation (1.6). This term is a constant at fixed R and can be, therefore, neglected in computations and added later. **Absolute energies** $V(R)$ are the eigenvalues and $\psi(\mathbf{r};\mathbf{R})$ the eigenfunctions of Equation (1.44) at the internuclear distance R.

After solution of Equation (1.44) within one electronic state, the Schrödinger equation for nuclei (Hund's case (a)) can be solved in the spherical coordinates [40]

$$\left[-\frac{\hbar^2}{2\mu}\frac{\mathrm{d}^2}{\mathrm{d}R^2} + \frac{\hbar^2}{2\mu}\frac{\left(\hat{\mathbf{J}} - \hat{\mathbf{L}} - \hat{\mathbf{S}}\right)^2}{R^2} + U(R)\right]\Psi(\mathbf{R}) = E\Psi(\mathbf{R}), \tag{1.45}$$

where $U(R) = V(R) - V(R \to \infty)$ are the **interaction energies**, $\hat{\mathbf{J}}$ is the operator for the total angular momentum, $\hat{\mathbf{L}}$ is the operator for the electronic angular momentum and $\hat{\mathbf{S}}$ is the operator for the electronic spin. After diagonalisation of the $\left(\hat{\mathbf{J}} - \hat{\mathbf{L}} - \hat{\mathbf{S}}\right)^2$ operator matrix in the spherical harmonics, i.e. expressing $\Psi(\mathbf{R}) = \Psi_{J,\Omega}(R)Y_{J,\Omega}(\Theta,\phi)$, multiplying Equation (1.45) by $Y^*_{J',\Omega'}(\Theta,\phi)$ from the left-hand side and integrating through Θ,ϕ, we get a nonzero result only for $J' = J$ and $\Omega' = \Omega$

$$\left[-\frac{\hbar^2}{2\mu}\frac{\mathrm{d}^2}{\mathrm{d}R^2} + \frac{\hbar}{2\mu}\frac{J(J+1) - \Omega^2}{R^2} + U(R)\right]\Psi_{J,\Omega}(R) = E\Psi_{J,\Omega}(R), \tag{1.46}$$

where J is the rotational quantum number and Ω is the quantum number for the projection of the total electronic angular momentum. The solutions of Equation (1.46), $\Psi_{J,\Omega}(R)$, are not only bound states $\psi_{v,J,\Omega}(R)$ but also continuum states $\chi_{E,J,\Omega}(R)$. A bound state entails a molecule: a bound pair of atoms. A continuum state entails two unbound atoms with the kinetic energy E. Both states can be characterised also by the principal quantum number and electronic spin, but in this work the electronic state will be always specified and, therefore, these quantum numbers will be omitted.

Equation (1.42) does not provide a good description when the BO approximation fails at some internuclear distances. Then, the system does not follow adiabates, but diabates for which the **diabatic representation** is needed. In diatomic molecules, this is usually around **avoided crossings**. One avoided crossing is illustrated between two electronic states $\mathrm{D}^2\Pi$ and $3^2\Pi$ of CO^+ in Figure 1.1. These two states have different dissociation limits. Another electronic state of the same symmetry, $\mathrm{A}^2\Pi$, is shown, too, with the same dissociation limit as $\mathrm{D}^2\Pi$. The red, blue and green lines are adiabates. If around the avoided crossing between the $\mathrm{D}^2\Pi$ and $3^2\Pi$ PECs a system from $\mathrm{D}^2\Pi$ with decreasing R (in the approach of C and O^+)"decides" to follow the $3^2\Pi$ PEC, we say it follows a

Figure 1.1: Three potential energy curves for CO^+ are shown two of which, $D^2\Pi$ and $3^2\Pi$, exhibit an avoided crossing. The lowest state is $A^2\Pi$, which has the same dissociation limit as $D^2\Pi$.

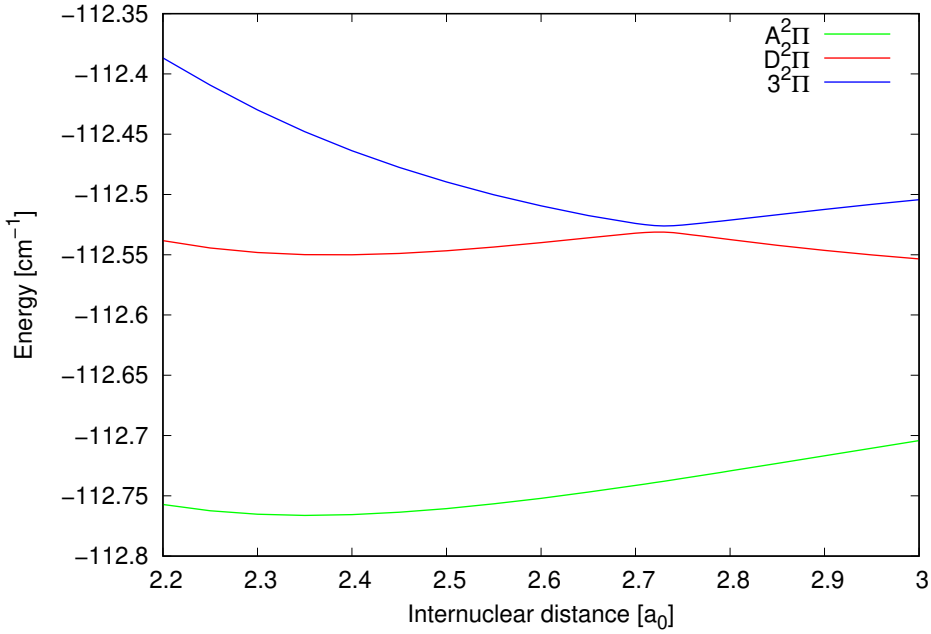

diabate. In such a case, the diabatic approximation is more suitable. For more details see, for instance, [41]. Here, however, the diabatic representation is not used, but rather a quasidiabatic approximation where the PEC in question is combined from the BO curves. The corresponding TDM is calculated from the made-up diabate. In this work, we do not deal with spin-forbidden transitions; therefore, the avoided crossings of our interest are those between two electronic states of the same spin and the same electronic symmetry as it is illustrated in Figure 1.1.

The asymptotic difference of the absolute energies between two electronic states i and f,

$$\Delta E = V_i(R \to \infty) - V_f(R \to \infty) \tag{1.47}$$

will be called here the energy difference between the dissociation limits. This difference ΔE is also illustrated in Figure 1.2 on a $HeLi^+$ system between its two dissociation limits $V_\mathrm{a}(R \to \infty)$ and $V_\mathrm{b}(R \to \infty)$ of the $a^3\Sigma^+$ and $b^3\Sigma^+$ states. In this case, $V_\mathrm{a}(R)$ is equal to the interaction energy $U_\mathrm{a}(R)$ because we set $V_\mathrm{a}(R \to \infty) = 0$. For the processes occurring within one electronic state, $\Delta E = 0$, the same holds for the processes between electronic states with the same dissociation limit.

1.4 Interatomic Interactions

In the previous Section, we have shortly mentioned interaction energies $U(R)$ for which $U(R \to \infty) = 0$. Interaction energy is a difference between the R-dependent

Figure 1.2: Potential energy curves are illustrated of two lowest electronic states of $HeLi^+$ with the $^3\Sigma^+$ symmetry, $a^3\Sigma^+$ and $b^3\Sigma^+$, together with their dissociation limits. The asymptotic energy difference ΔE between them is depicted, too.

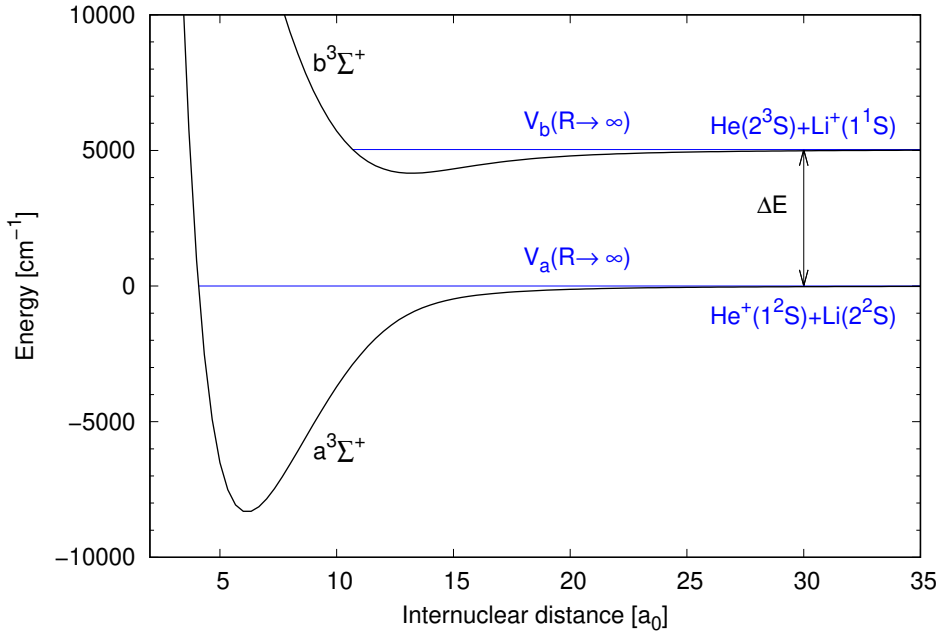

energy of the system AB and energies of the isolated non-interacting A and B. Mathematically expressed,

$$U(R) = E_{\mathrm{AB}}(R) - (E_{\mathrm{A}} + E_{\mathrm{B}})\,, \tag{1.48}$$

where E_{A} and E_{B} are atomic energies. In Figure 1.2, A and B are He and Li^+.

At large R, He and Li^+ experience attractive forces in their collision. They interact together through their electromagnetic fields. At the beginning of their approach, the attractive long-range forces prevail. We are simply discussing the "classical movement" on a PEC. If we try to move Li^+ closer to He than when the PEC has its minimum, they start to repulse each other. This region is called short range and the larger force comes from the so-called electronic exchange energy, which rises due to the increasing overlap of electronic orbitals.

Interaction energies and values of the (transition) dipole-moment vector function can be computed at $R_i, i = 1, 2, \ldots, M$. For $R > R_M$, $U(R)$ is extrapolated (explained in Subsection 1.7.1). For that, we need to know the general behaviour at long range. We follow here the approach of [42, 43].

In order to find the long-range behaviour, we need to look at Equation (1.44) and devide the Hamiltonian $\hat{H} = \hat{H}_0 + \hat{H}_{\mathrm{int}}^{\mathrm{AB}}$ into

$$\hat{H}_0 = \hat{H}_{\mathrm{A}} + \hat{H}_{\mathrm{B}}, \tag{1.49}$$

$$\hat{H}_{\mathrm{A}} = \frac{e^2}{4\pi\epsilon_0}\frac{1}{2}\sum_{a,c=1}^{n_{\mathrm{A}}}\frac{1}{r_{ac}} - \frac{e^2}{4\pi\epsilon_0}\sum_{a=1}^{n_{\mathrm{A}}}\frac{Z_{\mathrm{A}}}{|\mathbf{r}_a - \mathbf{R}_{\mathrm{A}}|}, \tag{1.50}$$

$$\hat{H}_{\mathrm{B}} = \frac{e^2}{4\pi\epsilon_0}\frac{1}{2}\sum_{b,d=1}^{n_{\mathrm{B}}-1}\frac{1}{r_{bd}} - \frac{e^2}{4\pi\epsilon_0}\sum_{i=1}^{n_{\mathrm{B}}-1}\frac{Z_{\mathrm{B}}}{|\mathbf{r}_b - \mathbf{R}_{\mathrm{B}}|}, \tag{1.51}$$

$$\hat{H}_{\text{int}}^{\text{AB}} = \frac{e^2}{4\pi\epsilon_0}\sum_{a=1}^{n_{\text{A}}}\sum_{b=1}^{n_{\text{B}}-1}\frac{1}{r_{ab}} + \frac{e^2}{4\pi\epsilon_0}\frac{Z_{\text{A}}Z_{\text{B}}}{|\mathbf{R}_{\text{A}}-\mathbf{R}_{\text{B}}|} - \\ - \frac{e^2}{4\pi\epsilon_0}\left(\sum_{a=1}^{n_{\text{A}}}\frac{Z_{\text{B}}}{|\mathbf{r}_a-\mathbf{R}_{\text{B}}|} + \sum_{b=1}^{n_{\text{B}}-1}\frac{Z_{\text{A}}}{|\mathbf{r}_b-\mathbf{R}_{\text{A}}|}\right), \tag{1.52}$$

where $\hat{H}_{\text{A}}$ is the electronic Hamiltonian for atom A, $r_{ac} = |\mathbf{r}_a - \mathbf{r}_c|$ is the spatial vector between the a-th and c-th electrons of the total number of n_{A} electrons, $Z_{\text{A}}e$ and $-e$ are the charges of the nucleus ($Z_{\text{A}} = n_{\text{A}}$) and electrons on atom A, $|\mathbf{r}_a - \mathbf{R}_{\text{A}}|$ is the spatial vector between the a-th electron and the nucleus A; $\hat{H}_{\text{B}}$ is the electronic Hamiltonian for atomic cation B, from which one electron is missing. The total number of electrons is denoted $n_{\text{B}}-1$. Similarly, it can be expressed for r_{bd}, $|\mathbf{r}_b - \mathbf{R}_{\text{B}}|$, r_{ab}, $|\mathbf{r}_a - \mathbf{R}_{\text{B}}|$ and $|\mathbf{r}_b - \mathbf{R}_{\text{A}}|$. The interaction Hamiltonian between atom A and atomic cation B is denoted $\hat{H}_{\text{int}}^{\text{AB}}$. In the following, the retardation effects are neglected.

1.4.1 Perturbation Theory

In the following, PT is used. For Hamiltonian (1.49), it is valid

$$\hat{H}_0\,|m,n\rangle = \hat{H}_0\,|m\rangle\otimes|n\rangle = \hat{H}_{\text{A}}\,|m\rangle\otimes|n\rangle + |m\rangle\otimes\hat{H}_{\text{B}}\,|n\rangle\,, \\ = \left(E_m^{\text{A}} + E_n^{\text{B}}\right)|m,n\rangle\,. \tag{1.53}$$

Here, $|m,n\rangle = |m\rangle\otimes|n\rangle$ denotes eigenstates of unperturbed electronic Hamiltonian (1.49). Then, at long distances, where the exchange energy can be neglected, the interaction energy can be approximated by the expression [42]

$$U(R) = \epsilon_{\text{el}}^{(1)}(R) + \sum_{n=2}^{\infty}\left[\epsilon_{\text{ind}}^{(n)}(R) + \epsilon_{\text{disp}}^{(n)}(R)\right] + \sum_{n=3}^{\infty}\epsilon_{\text{ind.disp}}^{(n)}(R), \tag{1.54}$$

where the first term is the first order term of PT and corresponds to multipole-multipole electrostatic energy. From the second and higher orders, one obtains the **induction energy** $\epsilon_{\text{ind}}^{(n)}(R)$ and **dispersion energy** $\epsilon_{\text{disp}}^{(n)}(R)$. The induction energy comes from the interaction between polarised electron clouds that can be imagined easier than the dispersion energy whose origin is purely quantal. The dispersion energy is usually explained as quantal fluctuations of electron density. The last sum in Equation (1.54) is a mixture of induction and dispersion energies and starts from the third order of PT. In this work, the second order will be used; thus, the expression for $\epsilon_{\text{ind.disp}}^{(n)}(R)$ will be not shown here.

First Order of Perturbation Theory

The electrostatic energy of the first order of PT, $\epsilon_{\text{el}}^{(1)}(R)$, in a ground state $|00\rangle$ can be expressed as

$$\epsilon_{\text{el}}^{(1)}(R) = \langle 00|\hat{H}_{\text{int}}^{\text{AB}}|00\rangle\,. \tag{1.55}$$

The interaction Hamiltonian, $\hat{H}_{\text{int}}^{\text{AB}}$ is in PT expanded into Taylor series in powers of $1/R$ [43]

$$\hat{H}_{\text{int}}^{\text{AB}} = \hat{T} q_{\text{A}} q_{\text{B}} + \hat{T}_{\alpha}(q_{\text{B}} \hat{d}_{\alpha}^{\text{A}} - \hat{d}_{\alpha}^{\text{B}} q_{\text{A}}) + \tag{1.56}$$
$$+ \hat{T}_{\alpha\beta}\left(\frac{1}{3} q_{\text{A}} \hat{Q}_{\alpha\beta}^{\text{B}} - \hat{d}_{\alpha}^{\text{A}} \hat{d}_{\beta}^{\text{B}} + \frac{1}{3} \hat{Q}_{\alpha\beta}^{\text{A}} q_{\text{B}}\right) + \cdots ,$$
$$\hat{T}_{\alpha\beta\ldots\nu}^{(n)} = \frac{1}{4\pi\epsilon_0} \Delta_{\alpha}\Delta_{\beta}\ldots\Delta_{\nu}\frac{1}{R}, \tag{1.57}$$

where $\hat{d}_{\alpha}^{\text{A}}$ is the α-component of the dipole moment operator for electronic cloud at atom A ($\alpha = x, y$ or z)

$$\hat{\mathbf{d}}^{\text{A}} = \sum_{i=1}^{n_{\text{A}}} (-e)\mathbf{r}_i. \tag{1.58}$$

Similarly, it can be expressed for atomic cation B

$$\hat{\mathbf{d}}^{\text{B}} = \sum_{i=1}^{n_{\text{B}}-1} (-e)\mathbf{r}_i. \tag{1.59}$$

Further, in Equation (1.57), $\hat{Q}_{\alpha\beta}^{\text{A}}$ is the α, β-component for the operator for the quadrupole moment on atom A

$$\hat{Q}_{\alpha\beta}^{\text{A}} = \frac{1}{2}\sum_{i=1}^{n_A} q_i (3 r_{\alpha}^{i} r_{\beta}^{i} - r^2 \delta_{\alpha,\beta}), \tag{1.60}$$

which is a tensor of rank 2. Lastly,

$$\hat{T} = \frac{1}{4\pi\epsilon_0}\frac{1}{R}, \tag{1.61}$$
$$\hat{T}_{\alpha} = -\frac{1}{4\pi\epsilon_0}\frac{R_{\alpha}}{R^3}, \tag{1.62}$$
$$\hat{T}_{\alpha\beta} = \frac{1}{4\pi\epsilon_0}\frac{3R_{\alpha}R_{\beta} - R^2\delta_{\alpha\beta}}{R^5}. \tag{1.63}$$

For the electrostatic energy, we can now write

$$\epsilon_{\text{el}}^{(1)}(R) = \langle 00|\hat{H}_{\text{int}}^{\text{AB}}|00\rangle , \tag{1.64}$$
$$= \frac{1}{4\pi\epsilon_0}\left[\frac{q_{\text{A}} q_B}{R} + \frac{q_{\text{A}}(\mathbf{d}^{\text{B}}\cdot\mathbf{R}) - q_{\text{B}}(\mathbf{d}^{\text{A}}\cdot\mathbf{R})}{R^3} + \frac{\mathbf{d}^{\text{A}}\cdot\mathbf{d}^{\text{B}}}{R^3} - \right.$$
$$\left. - \frac{3(\mathbf{d}^{\text{A}}\cdot\mathbf{R})(\mathbf{d}^{\text{B}}\cdot\mathbf{R})}{R^5} + \cdots\right], \tag{1.65}$$

where q_{A}, q_{B} denote charges on A and B atoms/ions; and $\mathbf{d}^{\text{A}}$, $\mathbf{d}^{\text{B}}$ are dipole moments for atom A and atomic cation B only in a specific electronic state (here it is in the ground state $|0\rangle$), respectively, where

$$\mathbf{d}^{\text{A}} = \langle 00|\hat{\mathbf{d}}^{\text{A}}|00\rangle = \langle 0|\hat{\mathbf{d}}^{\text{A}}|0\rangle \otimes \langle 0|0\rangle = \langle 0|\hat{\mathbf{d}}^{\text{A}}|0\rangle . \tag{1.66}$$

The first term in Equation (1.65) is the monopole-monopole interaction or the Coulomb interaction between A and B; the second term is the monopole-dipole interaction; the fourth and fifth terms are the dipole-dipole interactions, etc.

For an atom A and atomic cation B, however, the atomic permanent dipole moments $\mathbf{d}^{\mathrm{A}}$ and $\mathbf{d}^{\mathrm{B}}$ are zero and $q_{\mathrm{A}} = 0$, $q_{\mathrm{B}} = e$, the first order of PT can be expressed as

$$\begin{aligned}\epsilon_{\mathrm{el}}^{(1)}(R) &= \frac{1}{4\pi\epsilon_0} q_{\mathrm{B}} \sum_{\alpha,\beta} \langle 00| \hat{Q}^{\mathrm{A}}_{\alpha,\beta} |00\rangle \frac{R_\alpha R_\beta}{R^5} + \cdots , \\ &= \frac{1}{4\pi\epsilon_0} \frac{e}{R^3} \langle 00| \hat{Q}^{\mathrm{A}}_{zz} |00\rangle + \cdots , \end{aligned} \tag{1.67}$$

where the only nonzero value is for $\alpha = \beta = z$ because $\mathbf{R} = (0, 0, R)$. In this work, S- and P-atoms are studied. For S-atoms, the quadrupole moment is zero, and for P-atoms, it is nonzero.

Second Order of Perturbation Theory

The second order of PT contains, as shown in Equation (1.54), induction and dispersion energy. The induction energy can stem from inducing polarisation on atom A by atom B or vice versa. Mathematically expressed, the energy correction of the 2nd order to the ground state $|00\rangle$ [43]:

$$\epsilon^{(2)}(R) = -\sum_{k,l}{}' \frac{\langle 00|\hat{H}^{\mathrm{AB}}_{\mathrm{int}}|kl\rangle \langle kl|\hat{H}^{\mathrm{AB}}_{\mathrm{int}}|00\rangle}{E^{\mathrm{A}}_k + E^{\mathrm{B}}_l - E^{\mathrm{A}}_0 - E^{\mathrm{B}}_0}, \tag{1.68}$$

$$\epsilon^{(2)}_{\mathrm{ind-A}}(R) = -\sum_{k\neq 0} \frac{\langle 00|\hat{H}^{\mathrm{AB}}_{\mathrm{int}}|k0\rangle \langle k0|\hat{H}^{\mathrm{AB}}_{\mathrm{int}}|00\rangle}{E^{\mathrm{A}}_k - E^{\mathrm{A}}_0}, \tag{1.69}$$

$$\epsilon^{(2)}_{\mathrm{ind-B}}(R) = -\sum_{l\neq 0} \frac{\langle 00|\hat{H}^{\mathrm{AB}}_{\mathrm{int}}|0l\rangle \langle 0l|\hat{H}^{\mathrm{AB}}_{\mathrm{int}}|00\rangle}{E^{\mathrm{B}}_l - E^{\mathrm{B}}_0}, \tag{1.70}$$

$$\epsilon^{(2)}_{\mathrm{disp}}(R) = -\sum_{k\neq 0, l\neq 0} \frac{\langle 00|\hat{H}^{\mathrm{AB}}_{\mathrm{int}}|kl\rangle \langle kl|\hat{H}^{\mathrm{AB}}_{\mathrm{int}}|00\rangle}{E^{\mathrm{A}}_k + E^{\mathrm{B}}_l - E^{\mathrm{A}}_0 - E^{\mathrm{B}}_0}, \tag{1.71}$$

where the primed sum indicates that k and l cannot be equal to zero simultaneously; $\epsilon^{(2)}_{\mathrm{ind-A}}(R)$ is the induction energy of atom/ion A obtained from $\epsilon^{(2)}(R)$ when $l = 0$; $\epsilon^{(2)}_{\mathrm{ind-B}}(R)$ is the induction energy of atom/ion B obtained from $\epsilon^{(2)}(R)$ when $k = 0$; and lastly, $\epsilon^{(2)}_{\mathrm{disp}}(R)$ is the dispersion energy obtained from $\epsilon^{(2)}(R)$ when neither k, nor l equals to zero.

The induction energy can be significant for diatomic molecular ions as it is in our cases, where an ion always interacts with a neutral atom, inducing thus a dipole and quadrupole. The interaction of monopole-induced dipole (m−id) and monopole-induced quadrupole (m−iq) can be expressed as

$$\begin{aligned}\epsilon^{(2)}_{\mathrm{ind}}(\mathrm{m-id}, \mathrm{m-iq})(R) &= -\frac{1}{2R^4}\left(q^2_{\mathrm{A}}\bar{\alpha}^{\mathrm{B}}_1 + q^2_{\mathrm{B}}\bar{\alpha}^{\mathrm{A}}_1\right) + \\ &+ \frac{1}{4\pi\epsilon_0}\frac{1}{R^6}\left(q^2_{\mathrm{A}} \sum_{l\neq 0} \frac{\langle 0 \left|\hat{Q}^{\mathrm{B}}_{zz}\right| l\rangle \langle l|\hat{Q}^{\mathrm{B}}_{zz}|0\rangle}{E_l - E_0} + q^2_{\mathrm{B}} \sum_{k\neq 0} \frac{\langle 0 \left|\hat{Q}^{\mathrm{A}}_{zz}\right| k\rangle \langle k|\hat{Q}^{\mathrm{A}}_{zz}|0\rangle}{E_k - E_0}\right), \end{aligned} \tag{1.72}$$

which for $q_{\mathrm{A}} = 0$, $q_{\mathrm{B}} = e$ and zero atomic dipole moments has a form

$$\epsilon^{(2)}_{\mathrm{ind}}(\mathrm{m-id}, \mathrm{m-iq})(R) = -\frac{e^2 \bar{\alpha}^{\mathrm{A}}_1}{2R^4} + \frac{1}{4\pi\epsilon_0}\frac{e^2}{R^6}\sum_{k\neq 0}\frac{\langle 0 \left|\hat{Q}^{\mathrm{A}}_{zz}\right| k\rangle \langle k|\hat{Q}^{\mathrm{A}}_{zz}|0\rangle}{E_k - E_0}, \tag{1.73}$$

where generally

$$\bar{\alpha}_1 = \frac{1}{4\pi\epsilon_0}\frac{2}{3}\sum_{l\neq 0}\frac{\langle 0|\hat{\mathbf{d}}|l\rangle \langle l|\hat{\mathbf{d}}|0\rangle}{E_l - E_0} \tag{1.74}$$

is the average static atomic dipole polarisability.

In the Taylor series of $\hat{H}^{\mathrm{AB}}_{\mathrm{int}}$ in powers of r_i/R, the first non-vanishing term in the dispersion energy corresponds to $1/R^6$. The dispersion energy in the multipole expansion is very often expressed as

$$\epsilon^{(2)}_{\mathrm{disp}}(R) = -\sum_{m=6}^{\infty}\frac{C_m}{R^m}, \tag{1.75}$$

where C_m are dispersion coefficients. In our diatomic case, the expansion in Equation (1.75) contains only even powers. Odd powers can occur in interactions between molecules. For example, the term $m = 7$ exists for molecules with no inversion center. The term $m = 6$ is due to dipole-dipole interaction; $m = 8$ is due to dipole-quadrupole; $m = 10$ due to dipole-octapole and quadrupole-quadrupole interactions [42].

The leading term of the induction energy for S-atom-cation interaction is proportional to $1/R^4$. For P-atom-cation interaction, it is monopole-quadrupole interaction proportional to $1/R^3$, which is coming from the first perturbation. These terms are significant for us and we will use them in the extrapolation of interaction energies $U(R_i), i = 1, 2, \ldots, M$ obtained from *ab initio* absolute energies $V(R_i), i = 1, 2, \ldots, M$.

To calculate *ab initio* $V(R_i)$ and $d_\alpha(R_i)$ data, the post-Hartree-Fock methods must be used in order to deal with multireference problems and to describe the electron correlation. Correctly, large basis sets are also necessary when highly precise methods are used. Because solving the electronic problem in Equation (1.44) is not the aim of this work, more information about *ab initio* calculations can be found in [44, 45].

Note on Transition Dipole Moment

The transition dipole moment for a molecular system (not atomic) is denoted $d_\alpha(R_i)$. We have already mentioned the dipole-moment operator for a system AB, $\hat{\mathbf{d}}$, in Equation (1.19). After the integration over electronic part between two electronic states, one obtains the transition dipole moment vector function for this transition

$$\mathbf{d}_{fi}(\mathbf{R}) = \int \psi^*_f(\mathbf{r})\hat{\mathbf{d}}\psi_i(\mathbf{r})\mathrm{d}\mathbf{r}. \tag{1.76}$$

By a further integration over nuclear angular part, the selection rules are obtained. The remaining radial part will be shown later. At this point, we reveal that in

ab initio calculations only one component of $\mathbf{d}_{fi}(R)$ is calculated, $d_\alpha(R)$, where $\alpha = x, y$ or z and the indices fi are omitted for simplicity. Transitions will be always specified.

1.5 Ro-vibrational Wave Functions

In this Section, we deal only with radial nuclear wave functions that are part of ro-vibrational wave functions. The angular part of nuclear wave function does not directly enter our computations. Its importance is, however, obvious if one realises that it plays a crucial role in selection rules for transitions.

Numerically, radial Schrödinger equation (1.46) we solve by the **Numerov method** [46] for continuum states and by the **Numerov-Cooley method** [47] or **Discrete Variable Representation method** [48] for bound states. More details about these two methods will be given in Section 1.7.2.

The boundary conditions to solve radial Schrödinger equation (1.46) for bound states are

$$\psi_{v,J,\Omega}(0) = \psi_{v,J,\Omega}(R \to \infty) = 0, \tag{1.77}$$

and $\psi_{v,J,\Omega}(R)$ is normalised to unity

$$\int_0^\infty |\psi_{v,J,\Omega}(R)|^2 \, \mathrm{d}R = 1. \tag{1.78}$$

The boundary conditions for the continuum-state wave function $\chi_{E,J,\Omega}(R)$ are

$$\chi_{E,J,\Omega}(0) = 0, \tag{1.79}$$

$$\chi_{E,J,\Omega}(R \text{ large}) \approx \sqrt{\frac{2\mu}{\hbar^2 \pi k}} \sin\left[kR - \frac{1}{2}J\pi + \delta_{J,\Omega}(E)\right], \tag{1.80}$$

where $\delta_{J,\Omega}(E)$ is the phase shift at the continuum energy E and $k = |\mathbf{k}|$ is the length of the wave vector $\mathbf{k}$. Formula (1.80) follows from the energy normalisation of $\chi_{E,J,\Omega}(R)$.

Four ro-vibrational bound-state wave functions of $\mathrm{HeLi}^+(\mathrm{a}^3\Sigma^+)$ are plotted in Figure 1.3. The Figure compares wave functions of the two lowest vibrational levels, $v = 0, 1$, with the rotational quantum numbers $J = 0, 101$. The vibrational quantum numbers are equal to number of nodes of the wave function; therefore, there are no nodes for $v = 0$ and one node for $v = 1$. The wave functions with higher rotational quantum numbers have slightly smaller amplitudes and a center "moved" away from the global minimum. The reason is that J and Ω in Equation (1.46) "alter" $U(R)$ into an effective potential $U_{J,\Omega}(R)$

$$U_{J,\Omega}(R) = U(R) + \frac{\hbar}{2\mu}\frac{J(J+1) - \Omega^2}{R^2}. \tag{1.81}$$

An effective potential is plotted in Figure 1.4 for $\mathrm{a}^3\Sigma^+$ and $J = 101, 159$. The larger the rotational quantum number is, the energetically higher the global minimum becomes. Essentially, J "pushes" the whole function up.

Continuum-state wave functions of the same symmetry and same values of the projections of the total electronic orbital and spin angular momenta ($\Omega = 0$,

Figure 1.3: The bound-state wave functions for four ro-vibrational states: $v = 0, J = 0$, $v = 0, J = 101$, $v = 1, J = 0$, and $v = 1, J = 101$ of $HeLi^+(a^3\Sigma^+)$.

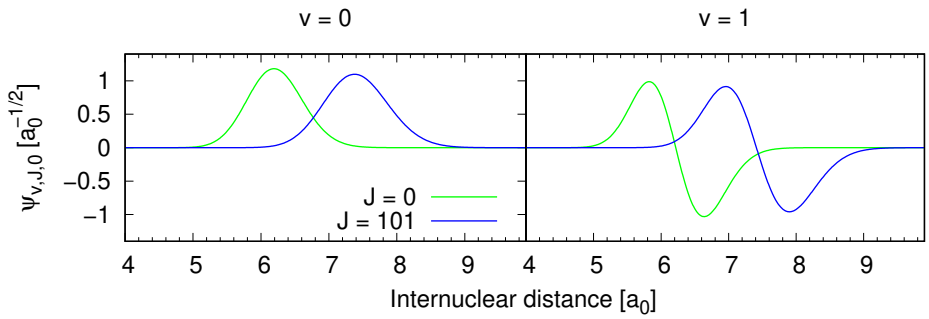

Figure 1.4: Effective potential $U_{J,0}(R)$ is illustrated for $HeLi^+(a^3\Sigma^+)$ with $J = 101, 159$.

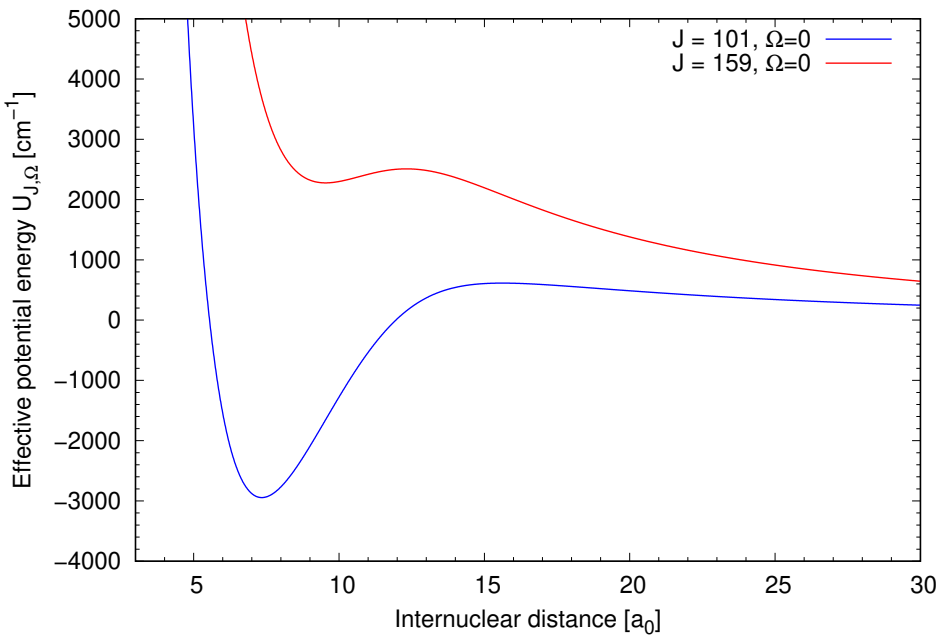

Figure 1.5: The continuum-state wave functions at $E = 2\,329.9$ cm^{-1} with $J = 0, 101$ are illustrated together with a wave function of the quasibound state (shape resonace) at the same energy andbut $v = 0, J = 159$ of HeLi$^+$(a$^3\Sigma^+$).

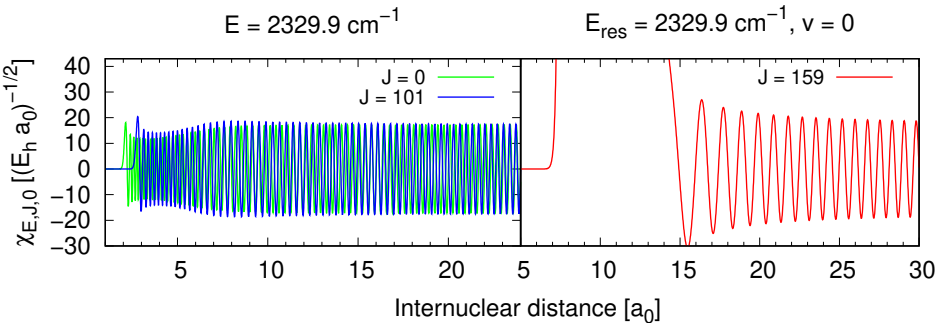

$\Sigma = 0$) are illustrated in Figure 1.5. In the left panel, the wave functions at the collision energy $E = 2\,329.9$ cm^{-1} and the rotational quantum numbers $J = 0, 101$ are compared.

Special cases of continuum states are the so-called **quasibound states**. They are not true bound states but the system can live in them quite long and the shape of their wave functions in front of the mid-turning point resembles a bound-state wave functions. A resonance wave function in the right panel of Figure 1.5 corresponds to $E = 2\,329.9$ cm^{-1},$J = 159, \Omega = 0$ and in LEVEL 7.0 [49] it is associated to $v = 0$. It reaches its maximum at 9.63 a_0 equal to $299\,257.959\,708$ $(E_\mathrm{h} a_0)^{-1/2}$. This maximum may entail a relatively long-living state, which is similar to a bound state, albeit its wave function behind this maximum oscillates around zero with a much smaller amplitudes (in other cases the amplitudes do not have to be so different). This oscillation is a continuum-state feature as it can be seen in Figure 1.5 left panel.

In this work, the existence of quasibound states stems from a barrier, mostly from a centrifugal barrier (the second term in Schrödinger equation (1.46) or Equation (1.81)). Hence these quasibound states are also called **shape resonances**. If the PEC of an electronic state exhibits a barrier itself above its dissociation limit (in $U(R) > 0$ term), then these quasibound states can also be rotationless. A barrier traps the system in the continuum state, causing thus longer (tunnelling) lifetimes. This quantal phenomenon affects the cross-section and rate-coefficient values.

If a PEC has two minima, the bound-state wave functions can either be localised in one of the wells or be delocalised. In Figure 1.6, a potential is illustrated with five bound-state wave functions plotted. The inner well is much deeper in comparison with the outer well. The ro-vibrational ground state ($v = 0, J = 0$) is localised in the inner well. The last pure vibrational level $v = 4$ (i.e. $J = 0$), which is localised on this inner well, is also plotted, and it has four nodes as it should. The first ro-vibrational level $v = 5, J = 0$, localised in the outer well, is also illustrated. Notice that there is no node as if the vibrational quantum number was equal to zero and in some way it really is. We could write instead $v' = 0, J = 0$, where the prime indicates the numbering of the shallow outer well. The bound-state wave functions for $v = 18, 19$ and $J = 0$, which are delocalised, are depicted, too. The dashed lines in Figure 1.6 are selected rotationless vibrational levels,

Figure 1.6: The double-well potential energy curve for CO^+ $1^2\Sigma^-$ ($\Omega = 0$ is omitted in the key) with the plotted bound-state wave functions $\psi_{v,J}(R)$ for ro-vibrational levels $v = 0, 4, 5, 18, 19$; $J = 0$ and their plotted energy levels together with $v = 1, 2, 3$; $J = 0$.

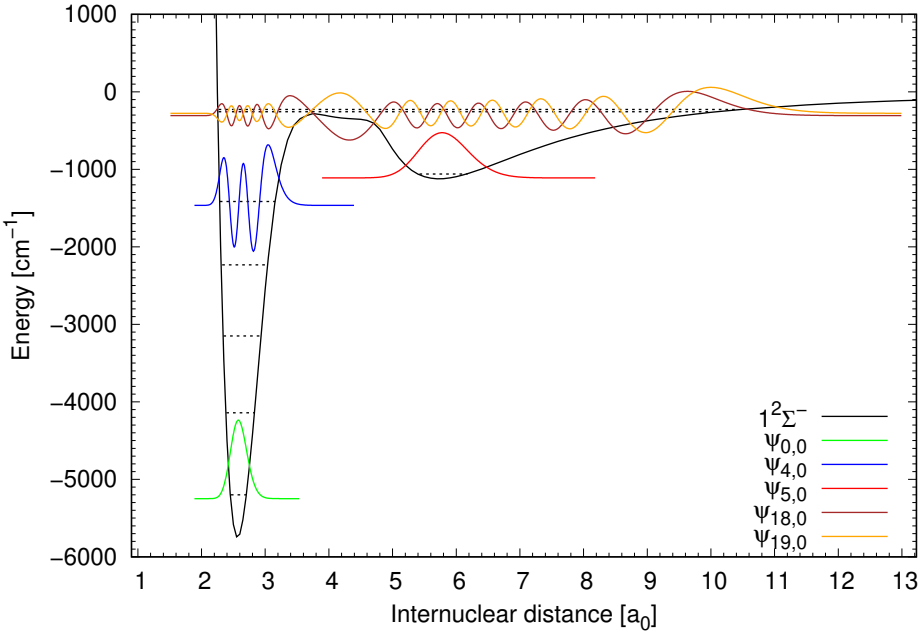

$v = 0, 1, 2, 3, 4, 5, 15, 16$.

1.6 Radiative Processes

In Section 1.3, it was mentioned that a radiative deexcitation can happen from a continuum or bound state to a continuum or bound state. According to the initial and final state, a radiative process can be classified as it follows. When the deexcitation

- starts and also finishes in a bound state, it is called a bound-bound process and is illustrated in Figure 1.7 by a red line;

- starts in a bound state and finishes in a continuum state, it is called a bound-free (also bound-continuum) process and is illustrated in Figure 1.7 by a blue line;

- starts in a continuum state and finishes in a bound state, it is called a free-bound (also continuum-bound) process and we will refer to it also as **radiative association** (RA). It is illustrated in Figure 1.7 by a green line;

- starts and also finishes in a continuum state, it is called a free-free (also contintuum-continuum) process. In this work, we deal with only such a free-free process, when an ion exchanges its charge with a neutral atom in a collision; this is called **radiative charge transfer** (RCT) and is illustrated in Figure 1.7 by a brown line.

Figure 1.7: Radiative processes between two electronic states, $b^3\Sigma^+$ and $a^3\Sigma^+$ of $HeLi^+$, with a different dissociation limit are illustrated for the bound-bound (red), bound-free (blue), free-bound (green) and free-free (brown) case.

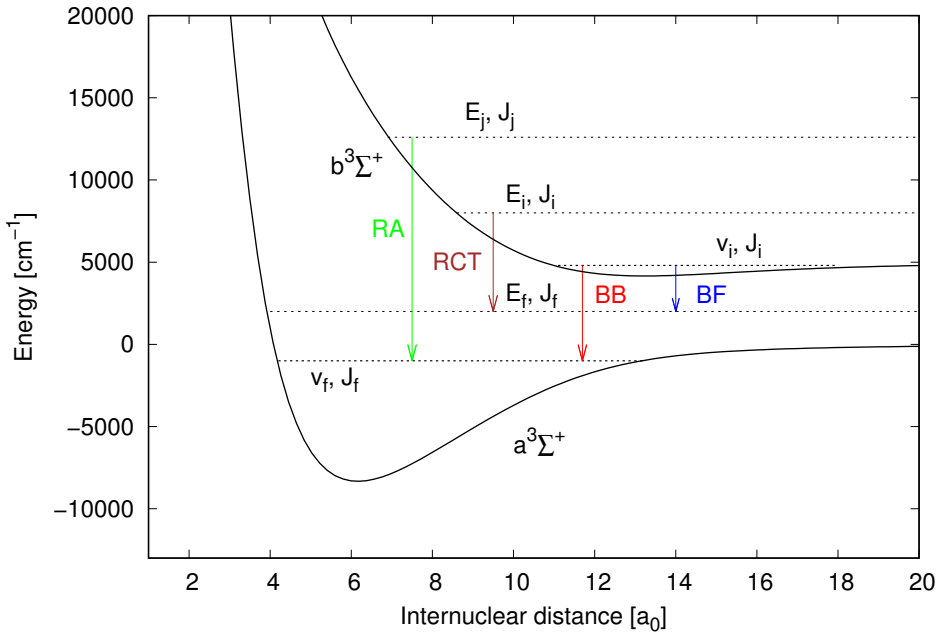

The bound-bound and bound-free processes together allow us to estimate the **radiative lifetimes** (RLTs) of a bound state.

The goal in the RA and RCT calculations is to obtain the rate coefficients for stimulated and spontaneous emission

$$\alpha(T, T_\mathrm{b}) = \left(\frac{8}{\mu\pi}\right)^{1/2} \left(\frac{1}{k_\mathrm{B}T}\right)^{3/2} \int_0^\infty E_i \sigma(E_i; T_\mathrm{b}) e^{-E_i/k_\mathrm{B}T} \mathrm{d}E_i, \tag{1.82}$$

where μ is the reduced mass of a diatomic system, k_B is the Boltzmann constant, T is the temperature, and $\sigma(E_i; T_\mathrm{b})$ is the cross section of the studied process (e.g. RA or RCT) at the collision energy E_i and the background temperature T_b of the black-body radiation. The cross section for spontaneous emission is $\sigma(E_i; T_\mathrm{b}{=}0) = \sigma(E_i)$, and $\sigma(E_i; T_\mathrm{b}{>}0)$ is the total cross section that is a sum of spontaneous and stimulated emission cross sections.

Sometimes, one can be interested in the rate coefficient for a depopulation of a continua of an initial electronic state. Then,

$$\alpha_\mathrm{dep}(T, T_\mathrm{b}) = \sum_k \alpha_k(T, T_\mathrm{b}), \tag{1.83}$$

where $\alpha_k(T, T_\mathrm{b})$ is a rate coefficient from Equation (1.82) for the k-th transition from one electronic state to the same or another electronic state.

Rate coefficients are input parameters in **reaction networks** widely used in astrochemical models and in astrophysical analyses of spectroscopic data (see for example in [50]). The results of reaction networks are influenced also by RLTs.

In this chapter, we will try to look at the above mentioned emission processes. Notice that for spontaneous emission $T_\mathrm{b} = 0$ K and we can simplify rate coeffi-

cient (1.82) to be a function of only temperature $\alpha(T)$, for which we need only $\sigma(E_i)$. The relation between $\sigma(E_i; T_\mathrm{b})$ and $\sigma(E_i)$ can be shown through the corresponding partial cross sections $\sigma_\mathrm{par}(E_i, T_\mathrm{b})$ and $\sigma_\mathrm{par}(E_i)$ through which either a sum or an integral over the final states (depending on the character of the studied process) give $\sigma(E_i; T_\mathrm{b})$ and $\sigma(E_i)$. The relation between the partial cross sections is

$$\sigma_\mathrm{par}(E_i; T_\mathrm{b}) = \sigma_\mathrm{par}(E_i) \frac{1}{1 - e^{-\frac{E_i + \Delta E - E_f}{k_\mathrm{B} T_\mathrm{b}}}}, \tag{1.84}$$

where ΔE was introduced in Section 1.4 in Equation (1.47). The last equation can be deduced from Equation (1.37), which comprises a sum of the probabilities of stimulated (left-hand part) and spontaneous (right-hand part) emission. The energy density per volume unit for the black-body radiation from Equation (1.37) is

$$\rho(\omega_{if}) = \frac{2\hbar}{\pi} \left(\frac{\omega_{if}}{c}\right)^3 \frac{1}{e^{\frac{\hbar\omega_{if}}{k_\mathrm{B} T_\mathrm{b}}} - 1}, \tag{1.85}$$

where $\hbar\omega_{if} = E_i + \Delta E - E_f$. Equation (1.84) and its derivation is detailed, for example, in [51].

1.6.1 Radiative Lifetimes

We shall start with processes beginning in a bound state: bound-bound and bound-free processes. A quantum mechanical characterisation for such an initial bound state is its RLT, which determines how long the molecule stays in the bound state. As it was mentioned in Section 1.5, a bound state has its vibrational and rotational quantum numbers and the projection of the total electronic angular momentum. In order to differentiate between the initial and final ro-vibrational bound state quantum numbers, we will add a lower index i to the initial state numbers and f to the final state numbers.

RLT of a ro-vibrational bound state characterised by v_i, J_i, Ω_i can be calculated from a formula

$$\tau_{v_i, J_i, \Omega_i} = \frac{\hbar}{\Gamma^\mathrm{rad}_{v_i, J_i, \Omega_i}}. \tag{1.86}$$

Most of the following theory was adopted from [27, 52]. Here we only specify the dependence on Ω_i. $\Gamma^\mathrm{rad}_{v_i, J_i, \Omega_i}$ denotes the radiative width of the initial ro-vibrational bound state, which is a sum of the radiative width corresponding to the bound-bound processes $\Gamma^\mathrm{BB}_{v_i, J_i, \Omega_i}$ and the radiative width corresponding to the bound-free processes $\Gamma^\mathrm{BF}_{v_i, J_i, \Omega_i}$

$$\Gamma^\mathrm{rad}_{v_i, J_i, \Omega_i} = \Gamma^\mathrm{BB}_{v_i, J_i, \Omega_i} + \Gamma^\mathrm{BF}_{v_i, J_i, \Omega_i}. \tag{1.87}$$

The relation of $\Gamma^\mathrm{BB}_{v_i, J_i, \Omega_i}$ to Equation (1.38) is

$$\Gamma^{\mathrm{BB}}_{v_i,J_i,\Omega_i} = \sum_f \hbar A^{\mathrm{BB}}_{v_i,J_i,\Omega_i;v_f,J_f,\Omega_f}, \tag{1.88}$$

$$= \sum_f \frac{1}{4\pi\epsilon_0}\frac{4}{3}p_i\left(\frac{\omega_{if}}{c}\right)^3 S_{J_i,\Omega_i;J_f,\Omega_f}\left|M_{v_i,J_i,\Omega_i;v_f,J_f,\Omega_f}\right|^2, \tag{1.89}$$

where $A^{\mathrm{BB}}_{v_i,J_i,\Omega_i;v_f,J_f,\Omega_f}$ is the Einstein A coefficient for spontaneous bound-bound emission, p_i is the probability of approach in the initial eletronic state, ω_{if} is the frequency of the emitted photon with an energy $\hbar\omega_{if} = E_{v_i,J_i,\Omega_i} + \Delta E - E_{v_f,J_f,\Omega_f}$, where E_{v_i,J_i,Ω_i} and E_{v_f,J_f,Ω_f} are the energies of the initial and final ro-vibrational bound states, respectively.

In Equation (1.89), the Hönl-London factors $S_{J_i,\Omega_i;J_f,\Omega_f}$ come from the angular part of the transition dipole-moment matrix and give us the selection rules for a transition. From the radial part, we get the transition dipole-moment matrix elements

$$M_{v_i,J_i,\Omega_i;v_f,J_f,\Omega_f} = \left\langle \psi_{v_f,J_f,\Omega_f}\left|T^1_q\left[\mathbf{d}(R)\right]\right|\psi_{v_i,J_i,\Omega_i}\right\rangle, \tag{1.90}$$

$$= \int_0^\infty \psi^*_{v_f,J_f,\Omega_f}(R)T^1_q\left[\mathbf{d}(R)\right]\psi_{v_i,J_i,\Omega_i}(R)\mathrm{d}R, \tag{1.91}$$

where $\psi_{v_f,J_f,\Omega_f}(R)$ and $\psi_{v_i,J_i,\Omega_i}(R)$ are the final and initial radial ro-vibrational bound-state wave functions, $T^1_q\left[\mathbf{d}(R)\right]$ is the irreducible spherical operator for the transition dipole moment $\mathbf{d}(R)$ of rank $k = 1$ and $q = \Lambda_f - \Lambda_i$ is the change of the projection of the electronic orbital angular momentu or also $q = -k, -k+1, \ldots, 0, \ldots, k-1, k$; hence for $k = 1$, $q = 0, \pm 1$. For its values

$$q = 0, \qquad T^1_0\left[\mathbf{d}(R)\right] = d_z(R), \tag{1.92}$$

$$q = 1, \qquad T^1_1\left[\mathbf{d}(R)\right] = -\frac{1}{\sqrt{2}}\left[d_x(R) + id_y(R)\right], \tag{1.93}$$

$$q = -1, \qquad T^1_{-1}\left[\mathbf{d}(R)\right] = \frac{1}{\sqrt{2}}\left[d_x(R) - id_y(R)\right], \tag{1.94}$$

where z axis is parallel with the bond in the diatomic system. Notice that the wave functions in Equation (1.91) are calculated as real; thus, $\psi^*_{v_f,J_f,\Omega_f}(R) = \psi_{v_f,J_f,\Omega_f}(R)$.

The relation of $\Gamma^{\mathrm{BF}}_{v_i,J_i,\Omega_i}$ to Einstein coefficient (1.38) is

$$\Gamma^{\mathrm{BF}}_{v_i,J_i,\Omega_i} = \int_0^{E_{v_i,J_i,\Omega_i}+\Delta E} \hbar A^{\mathrm{BF}}_{v_i,J_i,\Omega_i;E_f,J_f,\Omega_f}\mathrm{d}E_f, \tag{1.95}$$

$$= \int_0^{E_{v_i,J_i,\Omega_i}+\Delta E} \frac{1}{4\pi\epsilon_0}\frac{4}{3}p_i\left(\frac{\omega_{if}}{c}\right)^3 S_{J_i,\Omega_i;J_f,\Omega_f}\left|M_{v_i,J_i,\Omega_i;E_f,J_f,\Omega_f}\right|^2\mathrm{d}E_f, \tag{1.96}$$

where $A^{\mathrm{BF}}_{v_i,J_i,\Omega_i;E_f,J_f,\Omega_f}$ is the Einstein coefficient for spontaneous bound-free emission, the energy of the emitted photon is now equal to $\hbar\omega_{if} = E_{v_i,J_i,\Omega_i} + \Delta E - E_f$ where E_f is the energy of the final continuum state; $M_{v_i,J_i,\Omega_i;E_f,J_f,\Omega_f}$ is again the matrix element for the transition dipole moment and its formula is

$$M_{v_i,J_i,\Omega_i;E_f,J_f,\Omega_f} = \left\langle \chi_{E_f,J_f,\Omega_f} \left| T_q^1 \left[\mathbf{d}(R)\right] \right| \psi_{v_i,J_i,\Omega_i} \right\rangle, \tag{1.97}$$

$$= \int_0^\infty \chi^*_{E_f,J_f,\Omega_f}(R) T_q^1 \left[\mathbf{d}(R)\right] \psi_{v_i,J_i,\Omega_i}(R) \mathrm{d}R, \tag{1.98}$$

where χ_{E_f,J_f,Ω_f} denotes the wave function for the final continuum state.

1.6.2 Radiative Association

In the previous Section, we discussed the transitions from bound states. Now, we will look at the transitions from continuum to bound states, which result in the formation of a molecule from two free atoms.

Cross sections $\sigma(E_i)$ are a sum over all allowed free-bound transitions

$$\sigma(E_i) = \sum_{J_i,\Omega_i;v_f,J_f,\Omega_f} \sigma_{J_i,\Omega_i;v_f,J_f,\Omega_f}(E_i), \tag{1.99}$$

where $\Omega = \Lambda + \Sigma$ is a sum of the projections of the orbital and spin angular momentum, Λ and Σ, respectively; $\sigma_{J_i,\Omega_i;v_f,J_f,\Omega_f}(E_i)$ denotes the partial cross sections for the free-bound transitions, and it can be expressed as

$$\sigma_{J_i,\Omega_i;v_f,J_f,\Omega_f}(E_i) = \frac{1}{4\pi\epsilon_0}\frac{8}{3}\left(\frac{\pi}{k}\right)^2 p_i \left(\frac{\omega_{if}}{c}\right)^3 S_{J_i,\Omega_i;J_f,\Omega_f} \left| M_{E_i,J_i,\Omega_i;v_f,J_f,\Omega_f} \right|^2, \tag{1.100}$$

where $k = \sqrt{2\mu E_i}/\hbar$ is the wave vector, c is the speed of light, $S_{J_i,\Omega_i,J_f,\Omega_f}$ are the Hönl-London factors, $M_{E_i,J_i,\Omega_i;v_f,J_f,\Omega_f}$ is the matrix element of transition dipole moment $\mathbf{d}(R)$

$$M_{E_i,J_i,\Omega_i;v_f,J_f,\Omega_f} = \left\langle \psi_{v_f,J_f,\Omega_f} \left| T_q^1 \left[\mathbf{d}(R)\right] \right| \chi_{E_i,J_i,\Omega_i} \right\rangle, \tag{1.101}$$

$$= \int_0^\infty \psi^*_{v_f,J_f,\Omega_f}(R) T_q^1 \left[\mathbf{d}(R)\right] \chi_{E_i,J_i,\Omega_i}(R) \mathrm{d}R, \tag{1.102}$$

similarly as in Equations (1.91) and (1.98). Finally, ω_{if} is the frequency of the emitted photon with the energy $\hbar\omega_{if} = E_i + \Delta E - E_{v_f,J_f,\Omega_f}$.

The above formulae are derived from quantum mechanics, specifically from the Fermi's Golden rule [53]. In numerical calculations, however, it becomes hard to evaluate Equation (1.100) around energies where the initial state has its shape resonances. Especially for **narrow resonances** when the ratio $\Gamma^{\mathrm{tun}}_{v,J,\Omega}/E_{v,J,\Omega}$ of the tunnelling width $\Gamma^{\mathrm{tun}}_{v,J,\Omega}$ and the resonance energy $E_{v,J,\Omega}$ is very small (we usually set the threshold 10^{-10} or 10^{-13}). From a tunnelling width, a lifetime of tunnelling to a continuum state with the same energy can be expressed as

$$\tau^{\mathrm{tun}} = \frac{\hbar}{\Gamma^{\mathrm{tun}}_{v,J,\Omega}}. \tag{1.103}$$

Typically, when $\Gamma^{\mathrm{tun}}_{v,J,\Omega}$ is large, $\Gamma^{\mathrm{rad}}_{v,J,\Omega}$ is small and vice versa.

For the cases of narrow resonances, it is useful to use an approximate formula [54, 55] from the **Breit-Wigner** (BW) **theory** [56] or also called **Cauchy distribution** for the RA rate coefficient

$$\alpha_{\mathrm{n}}(T) = \hbar^2 \left(\frac{2\pi}{\mu k_{\mathrm{B}} T}\right)^{3/2} p_i \sum_{\Omega_i, r_i} (2J_i + 1)\, e^{-E_{v_i,J_i,\Omega_i}/k_{\mathrm{B}}T} \frac{\Gamma^{\mathrm{rad}}_{v_i,J_i,\Omega_i} \Gamma^{\mathrm{tun}}_{v_i,J_i,\Omega_i}}{\Gamma_{v_i,J_i,\Omega_i}}, \tag{1.104}$$

where the sum is over all shape resonances of the initial electronic state (indicated by r_i) and over all its projections Ω_i. The corresponding resonance energies are denoted E_{v_i,J_i,Ω_i}. Index n in $\alpha_{\mathrm{n}}(T)$ means this formula is used only for narrow resonances. If someone uses BW formula (1.104), then a neighbourhood δ_{r_i} (specified later for each process separately) around energies of narrow resonances E_{v_i,J_i,Ω_i} must be omitted in the integration in Equation (1.82).

Stimulated Emission

In Equation (1.84), we introduced a general expression for a partial cross section for stimulated and spontaneous emission. We can use the RA partial cross section from Equation (1.100) and write the RA partial cross section $\sigma(E_i, T_{\mathrm{b}})$

$$\sigma_{J_i,\Omega_i;v_f,J_f,\Omega_f}(E_i, T_{\mathrm{b}}) = \sigma_{J_i,\Omega_i;v_f,J_f,\Omega_f}(E_i) \frac{1}{1 - e^{-\frac{E_i + \Delta E - E_{v_f,J_f,\Omega_f}}{k_{\mathrm{B}} T_{\mathrm{b}}}}}. \tag{1.105}$$

The factor in the denominator enlarges the cross sections in the black-body radiation. The effect is noticeable for $\Delta E = 0$, while for large ΔE,

$$e^{-\frac{E_i + \Delta E - E_{v_f,J_f,\Omega_f}}{k_{\mathrm{B}} T_{\mathrm{b}}}} \approx 0 \tag{1.106}$$

and, thus, $\sigma_{J_i,\Omega_i;v_f,J_f,\Omega_f}(E_i, T_{\mathrm{b}} \neq 0) \approx \sigma_{J_i,\Omega_i;v_f,J_f,\Omega_f}(E_i)$.

The expression for the rate coefficients for stimulated and spontaneous emission was introduced in Equation (1.82). If $\Delta E \neq 0$, then the enhancement by the stimulated emission can only be seen for very large temperatures and still this enhancement is not as large as when $\Delta E = 0$.

Spinless Approximation

A so-called spinless approximation (SLA) is often used in Equation (1.100) by setting $\Sigma = 0$ and, therefore, $\Omega = \Lambda$ and $\Delta\Omega = \Delta\Lambda$. Further, if we realise that only squared Ω is in Equation (1.46), then, we can be interested in only $|\Omega| = |\Lambda|$. These two steps reduce the sum in cross section (1.100).

For the spinless cross section, it was introduced

$$\sigma_{\mathrm{SLA}}(E_i) = N_{\Omega_i \to \Omega_f} \sigma^{\Lambda_i \to \Lambda_f} \tag{1.107}$$

in a similar way in [31]. Here, it is expressed more generally, where $N_{\Omega_i \to \Omega_f}$ denotes the number of Ω-distinguished transitions, and $\sigma^{\Lambda_i \to \Lambda_f}$ denotes the cross sections for a Λ-transition with $\Sigma_i = \Sigma_f = 0$.

The spinless rate coefficient is then

$$\alpha_{\mathrm{SLA}}(T) = N_{\Omega_i \to \Omega_f} \alpha^{\Lambda_i \to \Lambda_f}(T), \tag{1.108}$$

or it can be directly calculated from $\sigma_{\mathrm{SLA}}(E_i)$ using Equation (1.82).

Semiclassical Method

Another way how to obtain RA cross sections is to use a semiclassical method (SC) that treats mere background contribution and to include the whole resonance contribution by employing the BW theory for all resonances. This method is derived from the Optical Potential Method (not used in this work) for transitions between two different electronic states. The theory of the SC method can be found in [48] or [57].

Needless to say, the SC method neglects the spin, similarly to SLA. Thus, $\Sigma = 0$ for both initial and final states, and $\Delta\Sigma = 0$, $\Omega = \Lambda$. Then we can say electronic states are determined by Λ, the projection of the orbital angular momentum. In the quantal approach without SLA, we have $\Omega_i \to \Omega_f$ transitions and we sum over them in order to obtain the cross section of a transition between two electronic states. Here, we have $\Lambda_i \to \Lambda_f$ transitions and we do not have to sum over them in order to obtain the cross section of an electronic transition. The SC cross section for such a process is

$$\sigma_{\Lambda_i \to \Lambda_f}(E_i) = 4\pi \sqrt{\frac{\mu}{2E_i}} p_i \int_0^\infty b \int_{R_c}^\infty \frac{A_{\Lambda_i,\Lambda_f}(R)}{\sqrt{1 - \frac{U_i(R)}{E_i} - \frac{b^2}{R^2}}} \mathrm{d}R\mathrm{d}b \tag{1.109}$$

where b is the impact parameter defined as the distance between the path a colliding particle would undergo with no interaction present and the center of the other particle present in the collision [58]; $U_i(R)$ is PEC for the initial electronic state at the internuclear distance R; R_c denotes the outer turning point (if the PEC of the initial state has a long-range barrier and it corresponds to the turning point at the largest internuclear distance), and $A_{\Lambda_i,\Lambda_f}(R)$ is the R-dependent analogue of the Einstein coefficient for the spontaneous emission

$$A_{\Lambda_i,\Lambda_f}(R) = \frac{1}{4\pi\epsilon_0} \frac{4}{3\hbar} \left[\frac{\omega_{if}(R)}{c}\right]^3 \frac{2 - \delta_{0,\Lambda_i+\Lambda_f}}{2 - \delta_{0,\Lambda_i}} \left|T_q^1\left[\mathbf{d}(R)\right]\right|^2, \tag{1.110}$$

$$\text{if} \quad E_i < \hbar\omega_{if}(R) \quad \text{and} \quad U_f(R) + \frac{E_i b^2}{R^2} < U_f(R \to \infty), \tag{1.111}$$

$$A_{\Lambda_i,\Lambda_f}(R) = 0, \quad \text{otherwise.} \tag{1.112}$$

The frequency of the emitted photon, $\omega_{if}(R)$, has the energy

$$\hbar\omega_{if}(R) = U_i(R) - U_f(R), \tag{1.113}$$

where $U_f(R)$ denotes PEC for the final electronic state at R. The rest of the physical quantities in Equations (1.109) - (1.111) are denoted similarly as in the quantal approach.

Condition (1.111) secures that the calculated cross sections are for a RA process. In other words, it secures the final state is a bound state, not a continuum

state. Also notice that the definition of the energy of the emitted photon assumes $\Delta E = 0$. The photon-energy definition assumes the Franck-Condon principle: The internuclear distance does not change during the electronic transition. Equation (1.113) limits the SC method to only transitions between two different electronic states because the photon energy would be equal to zero for processes within one dissociation limit. A reformulation of Equation (1.111) could allow the SC approach to be applicable for transition between electronic states with $\Delta E \neq 0$.

The **Breit-Wigner** RA cross sections can be expressed as

$$\sigma_{\Lambda_i \to \Lambda_f}(E_i) = \frac{\pi}{k^2} p_i \sum_{r_i} (2J_i + 1) \frac{4\Gamma^{\text{tun}}_{v_i,J_i,\Lambda_i} \Gamma^{\text{rad}}_{v_i,J_i,\Lambda_i}}{4(E_i - E_{v_i,J_i,\Lambda_i})^2 + \Gamma^2_{v_i,J_i,\Lambda_i}}, \tag{1.114}$$

where the dependence of $\Gamma^{\text{tun}}_{v_i,J_i,\Lambda_i}$ and $\Gamma^{\text{rad}}_{v_i,J_i,\Lambda_i}$ on Λ_i is the consequence of $\Omega_i = \Lambda_i$ and that instead of Ω_i in Schrödinger equation (1.46), we use Λ_i in the SC method.

For completeness, the SC **Breit-Wigner** RA rate coefficients can be calculated from Equation (1.104) after putting $\Omega_i = \Lambda_i$.

1.6.3 Radiative Charge Transfer

RCT is a free-free process during which a charge is exchanged between two free atoms; in our case a charge of one electron. The quantal cross section for such a process can be expressed as

$$\sigma(E_i) = \int_0^{\omega_{if}^{\max}} \frac{\mathrm{d}\sigma}{\mathrm{d}\omega_{if}}(E_i, \omega_{if}) \mathrm{d}\omega_{if}, \tag{1.115}$$

$$\frac{\mathrm{d}\sigma}{\mathrm{d}\omega_{if}}(E_i, \omega_{if}) = \frac{1}{4\pi\epsilon_0} \frac{8}{3} \left(\frac{\pi}{k}\right)^2 p_i \left(\frac{\omega_{if}}{c}\right)^3 \sum_{J_i,\Omega_i;J_f,\Omega_f} S_{J_i,\Omega_i;J_f,\Omega_f} \left| M_{E_i,J_i,\Omega_i;E_f,J_f,\Omega_f} \right|^2, \tag{1.116}$$

where $\mathrm{d}\sigma/\mathrm{d}\omega_{if}(E_i, \omega_{if})$ is the differential partial cross section at the collision energy E_i as a function of the frequency of the emitted photon ω_{if} with the energy equal to $\hbar\omega_{if} = E_i + \Delta E - E_f$. The energy of the initial E_i and final E_f continuum states are distiguished by a lower index. The integration over photon-frequency starts at $\omega_{if} = 0$ and ends at $\omega_{if}^{\max} = (E_i + \Delta E)/\hbar$, where $\omega_{if} = 0$ corresponds to $E_f = E_i + \Delta E$ and $\omega_{if}^{\max}$ corresponds to $E_f = 0$. In Equation (1.116), $M_{E_i,J_i,\Omega_i;E_f,J_f,\Omega_f}$ is the matrix element for the transition dipole moment $\mathbf{d}(R)$ expressed as

$$M_{E_i,J_i,\Omega_i;E_f,J_f,\Omega_f} = \left\langle \chi_{E_f,J_f,\Omega_f} \left| T^1_q \left[\mathbf{d}(R)\right] \right| \chi_{E_i,J_i,\Omega_i} \right\rangle, \tag{1.117}$$

$$= \int_0^\infty \chi^*_{E_f,J_f,\Omega_f}(R) T^1_q \left[\mathbf{d}(R)\right] \chi_{E_i,J_i,\Omega_i}(R) \mathrm{d}R. \tag{1.118}$$

The RCT cross sections at large collision energies behave as [59]

$$\sigma(E_i) \approx C/\sqrt{E_i}. \tag{1.119}$$

Equation (1.82) then can be solved for large energies and split into

$$\alpha(T) = \alpha_{\text{fin}}(T, E_i^{\text{m}}) + \alpha_{\text{inf}}(T, E_i^{\text{m}}), \tag{1.120}$$

$$\alpha_{\text{inf}}(T, E_i^{\text{m}}) = C\sqrt{\frac{8}{\mu\pi}}\left[\frac{\sqrt{\pi}}{2}\text{erfc}(x) + xe^{-x^2}\right], \tag{1.121}$$

where $x = \sqrt{E_i^{\text{m}}/(k_{\text{B}}T)}$, E_i^{m} is an initial collision energy at which the asymptotic behaviour of $\sigma(E_i)$ is valid. Up to E_i^{m}, the numerical integration of Equation (1.82) is taken for $\alpha_{\text{fin}}(T, E_i^{\text{m}})$ as

$$\alpha_{\text{fin}}(T, E_i^{\text{m}}) = \left(\frac{8}{\mu\pi}\right)^{1/2}\left(\frac{1}{k_{\text{B}}T}\right)^{3/2}\int_0^{E_i^{\text{m}}} E_i\sigma(E_i)e^{-E_i/k_{\text{B}}T}\text{d}E_i. \tag{1.122}$$

Further, $\text{erfc}(x)$ is the complementary error function [33]. The rate coefficient, thus, exhibits limiting behaviour

$$\alpha(T\to\infty) = C\sqrt{\frac{2}{\mu}} \tag{1.123}$$

from [33].

1.7 Computational Methods

1.7.1 Inter- and Extrapolation

Ab initio data, $U(R_i)$ and $d_\alpha(R_i)$, are sets of points for $i = 1, 2, \ldots, M$ and α denotes one coordinate of $\mathbf{d}(R)$. For $R_1 < R < R_M$ where $R \neq R_i$ and $i = 2, M-1$, the data are interpolated and for $R < R_1$ and $R > R_M$ the data are extrapolated before the mentioned radiative processes calculations can start. For the interpolation, cubic splines are widely used, for example. In this work, however, we use a global interpolation method called the **Reciprocal-Power Reproducing Kernel Hilbert Space** (RP-RKHS) [60, 61, 62], where the interpolated PEC can be expressed as

$$U^{[n,m]}(R) = \sum_{i=1}^{M} a_i^{[n,m]} r^{[n,m]}(R, R_i), \tag{1.124}$$

$$r^{[n,m]}(R, R_i) = \frac{n^2}{R_>^{m+1}} B(m+1, n)\,{}_2F_1(-n+1, m+1; n+m+1; \frac{R_<}{R_>}), \tag{1.125}$$

$$= \frac{1}{R_>^{m+1}} \sum_{k=0}^{n-1} b_k^{[n,m]} \frac{R_<^k}{R_>^k}, \tag{1.126}$$

where $R_< = \min(R, R_i)$, $R_> = \max(R, R_i)$, $a_i^{[n,m]}$ are solutions of

$$U(R_j) = \sum_{i=1}^{M} a_i^{[n,m]} r^{[n,m]}(R_j, R_i) \tag{1.127}$$

and $b_k^{[n,m]}$ for $k = 0, 1, \ldots, n-1$ can be deduced from Equation (1.125), $B(m+1, n)$ and ${}_2F_1(-n+1, m+1; n+m+1; \frac{R_<}{R_>})$ are the Beta function and Gauss' hypergeometric function, respectively. Equation (1.126) indicates the reciprocal power behaviour beyond R_M.

As it was mentioned above, this method is global, i.e. $U(R)$ is determined at an arbitrary position R by the whole set of the *ab initio* data $U(R_i)$ at the positions R_i, $i = 1, 2, \ldots, M$. In order to achieve a better accuracy, it is advisable that R_1 is reasonably small, R_M is large enough and the grid is reasonably dense.

The equations above are only for radial RP-RKHS (also called RP-RKHS for distancelike variables). Other RKHS methods, however, have also been derived for anglelike variables (for more information see [60]).

From [61], the extrapolated potential energy curve at short range ($R < R_1$) is in RP-RKHS

$$U^{[n,m]}(R) = \sum_{k=0}^{n-1} d_k^{[n,m]} R^k, \tag{1.128}$$

$$d_k^{[n,m]} = b_k^{[n,m]} \sum_{i=1}^{M} \frac{a_i^{[n,m]}}{R_i^{m+1+k}} \tag{1.129}$$

and at long range ($R > R_M$) it is

$$U^{[n,m]}(R) = -\sum_{k=0}^{n-1} \frac{c_{m+1+k}^{[n,m]}}{R^{m+1+k}}, \tag{1.130}$$

$$-c_{m+1+k}^{[n,m]} = b_k^{[n,m]} \sum_{i=1}^{M} a_i^{[n,m]} R_i^k. \tag{1.131}$$

where m determines the asymptotically leading terms c_{m+1}/R^{m+1}, and often, $n = 2$.

Usually, it is desired to find the correct long-range behaviour of PEC in the form

$$U(R > R_M) \approx \frac{D_l}{R^l}, \tag{1.132}$$

where $D_l R^{-l}$ is referred to as a leading term of the multipole expansion of the potential energy, and D_l is a constant. Then, it means that in RP-RKHS we need to set $m = l - 1$.

The choice of the leading term depends on which interaction is dominant in the long range. Although all our studied processes have a cation and a neutral atom, the leading term can differ. Important is also the electronic state in which the system is. In other words, in which state an atom approaches a cation. If the neutral atom is in an S state, the cation approximated as a monopole polarises the atom and induces a dipole in the atom. The leading term, thus, corresponds to monopole-induced dipole (m-id) $\approx R^{-4}$. If the neutral atom is in a P state, then monopole-quadrupole (m-q) interaction from $\epsilon_{\text{el}}^{(1)}$ in Equation (1.65) dominates. Then, the leading term corresponds to the monopole-quadrupole interaction R^{-3}.

In the above examples, the former is usually extrapolated as

$$U_{\mathrm{m-id}}(R > R_M) = \frac{D_4}{R^4} + \frac{D_6}{R^6}, \tag{1.133}$$

i.e. $n = 2$, $m = 1$ and the interpolation and extrapolation is done with respect to R^2. The latter is

$$U_{\mathrm{m-q}}(R > R_M) = \frac{D_3}{R^3} + \frac{D_4}{R^4}, \tag{1.134}$$

i.e. $n = 2$, $m = 2$ and the interpolation and extrapolation is done with respect to R.

1.7.2 Integration of Schrödinger Equation

In Section 1.5, we discussed nuclear radial wave functions of three types of states: bound, continuum and quasibound. We showed the typical shapes of the wave functions and their characterisations. In this Subsection, their numerical computation will be discussed. The normalisations of continuum-state and bound-state wave functions are the same as in Equations (1.80) and (1.78), respectively.

Numerov Method

Ro-vibrational radial wave functions $\Psi(R)$ are solutions of Schrödinger equation (1.46). Because of different boundary conditions for bound- and continuum-state wave functions, we use two numerical methods. The first one is called the Numerov method [46] and is used for continuum-state wave functions $\psi(R)$.

In this method, a wave function is firstly expanded in a Taylor series in powers of integration step h

$$\psi(R+h) = \psi(R) + h\psi'(R) + \frac{h^2}{2}\psi^{(2)}(R) + \frac{h^3}{6}\psi^{(3)}(R) + \frac{h^4}{24}\psi^{(4)}(R) + \cdots . \tag{1.135}$$

Similarly, a Taylor series for $\psi(R-h)$ can be written. Then, after several steps one can derive a formula for $\psi_{n+1} \equiv \psi(R_{n+1})$

$$\psi_{n+1} = \frac{2\left(1 + \frac{5h^2}{12}k_n^2\right)\psi_n - \left(1 - \frac{h^2}{12}k_{n-1}^2\right)\psi_{n-1}}{1 - \frac{h^2}{12}k_{n+1}^2}, \tag{1.136}$$

where $k_n \equiv k(R_n)$, $R_n = R_0 + nh$ and

$$k^2(R) = \frac{2\mu}{\hbar^2}\left[U(R) - E\right] + \frac{J(J+1) - \Omega^2}{R^2}. \tag{1.137}$$

Evaluation starts for ψ_2 and larger n with the boundary condition

$$\psi(R_0 = 0) = 0, \tag{1.138}$$

which gives $\psi_0 = 0$, $\psi_1 =$ "very small number". In our in-house programme $\psi_1 = h^2/k_1^2$.

The Numerov method is a fifth order method, which makes it more precise than the quite famous fourth order Runge-Kutta (RK4), used in numerical integrations of differential equations. To avoid roundoff errors, it is advisable to use at least double precision in computer codes.

Numerov-Cooley Method

For the bound-state wave functions a modified Numerov method is used that can find those solutions for which $E < 0$ are bound-state energies. This is commonly known as the Numerov-Cooley method [47], whose point is to evaluate the wave function from Equation (1.136) (or in a similar form) employing the boundary conditions for bound states

$$\psi(R = 0) = 0, \tag{1.139}$$

$$\psi(R \to \infty) = 0. \tag{1.140}$$

This means that we can set $\psi(R = 0) = \psi_0 = 0$ and $\psi(R\,\text{very small}) = \psi_1 =$ "very small number" at the beginning of the so-called outward integration. Equation (1.136) is used step by step until the first maximum of the wave function at R_m is found. Then, an inward integration is performed, too, with $\psi(R \to \infty) \approx \psi_N = 0$, $\psi_{N-1} =$ "very small number". The aim is to obtain the same value (within the required precision) of ψ_m at R_m from both directions. However, we also need to match the derivatives of the wave function at the meeting point R_m from the both directions. The different slopes around the maximum entail the repetition of the whole procedure. Before another iteration, E is corrected to $E + D(E)$, which changes the values in Equation (1.137) and, thus, also in Equation (1.136). The energy correction $D(E)$ in our in-house programme is [47]

$$D(E) = \frac{\left(1 - \frac{h^2}{12}k_{m-1}^2\right)\psi_{m-1} - 2\left(1 + \frac{5h^2}{12}k_m^2\right)\psi_m + \left(1 - \frac{h^2}{12}k_{m+1}^2\right)\psi_{m+1}}{h^2\sum_{n=1}^{N-1}\psi_n\left[\left(\psi_{n-1} + \psi_{n+1}\right)\frac{1}{12} + \frac{5}{6}\psi_n\right]}. \tag{1.141}$$

Discrete Variable Representation Method

The bound-state wave functions can be calculated also by the discrete variable representation (DVR) method, which is described in [48] and therein references. Although this approach is used in the quantal computations of cross sections that are only compared to the semiclassical cross sections, we choose not to go into details because the quantual cross sections with the usage of the DVR method are only to check the correction of the semiclassical cross sections with the combination of the Breit-Wigner theory. On the other hand, the Numerov-Cooley method has been used in the computations of rate coefficients in the rest of our work.

In the DVR method, the bound-state wave function $\psi(R)$ is expanded in the orthonormal basis set

$$\phi_n(R) = \sqrt{\frac{2}{R_N - R_1}}\sin\frac{n\pi(R - R_1)}{R_N - R_1}. \tag{1.142}$$

The radial Schrödinger equation is then expressed in the matrix form for which the potential and kinetic energy matrix elements are

$$V_{ij}^{\mathrm{DVR}} = U(R_i)\delta_{ij}, \tag{1.143}$$

$$T_{ij}^{\mathrm{DVR}} = \frac{\hbar^2}{4\mu}\left(\frac{\pi}{R_N - R_1}\right)^2 \left[\frac{2N^2+1}{3} - \frac{1}{\sin^2\left(\frac{\pi i}{N}\right)}\right] \text{ if } i = j, \tag{1.144}$$

$$= \frac{\hbar^2}{4\mu}\left(\frac{\pi}{R_N - R_1}\right)^2 \left\{\frac{(-1)^{i-j}}{\sin^2\left[\frac{\pi(i-j)}{2N}\right]} - \frac{(-1)^{i-j}}{\sin^2\left[\frac{\pi(i+j)}{2N}\right]}\right\} \text{ if } i \neq j, \tag{1.145}$$

where

$$R_i = R_1 + \frac{R_N - R_1}{N} i. \tag{1.146}$$

1.7.3 Tunnelling Widths

The tunnelling widths of shape resonances $\Gamma^{\mathrm{tun}}_{v,J,\Omega}$, used throughout works [31],[33] and [30], were obtained by the LEVEL 7.7 computer programme [49]. This programme finds also the positions of shape resonances $E_{v,J,\Omega}$ and can compute the quasibound and bound-state wave functions characterised by v, J, Ω quantum numbers. The newer versions, from LEVEL 8.0 [63], can also calculate the Einstein A coefficients for spontaneous emission between two electronic states. This version was used in [34, 64].

1.7.4 Quadrature

In Subsection 1.7.2, we discussed integration methods for solving the Schrödinger equation. This Subsection discusses the quadrature methods for integrals used in this work.

The simplest integration method is probably the **trapezoidal rule**

$$\int_a^b f(x)\mathrm{d}x \approx h\left[\frac{1}{2}f(x_0) + f(x_1) + \cdots + f(x_{n-1}) + \frac{1}{2}f(x_n)\right], \tag{1.147}$$

where $h = (b-a)/n$ is an integration step and $x_i = a + ih$. The precision of this rule can be improved in some extent by making h very small. However, too small h means many intervals and evaluations of the $f(x_i)$ values. Consequently, the integration is performed rather slowly and the result can be affected by a large roundoff error.

The **Simpson's rule**

$$\int_a^b f(x)\mathrm{d}x \approx \frac{h}{3}\left[f(x_0) + 4f(x_1) + 2f(x_2) + 4f(x_3) + 2f(x_4) + \right.$$
$$\left. + \cdots + 4f(x_{n-1}) + f(x_n)\right], \tag{1.148}$$

is also commonly used. The same definitions of h and x_i are valid. Many improvements have been suggested to this rule, one of which is

$$\int_a^b f(x)\mathrm{d}x \approx \frac{h}{48}\left[17f(x_0)+59f(x_1)+43f(x_2)+49f(x_3)+48\sum_{i=4}^{n-4} f(x_i)+\right.$$
$$\left.+\,49f(x_{n-3})+43f(x_{n-2})+59f(x_{n-1})+17f(x_n)\right]. \tag{1.149}$$

Both the mentioned rules have the same weakness in the choice of h. In order to avoid this drawback one can use the **Romberg method**. Firstly, we approximate very poorly the integral

$$\int_a^b f(x)\mathrm{d}x \approx R_{1,1} = (b-a)\frac{f(b)-f(a)}{2} = h_1\frac{f(b)-f(a)}{2}, \tag{1.150}$$

which we denote $R_{1,1}$, and the integration step $h_1 = b-a$. The Romberg method is iterative in that respect that $R_{j,1}$ terms

$$R_{j,1} = \frac{1}{2}R_{j-1,1} + h_j\sum_{i=1}^{2^{j-2}} f\left[a+(2i-1)h_j\right] \tag{1.151}$$

are calculated with integration steps h_j

$$h_j = \frac{b-a}{2^{j-1}} \tag{1.152}$$

for $j \geq 2$ step by step. Simultaneously, improved integrals $R_{j,k}$ are computed from $R_{j,1}$ for $2 \leq k \leq j$:

$$R_{j,k} = \frac{4^{k-1}R_{j,k-1} - R_{j-1,k-1}}{4^{k-1}-1}. \tag{1.153}$$

The most precise integral is then $R_{j,j}$.

The integration over the internuclear distance in Equation (1.109) is performed by the Romberg method and the trapezoidal rule was used in the integration over the impact parameter b in Equation (1.109). The Simpson's rule was employed on the integrations over R in Equation (1.91), Equation (1.98), Equation (1.102) and Equation (1.118) for the transition dipole-moment matrix elements. The integrations over collision energy in Equation (1.82) was performed also by the Simpson's rule. Since the grid for RCT cross section in Equation (1.115) is very large, the simplest approximation

$$\int_a^b f(x)\mathrm{d}x \approx h\sum_{i=0}^{n} f(x_i) \tag{1.154}$$

can be used with a small error caused.

All the methods can be found in [65] except for the extended Simpson's rule in Equation (1.149), which can be found, for instance, in [66].

1.7.5 Hönl-London Factors

Hönl-London factors for Hund's case (a) and (b) molecules can be found in [67]. For singlet diatomic molecules, the Hönl-London factors for Hund's case (a) molecules for dipole and quadrupole transitions were derived in [68].

1.8 Studied Systems[†]

Two diatomic systems related to astrochemistry were chosen in this work: $HeLi^+$ and CO^+. The former is believed to have occurred during the recombination era of the Universe [5] in its excited electronic states. The latter occurs in comet tails, interstellar medium and higher layers of atmospheres of cool stars or planetary atmospheres. Although $HeLi^+$ has not been observed in this era, the studied processes on this system could occur in the interstellar medium and higher layers of stellar and planetary atmospheres. Therefore, the described theory and calculations are relevant to current astrochemistry as well.

1.8.1 $HeLi^+$

Molecular ion $HeLi^+$ was studied in this work in the following electronic states: $1^3\Pi$, $c^3\Sigma^+$, $b^3\Sigma^+$, $a^3\Sigma^+$, all of which are also illustrated in Figure 1.8 with the relevant transition dipole-moment functions. The *ab initio* data were obtained in [69]. The PECs characteristics are summarised also in Table 1.1. Concretely, the positions of global minima R_e of all the states and the local maximum of $1^3\Pi$ R_{loc} the dissociation energies D_e and the interaction energies at the local maximum $U(R_{loc})$ are given.

The $1^3\Pi$ and $c^3\Sigma^+$ states have the same dissociation limit and for $R \to \infty$ form $Li^+(1^1S)$ cation in its ground electronic state and $He(2^3P)$ in its first triplet-P excited electronic state. The $1^3\Pi$ state has a barrier of 64.9 cm^{-1} height at 18.99 a_0, consequently this PEC supports at least one shape resonance with $J = 0$. LEVEL 7.7 found two rotationless shape resonances: $v = 19, E = 0.477\,308$ cm^{-1}, $\Gamma^{tun}_{19,0} = 1.5 \times 10^{-40}$ cm^{-1}; $v = 20, E = 42.209\,775$ cm^{-1}, $\Gamma^{tun}_{20,0} = 5.898 \times 10^{-5}$ cm^{-1}.

The $c^3\Sigma^+$ state has a shallow well. However, if compared to the well of the $b^3\Sigma^+$ state, one can see the well of the $b^3\Sigma^+$ state is even shallower. Both these states support ro-vibrational bound states. The $b^3\Sigma^+$ state's dissociation limit differs only in the excitation of He atom, which is in its lower triplet state, $He(2^3S)$. This means RCT cannot be studied between the $1^3\Pi$ and $b^3\Sigma^+$ or the $c^3\Sigma^+$ and $b^3\Sigma^+$ states since there is no charge exchange.

The lowest triplet state is the $a^3\Sigma^+$ state and has the deepest well and, thus, supports the greatest number of ro-vibrational bound states. This state dissociates into the ground lithium atom, $Li(2^2S)$, and hellium cation in its ground electronic state, $He^+(1^2S)$. Therefore, RCT can be studied between the continua of the $b^3\Sigma^+$ and $a^3\Sigma^+$ states, or of the $1^3\Pi$ (or $c^3\Sigma^+$) and $a^3\Sigma^+$. However, notice that the integration over emitted photon frequency in Equation (1.115) can limit the choice of studied processes in respect of the energy difference at $R \to \infty$. For some electronic states a RCT calculation can be very time consuming. RA computations do not have this disadvantage and can occur between any states with the only condition that the final state has bound states and some of its bound ro-vibrational states lay bellow the initial state.

[†]The *ab initio* calculations on both the $HeLi^+$ and CO^+ systems were performed by my supervisor Pavel Soldán.

Figure 1.8: Top - The potential energy curves of the $1^3\Pi$, $c^3\Sigma^+$, $b^3\Sigma^+$, and $a^3\Sigma^+$ electronic states of the $HeLi^+$ molecular ion are illustrated; Middle - Transition dipole-moment functions $d_\alpha(R)$ for transitions restricted to $^3\Sigma^+$ symmetry compared with the dipole moment of $1^3\Pi$; Bottom - Transition dipole-moment functions for transitions with the $\Pi \rightarrow \Sigma$ symmetry compared with the dipole moment of $1^3\Pi$. The dipole moment of $1^3\Pi$ state is in the middle and bottom panels for better comparison.

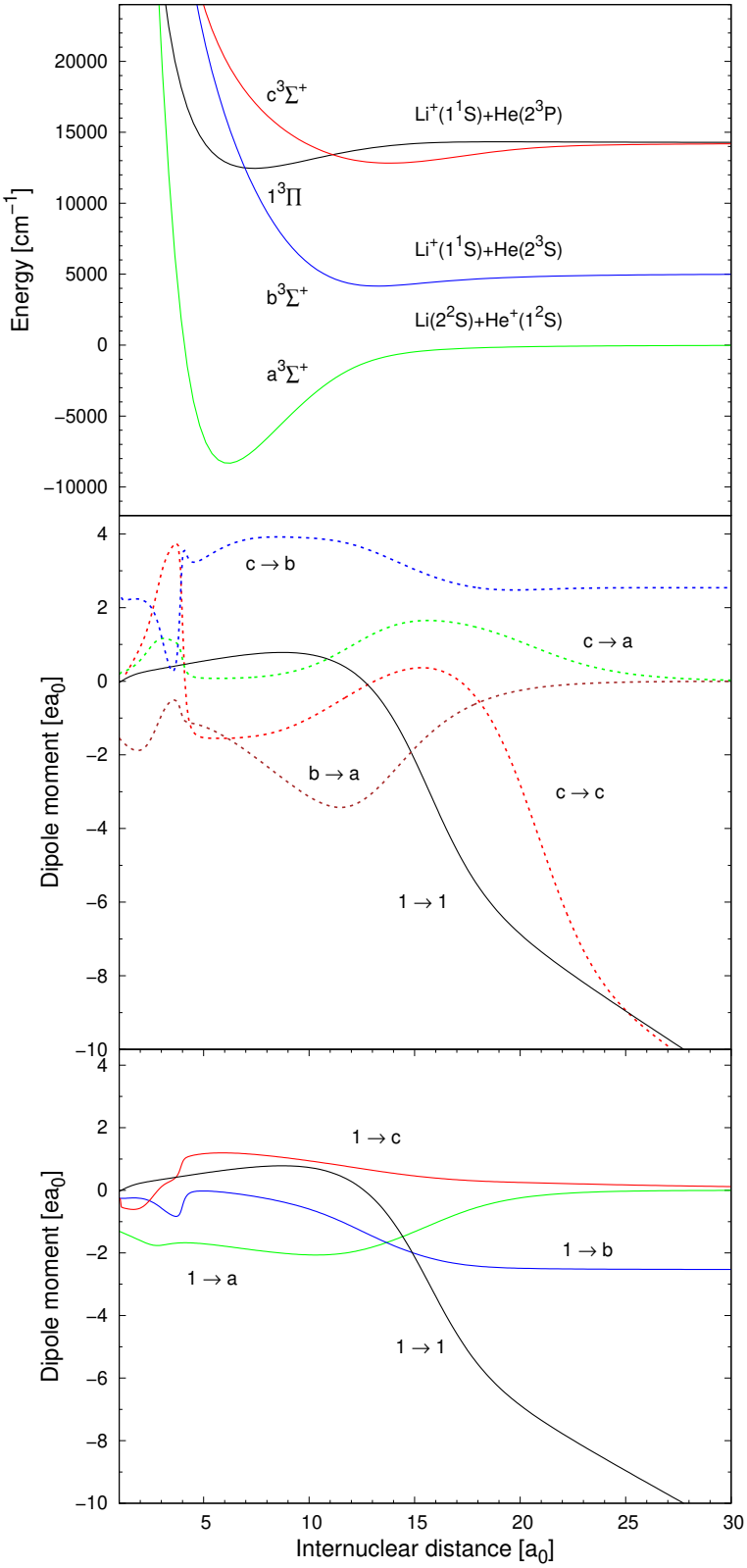

Table 1.1: Minima and local extrema on potential energy curves are summarised for the lowest triplet states of $HeLi^+$: $a^3\Sigma^+$, $b^3\Sigma^+$, $c^3\Sigma^+$ and $1^3\Pi$. The values are taken from [69] and [31].[a]

state	R_e $[a_0]$	D_e $[cm^{-1}]$	R_{loc} $[a_0]$	$U(R_{loc})$ $[cm^{-1}]$
$a^3\Sigma^+$	6.164	8 328.0	-	-
$b^3\Sigma^+$	13.221	872.4	-	-
$c^3\Sigma^+$	13.808	1 438.7	-	-
$1^3\Pi$	7.383	1 802.1	18.99	64.9

[a] R_e and D_e denote the internuclear distance at the global minimum and the depth of the well in respect to the corresponding dissociation. R_{loc} and $U(R_{loc})$ denote the internuclear distance at local extrema and the values of interaction energies $U(R_{loc})$ at that distance.

Table 1.2: Minima and local extrema on potential energy curves are summarised for the lowest doublet states of CO^+: $X^2\Sigma^+$, $A^2\Pi$, $C^2\Delta$, $D^2\Pi$, $1^2\Sigma^-$ and $2^2\Sigma^-$. The values are from [34, 64].

state	R_e $[a_0]$	D_e $[cm^{-1}]$	R_{loc} $[a_0]$	$U(R_{loc})$ $[cm^{-1}]$
$X^2\Sigma^+$	2.110	68 043.1	8.938	49.3
$A^2\Pi$	2.353	47 564.9	-	-
$C^2\Delta$	2.562	5 279.7	3.740	-342.9
			3.963	-449.6
			8.523	53.8
$D^2\Pi$	3.539	3 921.1	2.380	-186.1
			2.745	4 546.3
			8.995	44.1
$1^2\Sigma^-$	2.565	5 749.1	3.755	-280.2
			5.730	-1 121.9
$2^2\Sigma^-$	5.051	132.2	2.947	7 021.5
			3.618	10 628.7
			8.069	60.9

1.8.2 CO^+

Only RA was studied on the CO^+ molecular ion. Seven most imporant channels were studied involving these electronic states: $D^2\Pi$, $C^2\Delta$, $2^2\Sigma^-$, $1^2\Sigma^-$, $A^2\Pi$ and $X^2\Sigma^+$. All the states are illustrated in Figure 1.9 (from [34]) together with the diabatic continuation of $D^2\Pi$, denoted $\widetilde{D}^2\Pi$. $D^2\Pi$ has an avoided crossing with $3^2\Pi$ around 2.745 a_0. The $2^2\Sigma^-$ states has an avoided crossing with $3^2\Sigma^-$ (not shown in the Figure) around 3.618 a_0. More electronic states of CO^+ can be found in Fig. 2 in [70].

In the bottom panel of Figure 1.9 (from [34]), the dipole-moment functions of interest are depicted.

The PECs characteristics are summarised in Table 1.2. The $A^2\Pi$ and $1^2\Sigma^-$ states are attractive in the long range. The $X^2\Sigma^+$, $C^2\Delta$, $D^2\Pi$ and $2^2\Sigma^-$ states are repulsive in the long range and have a barrier.

Figure 1.9: Top - The potential energy curves of six electronic states involved in radiative association study of CO^+. $\tilde{D}^2\Pi$ denotes the diabatic continuation of the $D^2\Pi$ state for small internuclear distances before the avoided crossing with $3^2\Pi$. Bottom - Transition dipole moments of all studied processes. These data are taken from [34, 64].

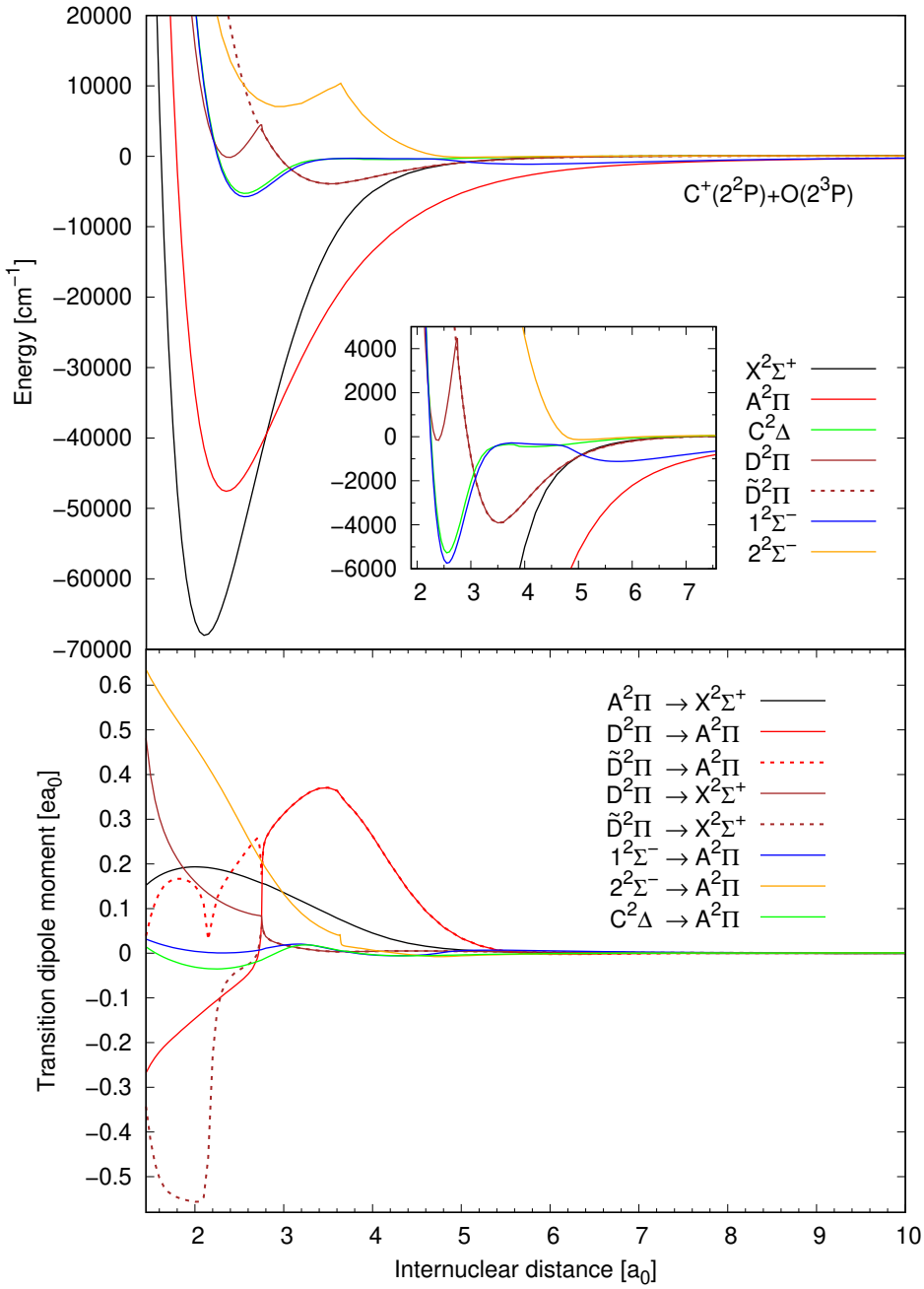

2. Results

2.1 Radiative Lifetimes

Radiative lifetimes (RLTs) of ro-vibrational bound states were calculated for $HeLi^+$ in its $b^3\Sigma^+$ electronic state. We neglect relativistic effects; therefore, the only deexcitation channel is the $a^3\Sigma^+$ state. In this Section, we will omit Ω_i and Ω_f indices because the spinless approximation has been used, where $\Omega = \Lambda + \Sigma = \Lambda + 0 = \Lambda = 0$ for Σ states. Since $\Delta\Lambda = 0$ for the $^3\Sigma^+ \to {}^3\Sigma^+$ transitions, we can write

$$T_q^1\left[\mathbf{d}(R)\right] = T_0^1\left[\mathbf{d}(R)\right] = d_z(R). \tag{2.1}$$

The Hönl-London factors for the $^3\Sigma^+ \to {}^3\Sigma^+$ transitions are

$$S_{J_i,J_f=J_i+1} = J_i + 1, \quad S_{J_i,J_f=J_i} = 0, \quad S_{J_i,J_f=J_i-1} = J_i. \tag{2.2}$$

In the RLTs calculations, the collision probability is usually written in the form

$$p_i = \frac{1}{g_i(2J_i+1)}, \tag{2.3}$$

where g_i denotes the degeneracy of the initial state, which is $g_i = 3$ for $b^3\Sigma^+$. The factor $2J_i+1$ in the denominator averages the radiative width over the number of rotational states at a given vibrational level. This Section summarises the main results from [32] and adds also the unpublished results of this study.

The potential energy curves (PECs) of the two involved states, $b^3\Sigma^+$ and $a^3\Sigma^+$, are plotted in the top panel in Figure 1.8 by the blue and green colours. They were extrapolated to

$$U(R \text{ large}) = \frac{D_4}{R^4} + \frac{D_6}{R^6} \tag{2.4}$$

where $D_4 = -157.815\,734\ E_\mathrm{h}a_0^4$ and $D_4 = -81.435\ E_\mathrm{h}a_0^4$ are the coefficients for the $b^3\Sigma^+$ and $a^3\Sigma^+$ states, respectively, taken from [71]. From Equation (1.74) for the static polarisability α_1, we know that $D_4 = \alpha_1/2$. The D_4 coefficients were, therefore, found to match the static dipole polarisabilities $\alpha_\mathrm{d}[\mathrm{He}(2^3\mathrm{S})] = 315.631\,468\ e^2a_0^2/E_\mathrm{h}$ [72] and $\alpha_\mathrm{d}[\mathrm{Li}(2^2\mathrm{S})] = 162.87\ e^2a_0^2/E_\mathrm{h}$ [73]. The extrapolation of $d_z(R)$, illustrated in the middle panel of Figure 1.8, was taken from [8], too.

Figure 1.8 shows that the Franck-Condon (FC) overlaps do not seem to be large. The minima of the electronic states are shifted by $\approx 7.056\ a_0$. The difference between their dissociation limits is $\Delta E = 0.623\,941$ eV $\approx 5\,032.4$ cm^{-1}. The transition dipole-moment function is illustrated in the same Figure in the middle panel by the brown line. For large R, it approaches zero. It is noticeable that the maximum values of $d_z(R)$ are around the internuclear distances where the $b^3\Sigma^+$ PEC has also its minimum. Around the minimum of the final state, $d_z(R)$ is nonzero. These two factors can enlarge the dipole-moment matrix elements ($M_{v_i,J_i;v_f,J_f}$ and/or $M_{v_i,J_i;E_f,J_f}$).

The deexcitation of a bound state v_i, J_i of $b^3\Sigma^+$ can end either in a bound state or a continuum state of $a^3\Sigma^+$. In Subsection 1.6.1, these are called bound-bound (BB) and bound-free (BF) processes, respectively. The $b^3\Sigma^+$ state has 1 289 bound states. The RLTs were calculated only for the lowest rotational quantum numbers: $J_i = 0, 1, 2$. Because there are 33 vibrational levels for $J_i = 0$ and $J_i = 1$ and 32 vibrational levels for $J_i = 2$, the RLTs were calculated only for 98 ro-vibrational bound states. The $a^3\Sigma^+$ state has a quite deep well due to which it can support 4 176 bound states. For $J_f = 0, 1$, it has 61 vibrational levels. For $J_f = 2, 3$ only 60 levels. $J_f = 3$ is the maximum J_f included in the RLTs computations for $J_i \leq 2$. This, together with Hönl-London factors (2.2), entails the sum in Equation (1.89) contains 61 terms for $J_i = 0$ and 121 terms for each $J_i = 1, 2$. The final electronic state supports shape resonances with the lowest rotational quantum number equal to 4. Because the Hönl-London factors are nonzero for $J_f = J_i \pm 1$ and the RLTs were calculated for $J_i \leq 2$, then the quasi-bound states in the BF transitions and their treatment is not the subject of this study.

2.1.1 Lifetimes of $HeLi^+$, $J_i = 0$

Table 2.1 summarises the results for the rotationaless $HeLi^+(b^3\Sigma^+)$ in the left six columns. The energy of all 33 vibrational levels with $J_i = 0$ are given in the second column. In the following two columns, the radiative widths for the BB and BF transitions are shown, respectively. Their sum gives the total radiative width, which can be found in the fifth column. The RLTs are in the sixth column.

The BB contributions are much larger than the BF contributions for low v_i. With increasing v_i, however, the BB contribution decreases and the BF contribution increases. For large v_i their difference is only one order of magnitude. The BB radiative widths contribute expectedly more to the total radiative width partly because $\omega_{v_i,0;v_f,J_f} > \omega_{v_i,0;E_f,J_f}$, which appear in Equation (1.89) and Equation (1.96) in the third power. The total radiative width follows the same tendency as the largest contribution, $\Gamma^{\mathrm{BB}}_{v_i,0}$. The resulting RLTs are then the shortest for the lowest vibrational quantum numbers and they increase with increasing v_i.

The BB transitions $v_i, J_i = 0 \rightarrow v_f, J_f = 1$ were studied more through evaluating $M_{v_i,0;v_f,1}$ and $\hbar A^{\mathrm{BB}}_{v_i,0;v_f,1}$ for $v_i = 0$ and $v_i = 29$. The $M_{v_i,0;v_f,1}$ values are in the top panels of Figure 2.1. For $v_i = 0$, the values are shown on the left-hand side and are larger one order of magnitude from the values for $v_i = 29$ which are shown on the right-hand side. Further, $\left|M_{0,0;v_f,1}\right| > 1$ for $v_f = 32 - 35$, but $\left|M_{29,0;v_f,1}\right| < 0.4$ for all v_f. In Equation (1.89) and Equation (1.96), the matrix elements are squared, which means they are squared also in $\hbar A^{\mathrm{BB}}_{v_i,0;v_f,1}$. Therefore, $\hbar A^{\mathrm{BB}}_{v_i,0;v_f,1}$ values are much larger for $v_i = 0$ than for $v_i = 29$. They are illustrated in the bottom panels where it can be seen that the difference is three orders of magnitude. This is in correspondance with Table 2.1. The reason is that $d_z(R)$ is the largest around the minimum of the initial ro-vibrational state, $v_i = 0, J_i = 0$, where the wave function of the initial state is also the largest. However, $d_z(R)$ is small for $R > 20\ a_0$, even smaller than at the internuclear distance corresponding to the minimum of the final electronic state. $\hbar A^{\mathrm{BB}}_{v_i,0;v_f,1}$ can be understood also as a radiative width for BB transition $v_i, J_i = 0 \rightarrow v_f, J_f = 1$.

The BF transitions $v_i, J_i = 0 \rightarrow E_f, J_f = 1$ were studied for $v_i = 0, 1, 2$. Firstly,

Table 2.1: Radiative lifetimes [s] of $HeLi^+(b^3\Sigma^+)$ of $v_i, J_i = 0$ in the sixth column, of $v_i, J_i = 1$ in the 11th column, of $v_i, J_i = 2$ in the 16th column. The radiative widths $[E_h]$ with their bound-bound (BB) and bound-free (BF) contributions are shown too. The bound-state energies $[cm^{-1}]$ are in the second, 7th and 12th columns, respectively. For given v_i and different J_i, the $\Gamma^{BB}_{v_i,J_i}$, $\Gamma^{BF}_{v_i,J_i}$, Γ_{v_i,J_i} and τ_{v_i,J_i} values are similar. These values start to differ from $v_i \approx 23$ with increasing v_i.

v_i	$E_{v_i,0}$	$\Gamma^{BB}_{v_i,0}$	$\Gamma^{BF}_{v_i,0}$	$\Gamma_{v_i,0}$	$\tau_{v_i,0}$	$E_{v_i,1}$	$\Gamma^{BB}_{v_i,1}$	$\Gamma^{BF}_{v_i,1}$	$\Gamma_{v_i,1}$	$\tau_{v_i,1}$	$E_{v_i,2}$	$\Gamma^{BB}_{v_i,2}$	$\Gamma^{BF}_{v_i,2}$	$\Gamma_{v_i,2}$	$\tau_{v_i,2}$
0	-829.6309	1.86(-11)	2.90(-20)	1.86(-11)	1.30(-6)	-829.3636	1.85(-11)	2.87(-20)	1.85(-11)	1.30(-6)	-828.8291	1.85(-11)	2.81(-20)	1.85(-11)	1.30(-6)
1	-746.7588	1.80(-11)	1.80(-18)	1.80(-11)	1.34(-6)	-746.4979	1.80(-11)	1.83(-18)	1.80(-11)	1.35(-6)	-745.9760	1.80(-11)	1.89(-18)	1.80(-11)	1.35(-6)
2	-668.5136	1.73(-11)	2.11(-17)	1.73(-11)	1.40(-6)	-668.2595	1.73(-11)	2.10(-17)	1.73(-11)	1.40(-6)	-667.7513	1.73(-11)	2.06(-17)	1.73(-11)	1.40(-6)
3	-595.0019	1.65(-11)	1.27(-16)	1.65(-11)	1.46(-6)	-594.7553	1.65(-11)	1.29(-16)	1.65(-11)	1.46(-6)	-594.2621	1.65(-11)	1.35(-16)	1.65(-11)	1.46(-6)
4	-526.3181	1.57(-11)	1.64(-15)	1.57(-11)	1.54(-6)	-526.0795	1.57(-11)	1.64(-15)	1.57(-11)	1.54(-6)	-525.6023	1.57(-11)	1.65(-15)	1.57(-11)	1.54(-6)
5	-462.5375	1.47(-11)	2.94(-15)	1.47(-11)	1.64(-6)	-462.3075	1.47(-11)	2.93(-15)	1.47(-11)	1.64(-6)	-461.8476	1.47(-11)	2.92(-15)	1.47(-11)	1.64(-6)
6	-403.7099	1.37(-11)	2.07(-14)	1.37(-11)	1.76(-6)	-403.4891	1.37(-11)	2.10(-14)	1.37(-11)	1.76(-6)	-403.0476	1.37(-11)	2.16(-14)	1.37(-11)	1.76(-6)
7	-349.8497	1.26(-11)	6.59(-14)	1.27(-11)	1.91(-6)	-349.6387	1.26(-11)	6.57(-14)	1.27(-11)	1.91(-6)	-349.2168	1.26(-11)	6.52(-14)	1.27(-11)	1.91(-6)
8	-300.9258	1.15(-11)	7.68(-14)	1.16(-11)	2.09(-6)	-300.7251	1.15(-11)	7.69(-14)	1.16(-11)	2.09(-6)	-300.3239	1.15(-11)	7.72(-14)	1.16(-11)	2.09(-6)
9	-256.8505	1.03(-11)	2.46(-13)	1.05(-11)	2.30(-6)	-256.6606	1.03(-11)	2.48(-13)	1.05(-11)	2.30(-6)	-256.2809	1.03(-11)	2.54(-13)	1.05(-11)	2.30(-6)
10	-217.4737	8.98(-12)	4.64(-13)	9.44(-12)	2.56(-6)	-217.2950	8.97(-12)	4.64(-13)	9.44(-12)	2.56(-6)	-216.9376	8.97(-12)	4.63(-13)	9.43(-12)	2.56(-6)
11	-182.5859	7.96(-12)	4.44(-13)	8.40(-12)	2.88(-6)	-182.4185	7.95(-12)	4.42(-13)	8.40(-12)	2.88(-6)	-182.0839	7.95(-12)	4.39(-13)	8.39(-12)	2.88(-6)
12	-151.9304	6.93(-12)	4.86(-13)	7.41(-12)	3.26(-6)	-151.7746	6.92(-12)	4.88(-13)	7.41(-12)	3.27(-6)	-151.4630	6.91(-12)	4.92(-13)	7.40(-12)	3.27(-6)
13	-125.2203	5.87(-12)	6.02(-13)	6.48(-12)	3.74(-6)	-125.0760	5.87(-12)	6.04(-13)	6.47(-12)	3.74(-6)	-124.7876	5.85(-12)	6.08(-13)	6.46(-12)	3.74(-6)
14	-102.1505	5.00(-12)	5.99(-13)	5.60(-12)	4.32(-6)	-102.0178	5.00(-12)	6.00(-13)	5.60(-12)	4.32(-6)	-101.7524	4.99(-12)	6.00(-13)	5.59(-12)	4.33(-6)
15	-82.40176	4.27(-12)	5.23(-13)	4.80(-12)	5.04(-6)	-82.28039	4.27(-12)	5.23(-13)	4.79(-12)	5.05(-6)	-82.03778	4.26(-12)	5.22(-13)	4.79(-12)	5.05(-6)
16	-65.64634	3.63(-12)	4.42(-13)	4.07(-12)	5.94(-6)	-65.53611	3.62(-12)	4.42(-13)	4.07(-12)	5.95(-6)	-65.31575	3.62(-12)	4.41(-13)	4.06(-12)	5.96(-6)
17	-51.57215	3.04(-12)	3.71(-13)	3.41(-12)	7.09(-6)	-51.47277	3.04(-12)	3.70(-13)	3.41(-12)	7.10(-6)	-51.27413	3.03(-12)	3.70(-13)	3.40(-12)	7.11(-6)
18	-39.98416	2.52(-12)	3.07(-13)	2.83(-12)	8.56(-6)	-39.79530	2.52(-12)	3.07(-13)	2.82(-12)	8.57(-6)	-39.61772	2.51(-12)	3.06(-13)	2.82(-12)	8.59(-6)
19	-30.30076	2.06(-12)	2.50(-13)	2.31(-12)	1.05(-5)	-30.22205	2.05(-12)	2.49(-13)	2.30(-12)	1.05(-5)	-30.06476	2.05(-12)	2.48(-13)	2.30(-12)	1.05(-5)
20	-22.55568	1.65(-12)	1.99(-13)	1.85(-12)	1.31(-5)	-22.48669	1.65(-12)	1.99(-13)	1.85(-12)	1.31(-5)	-22.34886	1.65(-12)	1.98(-13)	1.84(-12)	1.31(-5)
21	-16.39917	1.30(-12)	1.57(-13)	1.46(-12)	1.66(-5)	-16.33943	1.30(-12)	1.56(-13)	1.46(-12)	1.66(-5)	-16.22010	1.30(-12)	1.55(-13)	1.45(-12)	1.66(-5)
22	-11.59850	1.01(-12)	1.20(-13)	1.13(-12)	2.14(-5)	-11.54749	1.01(-12)	1.20(-13)	1.13(-12)	2.15(-5)	-11.44563	1.00(-12)	1.19(-13)	1.12(-12)	2.16(-5)
23	-7.938604	7.59(-13)	9.05(-14)	8.50(-13)	2.85(-5)	-7.895770	7.57(-13)	9.02(-14)	8.48(-13)	2.85(-5)	-7.810275	7.53(-13)	8.96(-14)	8.43(-13)	2.87(-5)
24	-5.222585	5.55(-13)	6.60(-14)	6.21(-13)	3.89(-5)	-5.187331	5.53(-13)	6.57(-14)	6.19(-13)	3.91(-5)	-5.117005	5.50(-13)	6.52(-14)	6.15(-13)	3.93(-5)
25	-3.272019	3.91(-13)	4.64(-14)	4.37(-13)	5.53(-5)	-3.243711	3.89(-13)	4.62(-14)	4.36(-13)	5.55(-5)	-3.187285	3.86(-13)	4.57(-14)	4.32(-13)	5.60(-5)
26	-1.927175	2.63(-13)	3.12(-14)	2.94(-13)	8.23(-5)	-1.905141	2.61(-13)	3.10(-14)	2.92(-13)	8.27(-5)	-1.861273	2.59(-13)	3.06(-14)	2.89(-13)	8.37(-5)
27	-1.047121	1.66(-13)	1.97(-14)	1.86(-13)	1.30(-4)	-1.030654	1.65(-13)	1.96(-14)	1.85(-13)	1.31(-4)	-0.997929	1.63(-13)	1.92(-14)	1.82(-13)	1.33(-4)
28	-0.509753	9.70(-14)	1.15(-14)	1.08(-13)	2.23(-4)	-0.475040	9.59(-14)	1.13(-14)	1.07(-13)	2.26(-4)	-0.475040	9.37(-14)	1.11(-14)	1.05(-13)	2.31(-4)
29	-0.211758	5.02(-14)	5.94(-15)	5.61(-14)	4.31(-4)	-0.204157	4.93(-14)	5.84(-15)	5.51(-14)	4.39(-4)	-0.189189	4.75(-14)	5.62(-15)	5.31(-14)	4.55(-4)
30	-0.068538	2.16(-14)	2.55(-15)	2.41(-14)	1.00(-3)	-0.064166	2.09(-14)	2.47(-15)	2.33(-14)	1.04(-3)	-0.055671	1.95(-14)	2.31(-15)	2.18(-14)	1.11(-3)
31	-0.014103	6.61(-15)	7.82(-16)	7.39(-15)	3.27(-3)	-0.012111	6.14(-15)	7.26(-16)	6.86(-15)	3.52(-3)	-0.008395	5.19(-15)	6.14(-16)	5.81(-15)	4.17(-3)
32	-0.000959	8.97(-16)	1.06(-16)	1.03(-15)	2.41(-2)	-0.000463	6.45(-16)	7.63(-17)	7.21(-16)	3.35(-2)					

[a] $x(-y) \equiv x \times 10^{-y}$

Figure 2.1: Top panel - The elements of the dipole-moment matrix $M_{0,0;v_f,1}$ and $M_{29,0;v_f,1}$ of HeLi$^+$ on the left and right-hand side, respectively; bottom panel - the radiative widths corresponding to bound-bound transitions $v_i = 0, 29; J_i = 0 \rightarrow v_f, J_f = 1$, or $\hbar A_{0,0;v_f,1}$ and $\hbar A_{29,0;v_f,1}$. On x axis are vibrational quantum numbers of final states. The Figure was published in [32].

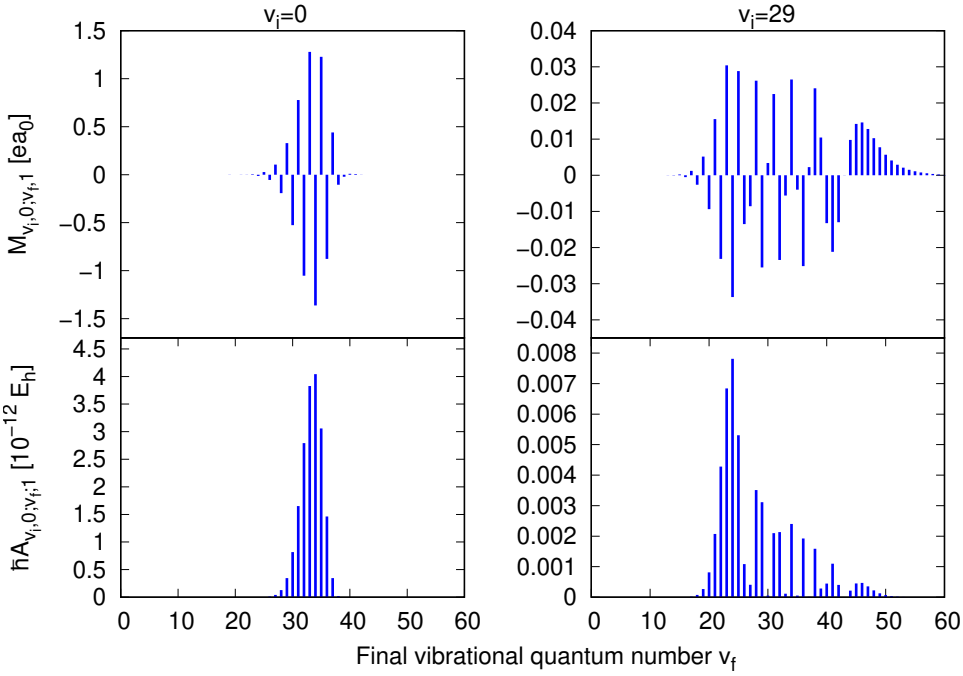

the absolute values $\left|M_{v_i,0;E_f,1}\right|$ for $v_i = 0, 2$ are illustrated in Firgure 2.2. From $\Gamma^{\mathrm{BF}}_{v_i,0}$ in Table 2.1, it can be guessed that the contributions for $v_i = 0$ should be the smallest ones. This is clearly seen also in Figure 2.2 by the red line when compared to the blue line corresponding to $\left|M_{2,0;E_f,1}\right|$. The elements for $v_i = 1$ have amplitudes between $\left|M_{0,0;E_f,1}\right|$ and $\left|M_{2,0;E_f,1}\right|$ and in order to keep the Figure clear, $\left|M_{1,0;E_f,1}\right|$ is not shown here.

In Figure 2.3, the radiative widths for BF transitions $v_i, J_i = 0 \rightarrow E_f, J_f = 1$ are illustrated, specifically for $v_i = 0, 1, 2$. Here $\hbar A_{0,0;E_f,1}$ cannot be plotted with $\hbar A_{1,0;E_f,1}$ and $\hbar A_{2,0;E_f,1}$ because of the significantly different values. Therefore, $\hbar A_{0,0;E_f,1}$ is illustrated in the left-hand panel. In the right-hand panel, $\hbar A_{1,0;E_f,1}$ and $\hbar A_{2,0;E_f,1}$ are in green and blue colours, respectively. Although they are of the same order of magnitude at small E_f, the rise of $\hbar A_{2,0;E_f,1}$ with larger v_i is obvious here as well.

RLTs for large E_{v_i,J_i} depend quite significantly on the quality of the extrapolated *ab initio* data. Therefore, methods with high precision of long range are recommended.

2.1.2 Lifetimes of HeLi$^+$, $\mathbf{J_i = 1, 2}$

The RLTs for $J_i = 1, 2$ are very similar to those for $J_i = 0$. Therefore, the results for $J_i = 1$ were only compared in [32] but not described in detail. We summarise them here in the middle of Table 2.1.

For $J_i = 1$, b$^3\Sigma^+$ still has 33 vibrational levels. The radiative widths and

Figure 2.2: Absolute values of the elements of the dipole-moment matrix $\left|M_{v_i,0;E_f,1}\right|$ are illustrated for $v_i = 0, 2$ and for final continuum-state energies $0\ E_\mathrm{h} \leq E_f \leq 0.002\ E_\mathrm{h}$ for HeLi$^+$; in the inner panel, it is for energies $0.006\ E_\mathrm{h} \leq E_f \leq 0.014\ E_\mathrm{h}$ in order to show that the values become comparable at these large E_f values.

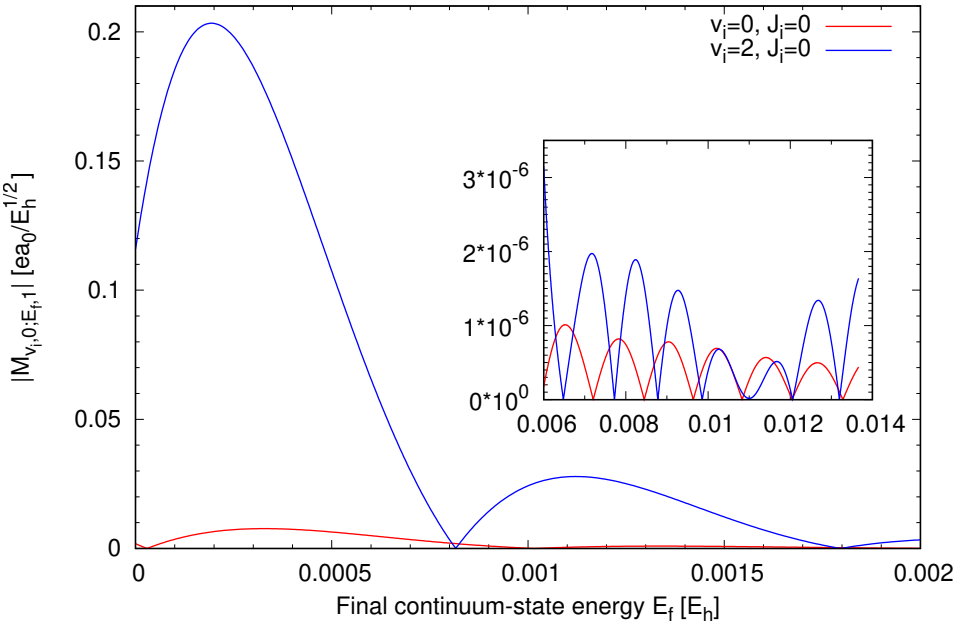

Figure 2.3: Contributions $\hbar A_{v_i,0;E_f,1}$ of HeLi$^+$ for $v_i = 0, 1, 2$ are illustrated.

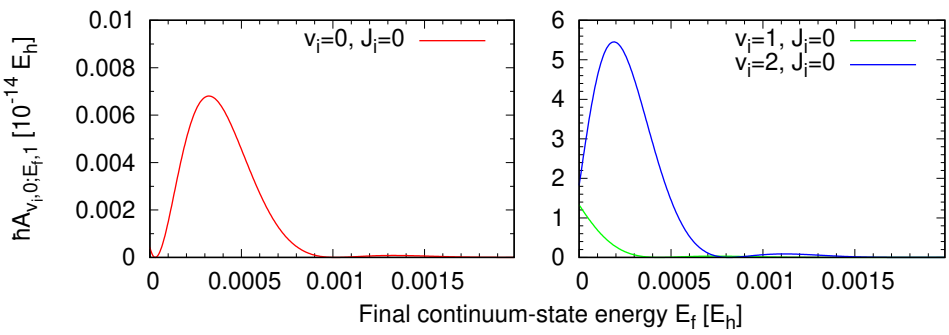

their BB and BF contributions are either the same or slightly smaller than the corresponding radiative widths for the rotationless $HeLi^+$. Thus, the lifetimes are a bit longer or the same.

For $J_i = 2$, there are 32 vibrational levels. Their total radiative widths and RLTs are shown on the right-hand side of Table 2.1. The radiative widths and hence the RLTs are again very similar to those for $J_i = 0, 1$. The RLTs of ro-vibrational states with $v_i = 0, J_i = 0, 1, 2$ are equal to 1.30×10^{-6} s. The results start to differ for $v_i \geq 12$. The trend with increasing v_i is the same as it was for $J_i < 2$. The RLTs are longer with increasing v_i. The same can be said when we compare three RLTs for $v_i =$ fixed and different J_i: The RLTs tend to prolong with larger J_i.

2.2 Radiative Association

2.2.1 $HeLi^+$

This Subsection shows the results of [30] and [31] with the emphasis on the second work. In [30], the depopulation of $c^3\Sigma^+$ state was calculated through the three following processes

$$c^3\Sigma^+[Li^+(1^1S) + He(2^3P)] \to a^3\Sigma^+, \tag{2.5}$$
$$c^3\Sigma^+[Li^+(1^1S) + He(2^3P)] \to b^3\Sigma^+, \tag{2.6}$$
$$c^3\Sigma^+[Li^+(1^1S) + He(2^3P)] \to c^3\Sigma^+. \tag{2.7}$$

In [31], the radiative association (RA) processes

$$1^3\Pi[Li^+(1^1S) + He(2^3P)] \to a^3\Sigma^+, \tag{2.8}$$
$$1^3\Pi[Li^+(1^1S) + He(2^3P)] \to b^3\Sigma^+, \tag{2.9}$$
$$1^3\Pi[Li^+(1^1S) + He(2^3P)] \to c^3\Sigma^+, \tag{2.10}$$

restricted to $\Pi \to \Sigma^+$ were studied.

Here, we also show unpublished results for the following processes

$$c^3\Sigma^+[Li^+(1^1S) + He(2^3P)] \to 1^3\Pi, \tag{2.11}$$
$$1^3\Pi\ [Li^+(1^1S) + He(2^3P)] \to 1^3\Pi. \tag{2.12}$$

The PECs are illustrated in the top panel of Figure 1.8. The leading term in RP-RKHS extrapolation of $c^3\Sigma^+$ and $1^3\Pi$ is

$$U(R \text{ large}) = \frac{D_3}{R^3} + \frac{D_4}{R^4}, \tag{2.13}$$

where for the $c^3\Sigma^+$ state $D_3 = -10.476\,4\ E_h a_0^3$ and for the $1^3\Pi$ state $D_3 = 5.071\,56\ E_h a_0^3$.

Transition dipole moments (TDMs) and dipole moments (DMs) are depicted in the middle and bottom panels of Figure 1.8. For the $c^3\Sigma^+ \to {}^3\Sigma^+$ transitions,

Table 2.2: Hönl-London factors for processes involving the $^3\Pi$ and $^3\Sigma^+$ symmetries are summarised.

Process	$\Omega_i \to \Omega_f$	$J_f = J_i + 1$	$J_f = J_i$	$J_f = J_i - 1$
$^3\Pi \to {}^3\Pi$	$0 \to 0$	$2(J_i + 1)$	0	$2J_i$
	$1 \to 1$	$2\frac{J_i(J_i+2)}{J_i+1}$	$2\frac{2J_i+1}{J_i(J_i+1)}$	$2\frac{(J_i-1)(J_i+1)}{J_i}$
	$2 \to 2$	$2\frac{(J_i-1)(J_i+3)}{J_i+1}$	$8\frac{2J_i+1}{J_i(J_i+1)}$	$2\frac{(J_i-2)(J_i+2)}{J_i}$
$^3\Pi \to {}^3\Sigma^+$	$0 \to 1$	$J_i + 2$	$2(J_i + 1)$	$J_i - 1$
	$1 \to 0$	J_i	$2(J_i + 1)$	$J_i + 1$
	$2 \to 1$	$\frac{J_i(J_i-1)}{J_i+1}$	$\frac{(2J_i+1)(J_i+2)(J_i-1)}{J_i(J_i+1)}$	$\frac{(J_i+1)(J_i+2)}{J_i}$
$^3\Sigma^+ \to {}^3\Pi$	$0 \to 1$	$J_i + 2$	$2J_i + 1$	$J_i - 1$
	$1 \to 0$	J_i	$2J_i + 1$	$J_i + 1$
	$1 \to 2$	$\frac{(J_i+2)(J_i+3)}{J_i+1}$	$\frac{(2J_i+1)(J_i-1)(J_i+2)}{J_i(J_i+1)}$	$\frac{(J_i-2)(J_i-1)}{J_i}$

Equation (2.1) is valid and the Hönl-London factors are also shown in Equation (2.2). For the one-electronic-state $1^3\Pi \to 1^3\Pi$ transition, Equation (2.1) is still valid, but the Hönl-London factors change. Their values for each Ω-transition are in Table 2.2. For the $^3\Pi \to {}^3\Sigma^+$ and the opposite transitions,

$$T^1_q\left[\mathbf{d}(R)\right] = T^1_{\pm 1}\left[\mathbf{d}(R)\right] = \mp\frac{1}{\sqrt{2}}\left[d_x(R) \pm i d_y(R)\right], \tag{2.14}$$

for which we need to know $d_x(R)$ and $d_y(R)$. In linear systems, however, $d_x(R) = d_y(R)$. The Hönl-London factors are summarised in Table 2.2.

The characteristics of all processes of interest are summarised in Table 2.3. The processes involving $1^3\Pi$ are Ω-distinguished while the three $c^3\Sigma^+ \to {}^3\Sigma^+$ are not. Because these $c^3\Sigma^+ \to {}^3\Sigma^+$ processes do not consider spin, they are treated within the spinless approximation (SLA), which entails $\Omega \approx \Lambda = 0$. The collision probability p_i for the $c^3\Sigma^+ \to {}^3\Sigma^+$ processes is then 1/3. For the Ω-distinguished transitions that start in the $1^3\Pi$ electronic state, it is equal to 2/9 and for the Ω-distinguished transitions $c^3\Sigma^+ \to 1^3\Pi$ $p_i = 1/9$.

From Table 2.3, the $1 \to$ a and c $\to$ a processes are expected to have the largest cross sections, and hence also the rate coefficients, due to the largest number of the target bound states and the biggest ΔE. The former reason causes the sum over J_i and J_f going to larger rotational quantum numbers. The latter reason causes the bigger ω_{if} of the emitted photon, which goes in the third power in Equation (1.100). The c $\to$ b process seems to be supported by a large FC overlap (the minima of the two electronic states are shifted only by 0.588 a_0) and also the transition dipole moment is nonzero for all internuclear distances (see Figure 1.8). On the other hand, the number of final bound states is quite small. The cross sections are still expected quite large. The $1 \to$ b process has a smaller transition dipole moment at the minimum of the initial electronic state. The number of target states stays the same. The minima, however, are more shifted (by 5.837 a_0). The expectation, thus, is that c $\to$ b should have larger cross sections and rate coefficients than $1 \to$ b. The rest of the processes should have smaller cross-section and rate-coefficient values than the above mentioned processes.

Table 2.3: Process characteristics are summarised for radiative association of He(2^3P) with Li^+(1^1S). Energies are in cm^{-1}. The values are taken from [30, 31].[a]

Process	$\Omega_i \to \Omega_f$	n_{tot}	n_r	n_w	n_n	$\mathcal{D}_{\Omega_f}$	n_v	n_{rv}	ΔE^b
1 → a	0 → 1	368	368	191	177	8 181.6	61	4 118	14 263.2
	1 → 0	367	367	190	177	8 182.2	61	4 176	14 263.2
	2 → 1	364	364	190	174	8 181.6	61	4 118	14 263.2
1 → b	0 → 1	368	338	164	174	829.5	33	1 256	9 230.9
	1 → 0	367	337	163	174	829.6	33	1 289	9 230.9
	2 → 1	364	334	163	171	829.5	33	1 256	9 230.9
1 → c	0 → 1	368	368	191	177	1 397.2	55	2 667	0
	1 → 0	367	367	190	177	1 397.4	55	2 722	0
	2 → 1	364	364	190	174	1 397.2	55	2 667	0
c → 1	0 → 1	454	99	60	39	1 743.5	19	885	0
	1 → 0	450	98	61	37	1 744.0	19	904	0
	1 → 2	450	98	61	37	1 743.1	19	868	0
1 → 1	0 → 0	368	272	134	138	1 744.0	19	904	0
	1 → 1	367	271	134	137	1 743.5	19	885	0
	2 → 2	364	268	135	134	1 743.1	19	868	0
c → a	0 → 0	458	416	193	223	8 183.0	61	4 172	14 263.0
c → b	0 → 0	458	133	76	57	829.5	33	1 289	9 231.0
c → c	0 → 0	458	301	140	161	1 399.5	54	2 727	0

[a] According to the definitions of [8]: n_{tot} is the total number of orbital resonances supported by the initial electronic state, from which n_r is the number of "symmetry-allowed" resonances, i.e., the number of resonances which have a bound partner in the corresponding target electronic state allowed by the dipole-moment selection rules, n_w is the number of wide resonances, and n_n is the number of narrow resonances; $\mathcal{D}_{\Omega_f}$ is the dissociation energy of the target electronic state from the ground ($v_f = 0, J_f = \Omega_f$) ro-vibrational state, n_v is the number of bound vibrational $\left(J_f^{min} = \Omega_f\right)$ states of the target electronic state, n_{rv} is the total number of bound ro-vibrational states of the target electronic state ($J_f^{min} = \Omega_f$), and ΔE is the energy difference between the dissociation levels of the potentials.

[b] ΔE was obtained for Ω-distinguished transitions by a weighted average for He(2^3P), which means that $E = 1/9 \sum_{J=0}^{2} J E_J$, where E_J are from [74].

Figure 2.4: Cross sections $\sigma^{1\to 0}(E_i)$ of the $1^3\Pi \to {}^3\Sigma^+$ processes for $HeLi^+$ are illustrated and only the $1 \to 0$ Ω-transitions are plotted [31]. The resonances with the width larger than 0.01 cm^{-1} are shown.

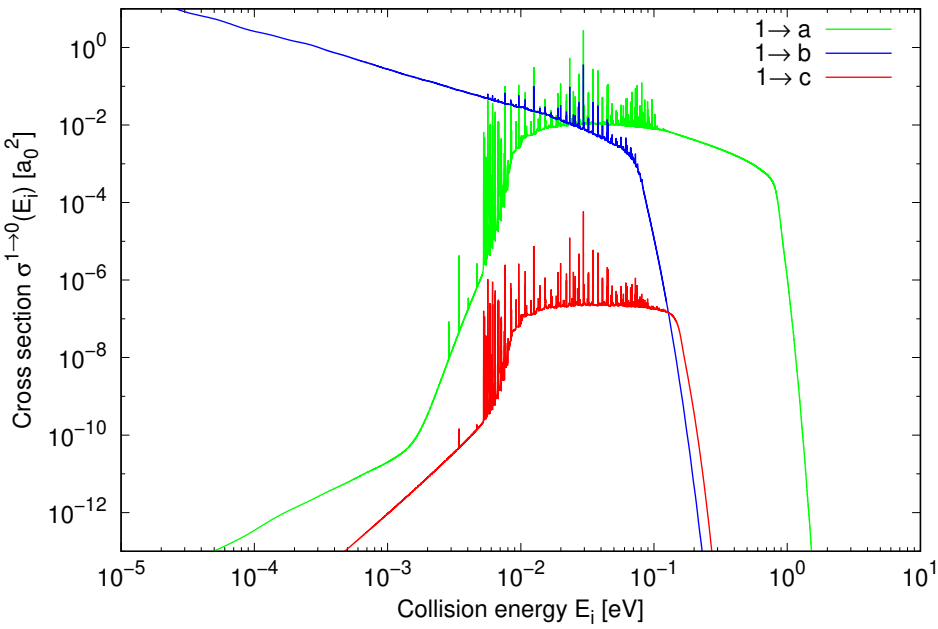

Cross Sections

The $1^3\Pi \to {}^3\Sigma^+$ cross sections for the $1 \to 0$ Ω-transition, $\sigma^{1\to 0}(E_i)$, are illustrated in Figure 2.4. The total cross sections are the sum over all Ω-transitions, but showing those would mean to lose the resonance structure. Here, the shape resonances of the $1^3\Pi$ continuum with $\Omega_i = 1$ are shown. The cross sections of the $0 \to 1$ and $2 \to 1$ Ω-transitions are very similar and, therefore, it is unnecessary to show them.

Surprisingly, the $1 \to$ a cross sections are not the largest up to $E \approx 0.024$ eV. These cross sections increase from very low values with increasing collision energy. On the other hand, the $1 \to$ b cross sections decrease from high values with increasing collision energy. In [31], several reasons are discussed. The first one is the influence of the barrier in $1^3\Pi$ that has its maximum $U_{\text{loc}}(R = 18.99\, a_0) = 64.9$ cm^{-1}. The $M_{E_i,1,1;v_f,0,0}$ elements at $E_i = 0.001$ eV and 0.075 eV for $1 \to$ a and $1 \to$ b were studied in Figure 2.5 (Fig. 5 in [31]). The first energy represents energies at which $1 \to$ b prevails. The second energy represents energies at which $1 \to$ a has slightly larger cross sections. In order to study the influence of the barrier, the integration in Equation (1.102) was divided into two terms: from 0 to 19 a_0 and from 19 a_0 to infinity.

At $E_i = 0.001$ eV, the $M_{E_i,1,1;v_f,0,0}$ elements are not strikingly different in the integration for $R \leq 19$ a_0 for both the processes. The difference is in the integration for $R \geq 19$ a_0. The elements of $1 \to$ b are around 5 orders of magnitude larger than those of $1 \to$ a. The difference is more striking when $M_{E_i,1,1;v_f,0,0}$ are squared in Equation (1.100). At $E_i = 0.075$ eV, the $M_{E_i,1,1;v_f,0,0}$ elements are significant for $R \geq 19$ a_0 and these are of the same magnitude for both the processes. Because these elements are summed in the cross-section

Figure 2.5: The contributions to $M_{E_i,1,1;v_f,0,0}$ $[ea_0/\sqrt{E_\mathrm{h}}]$ from 0 to 19 a_0 (red) and from 19 a_0 to infinity (blue) are illustrated for $1 \to$ a and $1 \to$ b at two collision energies, $E_i = 0.001$ eV and $E_i = 0.075$ eV, for HeLi$^+$ [31].

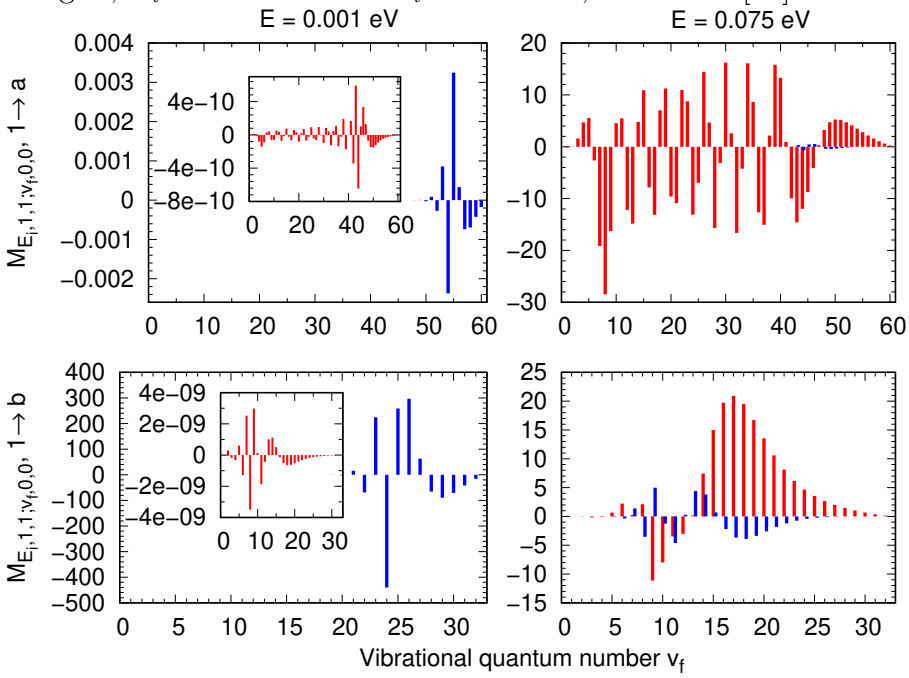

values, we get larger cross sections for $1 \to$ a.

Secondly, the differencies in transition dipole-moment functions of $1 \to$ b and other two $1^3\Pi \to {}^3\Sigma^+$ were studied. The $1 \to$ a and $1 \to$ c cross sections increase from low energy values. This is because of the barrier in the $1^3\Pi$ state. Then, one would expect the $1 \to$ b cross sections to increase from low energies, too. In Figure 1.8, it can be seen that both the transition dipole moments of $1 \to$ a and $1 \to$ c approach zero at $R \to \infty$, but $1 \to$ b approaches a nonzero value ($f_\infty \approx 2.538\ ea_0$). The cross sections for $1 \to$ b can be expressed by a sum of three contributions steming from the expression

$$d_x(R) = f_x(R) + f_\infty, \tag{2.15}$$

where

$$f_x(R \to \infty) = 0. \tag{2.16}$$

Then, from

$$\begin{aligned} \left|M_{E_i,J_i,1;v_f,J_f,0}\right|^2 =& |\langle\chi_{E_i,J_i,1}|\, f(R)\, |\psi_{v_f,J_f,0}\rangle|^2 + \\ &+ 2f_\infty \langle\chi_{E_i,J_i,1}|\, f(R)\, |\psi_{v_f,J_f,0}\rangle + \\ &+ f_\infty^2 |\langle\chi_{E_i,J_i,1}|\psi_{v_f,J_f,0}\rangle|^2 \end{aligned} \tag{2.17}$$

we get correspondingly

$$\sigma(E_i) = \sigma_f(E_i) + \sigma_{f_\infty f}(E_i) + \sigma_{f_\infty}(E_i). \tag{2.18}$$

Figure 2.6: Contributions $\sigma_f(E_i)$ (green), $|\sigma_{f_\infty f}(E_i)|$ (brown) and $\sigma_{f_\infty}(E_i)$ (red) to $1 \to$ b $\sigma^{1\to 0}(E_i)$ (blue) for HeLi$^+$ are illustrated [31].

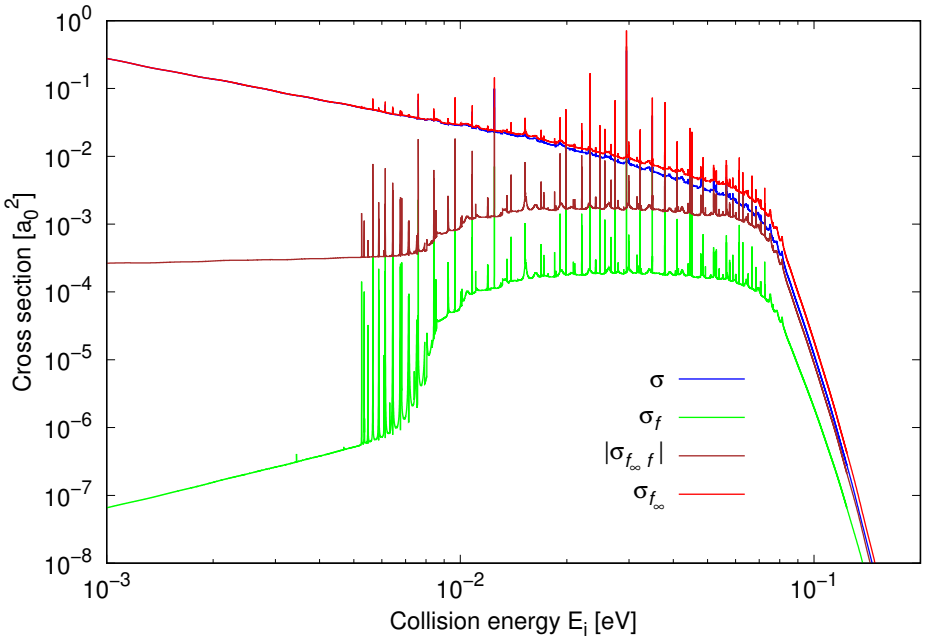

These three contributions are plotted in Figure 2.6 (Fig. 6 in [31]). The contribution $\sigma_{f_\infty f}(E_i)$ has negative values. In order to keep Figure 2.6 simple, only the absolute value $|\sigma_{f_\infty f}(E_i)|$ is plotted. The $\sigma_f(E_i)$ term represents values computed from $f_x(R)$. This term has a similar shape like the cross sections of $1 \to$ a and $1 \to$ c that also have their transition dipole moments approach zero. The $\sigma_{f_\infty}(R)$ term purely comes from the nonzero asymptote and is obviously responsible for the shape of the $1 \to$ b cross sections.

The cross section of $c^3\Sigma^+ \to 1^3\Pi$ is illustrated in Figure 2.7. Only the $0 \to 1$ Ω-transition is shown in order not to lose the resonance structure. This time, the shape resonances of $c^3\Sigma^+$ with $\Omega_i = 0$ are shown. At low collision energies, this process has the second largest cross sections. Their values are larger than the opposite channel $1 \to$ c except for the energies 0.01 eV$< E_i <$ 0.13 eV. At around 1.14 eV, the cross sections are the largest ones, prevailing slightly above the $1 \to$ a process. The sparse resonance structure stems from the fact that the maximum rotational number of $1^3\Pi$ bound states is $J_f = 70$, which forbids most of the resonances of $c^3\Sigma^+$. From Table 2.3, it can be seen that out of 454 resonances only 99 are symmetry-allowed. These resonances are low-energy lying, with the maximum energy of $E_{0,15,71} = 50.962\,303$ cm$^{-1} \approx 6.3 \times 10^{-3}$ eV.

Lastly, the cross sections of $1^3\Pi \to 1^3\Pi$ for the $1 \to 1$ Ω-transition are illustrated in Figure 2.8. Their values are expectedly small. Because of the barrier in PEC, the cross sections increase from low values with increasing collision energy. In contrast to the c $\to 1$ case, more resonances can be seen here. This is because $1^3\Pi$ has more resonances with lower rotational quantum numbers than 72. From Table 2.3, it can be seen that 99 resonances occur in the $0 \to 1$ Ω-distinguished transition for the c $\to 1$ process and 271 resonances in the $1 \to 1$ Ω-distinguished transition for the $1 \to 1$ process.

Figure 2.7: The cross sections of $c^3\Sigma^+ \rightarrow 1^3\Pi$ of $HeLi^+$ restricted to the $0 \rightarrow 1$ Ω-transition are illustrated. The resonances with the width larger than 0.01 cm^{-1} are shown.

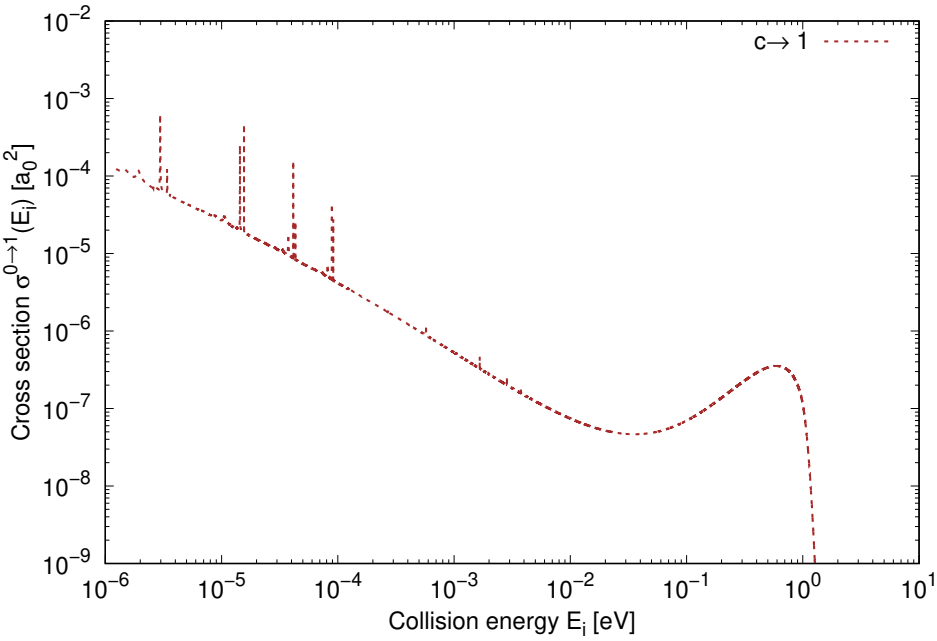

Figure 2.8: Cross sections of $1^3\Pi \rightarrow 1^3\Pi$ of $HeLi^+$ restricted to the $1 \rightarrow 1$ Ω-transition are illustrated. The resonances with the widths larger than 0.01 cm^{-1} are shown.

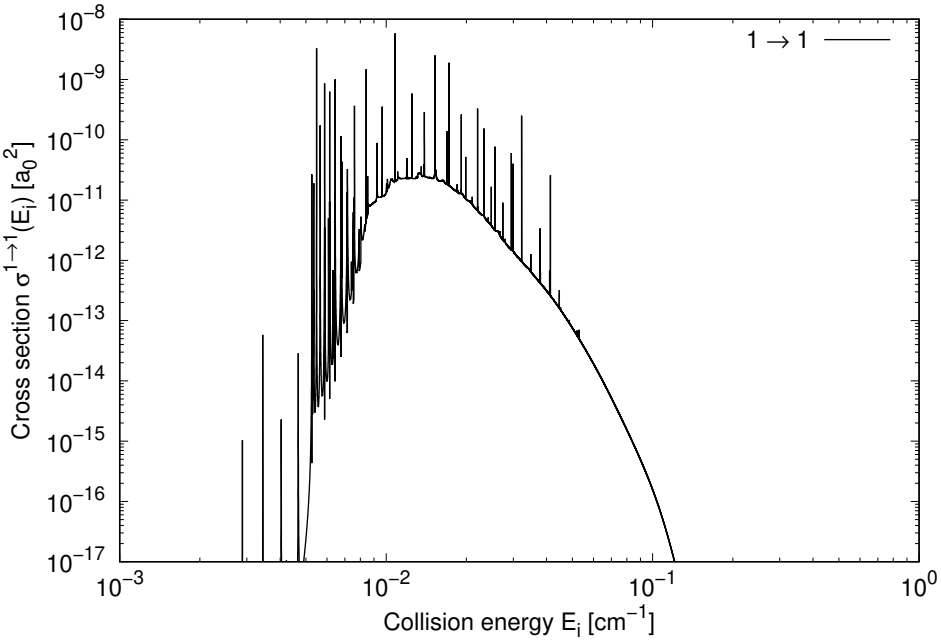

Figure 2.9: Rate coefficients of eight radiative association processes of $HeLi^+$ that represent the depopulation of the continuum in $He(2^3P)+Li^+(1^1S)$ are illustrated.

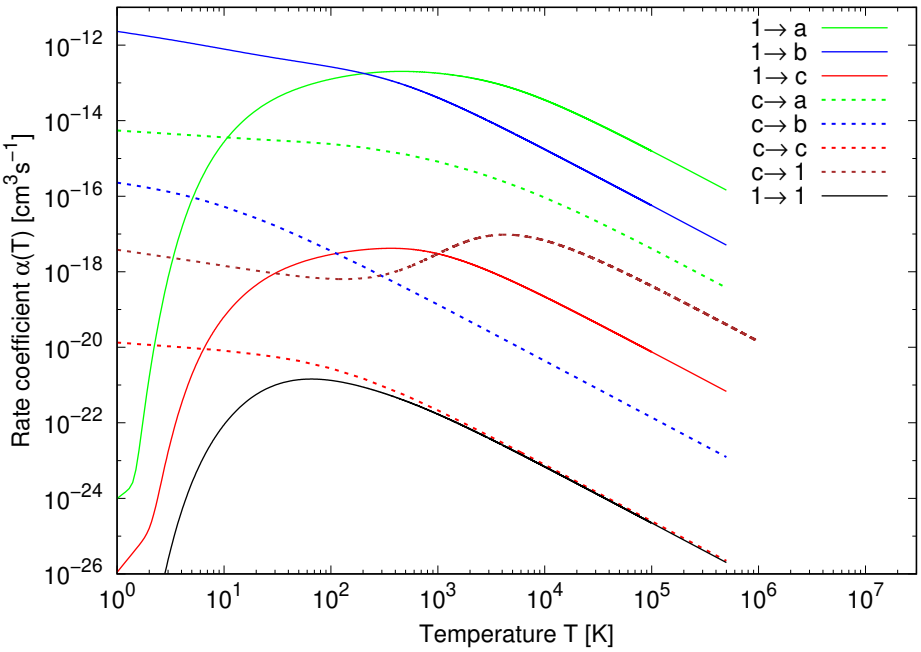

Rate Coefficients

The rate coefficients of all 8 electronic transitions are illustrated in Figure 2.9. Here, the $c^3\Sigma^+ \rightarrow {}^3\Sigma^+$ rate coefficients are shown, too. Up to slighly above 2 000 K, 1 → b prevails. Then, 1 → a is the most efficient RA channel. The second most efficient process up to around 10 K is c → a, then it becomes the third most important. Interestingly, c → b can be considered important only up to around 5 K, where is the third most efficient process. Between temperatures 100 K and 300 K, it is the fifth most efficient process and above 300 K it becomes the sixth most efficient one. At 100 K, 1 → c has larger rate coefficients than c → b and above 1 000 K, it is succeeded by the opposite process c → 1, where c → 1 becomes the fourth most important process. Above roughly 6 K, c → c becomes the second slowest process. The least efficient process is 1 → 1. Because of the barrier effect in the initial state, the 1 → a and 1 → c have lower values of rate coefficients at very low temperatures than the one-electronic-state process c → c.

The rate coefficients of $1^3\Pi \rightarrow {}^3\Sigma^+$ are summarised in Table 2.4. The rate coefficients for individual Ω-transitions ($\alpha^{0\rightarrow1}(T)$, $\alpha^{1\rightarrow0}(T)$, $\alpha^{2\rightarrow1}(T)$), their sum $\alpha(T)$ and $\alpha_{\mathrm{SLA}}(T)$ can be found also in the Table. Only the results of 1 → a were shown in so much detail in [31]. For the rest of electronic $1^3\Pi \rightarrow {}^3\Sigma^+$ transitions, only $\alpha(T)$ and $\alpha_{\mathrm{SLA}}(T)$ were shown in [31] because the values of individual Ω-distinguished rate coefficients are very similar if not the same. The spinless rate coefficients obtained from Equation (1.108) are a good approximation to the rate coefficients from a sum over Ω-distinguished contributions.

It was mentioned earlier that the $c^3\Sigma^+ \rightarrow {}^3\Sigma^+$ processes were calculated by SLA. Their rate coefficients are summarised in Table 2.5 taken from [30] (Table 2 there). All of them are $\alpha_{\mathrm{SLA}}(T)$ from Equation (1.108). Among them,

Table 2.4: Rate coefficients [$cm^3\,s^{-1}$] for the radiative association processes of the $HeLi^+$ molecular ion restricted to the $^3\Pi \rightarrow {}^3\Sigma^+$ symmetry are illustrated. For all processes, $\alpha^{0\rightarrow1}(T)$, $\alpha^{1\rightarrow0}(T)$, $\alpha^{2\rightarrow1}(T)$ rate coefficients and their sum $\alpha(T)$ are shown. The corresponding $\alpha_{\mathrm{SLA}}(T)$ are compared too. $\alpha(T)$ and $\alpha_{\mathrm{SLA}}(T)$ have similar values with slight differences up to arround 20 K. The Ω-distinguished rate coefficients resemble each other as well with slight differences up to around 50 K. The least different values are for the $1 \rightarrow$ b process.[a]

	$1 \rightarrow$ a					$1 \rightarrow$ b					$1 \rightarrow$ c				
T (K)	$\alpha^{0\rightarrow1}$	$\alpha^{1\rightarrow0}$	$\alpha^{2\rightarrow1}$	α	α_{SLA}	$\alpha^{0\rightarrow1}$	$\alpha^{1\rightarrow0}$	$\alpha^{2\rightarrow1}$	α	α_{SLA}	$\alpha^{0\rightarrow1}$	$\alpha^{1\rightarrow0}$	$\alpha^{2\rightarrow1}$	α	α_{SLA}
10	8.42(-16)	8.91(-16)	9.98(-16)	2.73(-15)	2.67(-15)	2.62(-13)	2.64(-13)	2.62(-13)	7.87(-13)	7.92(-13)	1.98(-20)	2.10(-20)	2.35(-20)	6.43(-20)	6.30(-20)
20	6.04(-15)	6.20(-15)	6.55(-15)	1.88(-14)	1.86(-14)	1.85(-13)	1.86(-13)	1.85(-13)	5.57(-13)	5.59(-13)	1.43(-19)	1.47(-19)	1.55(-19)	4.45(-19)	4.40(-19)
30	1.25(-14)	1.27(-14)	1.32(-14)	3.84(-14)	3.81(-14)	1.53(-13)	1.54(-13)	1.53(-13)	4.60(-13)	4.61(-13)	2.96(-19)	3.01(-19)	3.12(-19)	9.09(-19)	9.02(-19)
50	2.37(-14)	2.39(-14)	2.46(-14)	7.22(-14)	7.18(-14)	1.22(-13)	1.22(-13)	1.22(-13)	3.65(-13)	3.66(-13)	5.55(-19)	5.61(-19)	5.76(-19)	1.69(-18)	1.68(-18)
100	4.17(-14)	4.19(-14)	4.25(-14)	1.26(-13)	1.26(-13)	8.83(-14)	8.85(-14)	8.85(-14)	2.65(-13)	2.66(-13)	9.45(-19)	9.49(-19)	9.64(-19)	2.86(-18)	2.85(-18)
200	5.84(-14)	5.84(-14)	5.89(-14)	1.76(-13)	1.75(-13)	5.99(-14)	6.00(-14)	6.00(-14)	1.80(-13)	1.80(-13)	1.27(-18)	1.27(-18)	1.28(-18)	3.82(-18)	3.81(-18)
500	6.72(-14)	6.71(-14)	6.73(-14)	2.02(-13)	2.01(-13)	2.87(-14)	2.87(-14)	2.87(-14)	8.62(-14)	8.62(-14)	1.35(-18)	1.35(-18)	1.35(-18)	4.06(-18)	4.05(-18)
1 000	6.02(-14)	6.01(-14)	6.02(-14)	1.80(-13)	1.80(-13)	1.35(-14)	1.36(-14)	1.36(-14)	4.06(-14)	4.07(-14)	9.99(-19)	9.99(-19)	1.00(-18)	3.00(-18)	3.00(-18)
2 000	4.58(-14)	4.58(-14)	4.58(-14)	1.37(-13)	1.37(-13)	5.63(-15)	5.64(-15)	5.64(-15)	1.69(-14)	1.69(-14)	5.49(-19)	5.49(-19)	5.50(-19)	1.65(-18)	1.65(-18)
2 500	4.05(-14)	4.04(-14)	4.04(-14)	1.21(-13)	1.21(-13)	4.17(-15)	4.17(-15)	4.17(-15)	1.25(-14)	1.25(-14)	4.32(-19)	4.32(-19)	4.32(-19)	1.30(-18)	1.30(-18)
3 000	3.60(-14)	3.60(-14)	3.60(-14)	1.08(-13)	1.08(-13)	3.25(-15)	3.25(-15)	3.25(-15)	9.74(-15)	9.75(-15)	3.50(-19)	3.50(-19)	3.50(-19)	1.05(-18)	1.05(-18)
4 000	2.91(-14)	2.90(-14)	2.91(-14)	8.72(-14)	8.71(-14)	2.17(-15)	2.17(-15)	2.17(-15)	6.52(-15)	6.52(-15)	2.47(-19)	2.47(-19)	2.47(-19)	7.40(-19)	7.40(-19)
6 000	2.03(-14)	2.03(-14)	2.03(-14)	6.08(-14)	6.08(-14)	1.22(-15)	1.22(-15)	1.22(-15)	3.65(-15)	3.65(-15)	1.46(-19)	1.46(-19)	1.46(-19)	4.38(-19)	4.38(-19)
8 000	1.51(-14)	1.51(-14)	1.51(-14)	4.53(-14)	4.53(-14)	8.03(-16)	8.03(-16)	8.03(-16)	2.41(-15)	2.41(-15)	9.89(-20)	9.89(-20)	9.89(-20)	2.97(-19)	2.97(-19)
10 000	1.18(-14)	1.18(-14)	1.18(-14)	3.53(-14)	3.53(-14)	5.80(-16)	5.80(-16)	5.80(-16)	1.74(-15)	1.74(-15)	7.26(-20)	7.26(-20)	7.26(-20)	2.18(-19)	2.18(-19)
16 000	6.67(-15)	6.67(-15)	6.67(-15)	2.00(-14)	2.00(-14)	2.90(-16)	2.90(-16)	2.90(-16)	8.71(-16)	8.71(-16)	3.73(-20)	3.72(-20)	3.73(-20)	1.12(-19)	1.12(-19)
20 000	5.01(-15)	5.00(-15)	5.00(-15)	1.50(-14)	1.50(-14)	2.09(-16)	2.09(-16)	2.09(-16)	6.26(-16)	6.26(-16)	2.70(-20)	2.70(-20)	2.70(-20)	8.10(-20)	8.10(-20)
25 000	3.72(-15)	3.72(-15)	3.72(-15)	1.12(-14)	1.12(-14)	1.50(-16)	1.50(-16)	1.50(-16)	4.50(-16)	4.50(-16)	1.95(-20)	1.95(-20)	1.95(-20)	5.86(-20)	5.86(-20)
32 000	2.66(-15)	2.66(-15)	2.66(-15)	7.98(-15)	7.97(-15)	1.04(-16)	1.04(-16)	1.04(-16)	3.12(-16)	3.12(-16)	1.36(-20)	1.36(-20)	1.36(-20)	4.08(-20)	4.08(-20)
50 000	1.42(-15)	1.42(-15)	1.42(-15)	4.27(-15)	4.27(-15)	5.34(-17)	5.34(-17)	5.34(-17)	1.60(-16)	1.60(-16)	7.05(-21)	7.04(-21)	7.05(-21)	2.11(-20)	2.11(-20)
64 000	1.00(-15)	1.00(-15)	1.00(-15)	3.00(-15)	3.00(-15)	3.69(-17)	3.69(-17)	3.69(-17)	1.11(-16)	1.11(-16)	4.89(-21)	4.89(-21)	4.89(-21)	1.47(-20)	1.47(-20)
100 000	5.24(-16)	5.24(-16)	5.24(-16)	1.57(-15)	1.57(-15)	1.89(-17)	1.89(-17)	1.90(-17)	5.68(-17)	5.68(-17)	2.52(-21)	2.52(-21)	2.52(-21)	7.55(-21)	7.55(-21)
200 000	1.89(-16)	1.89(-16)	1.89(-16)	5.67(-16)	5.67(-16)	6.71(-18)	6.71(-18)	6.71(-18)	2.01(-17)	2.01(-17)	8.95(-22)	8.94(-22)	8.95(-22)	2.68(-21)	2.68(-21)
500 000	4.84(-17)	4.84(-17)	4.84(-16)	1.45(-16)	1.45(-16)	1.70(-18)	1.70(-18)	1.70(-18)	5.10(-18)	5.10(-18)	2.27(-22)	2.27(-22)	2.27(-22)	6.81(-22)	6.81(-22)

[a] $x(-y) \equiv x \times 10^{-y}$

Table 2.5: Spinless rate coefficients [$cm^3\,s^{-1}$] for the radiative association processes of the $HeLi^+$ molecular ion restricted to $^3\Sigma^+$ symmetry are summarised. This Table was published in [30].[a]

T (K)	c → a	c → b	c → c
10	3.63(-15)	5.27(-17)	8.13(-21)
20	3.22(-15)	2.62(-17)	6.52(-21)
30	3.01(-15)	1.66(-17)	5.57(-21)
50	2.77(-15)	8.86(-18)	4.36(-21)
100	2.41(-15)	3.58(-18)	2.77(-21)
200	1.96(-15)	1.38(-18)	1.49(-21)
500	1.28(-15)	3.72(-19)	5.30(-22)
1 000	8.29(-16)	1.35(-19)	2.14(-22)
2 000	4.83(-16)	4.83(-20)	8.14(-23)
2 500	3.97(-16)	3.47(-20)	5.91(-23)
3 000	3.35(-16)	2.64(-20)	4.54(-23)
4 000	2.53(-16)	1.72(-20)	2.99(-23)
6 000	1.65(-16)	9.39(-21)	1.65(-23)
8 000	1.19(-16)	6.10(-21)	1.08(-23)
10 000	9.17(-17)	4.37(-21)	7.73(-24)
16 000	5.13(-17)	2.16(-21)	3.84(-24)
20 000	3.85(-17)	1.55(-21)	2.75(-24)
25 000	2.86(-17)	1.11(-21)	1.97(-24)
32 000	2.05(-17)	7.65(-22)	1.36(-24)
50 000	1.10(-17)	3.92(-22)	7.00(-25)
64 000	7.75(-18)	2.71(-22)	4.84(-25)
100 000	4.07(-18)	1.39(-22)	2.48(-25)
200 000	1.47(-18)	4.90(-23)	8.77(-26)
500 000	3.78(-19)	1.24(-23)	2.22(-26)

[a] $x(-y) \equiv x \times 10^{-y}$.

$c^3\Sigma^+ \rightarrow a^3\Sigma^+$ has the largest rate coefficients.

Table 2.6 summarises the rate coefficients of c → 1 with the Ω-transition rate coefficients and also the spinless rate coefficients. The rate coefficients for individual Ω-transitions are similar again. The spinless rate coefficients are similar to the sum over the $\Omega_i \rightarrow \Omega_f$ transitions.

Lastly, the rate coefficients of 1 → 1 are shown in Table 2.7. The Ω-transition rate coefficients are summarised, too. This time their values slightly differ; therefore, the spinless rate coefficients seem to be different from the rate coefficients obtained as a sum over the Ω-transition rate coefficients. However, the values are so small that the difference is insignificant. Hence the spinless rate coefficient is still a good approximation to the rate coefficient.

Because the spinless rate coefficients are reliable, we summarise all of them in Table 2.8.

The total rate coefficients of creating a bound $HeLi^+$ in the $He(2^3P)+Li^+(1^1S)$ continuum, $\alpha_{dep}(T)$, are summarised in Table 2.9, together with the depopulation rate coefficients for each symmetry of approach separately, $1^3\Pi$ and $c^3\Sigma^+$. The former one is a sum over rate coefficients of 1 → a, 1 → b, 1 → c and 1 → 1. The latter is a sum over rate coefficients of c → a, c → b, c → c and c → 1.

Table 2.6: Rate coefficients [$cm^3\,s^{-1}$] for the c $\rightarrow$ 1 radiative association process of the $HeLi^+$ molecular ion computed from the Ω-distinguished rate coefficients are summarised. The rate coefficients are compared to the spinless rate coefficients. Similarly, as it was for the 1 $\rightarrow$ b process in Table 2.4, the Ω-distinguished rate coefficients have similar values. The same can be said about the rate coefficients $\alpha(T)$ and spin-less rate coefficients $\alpha_{\mathrm{SLA}}(T)$. Both the 1 $\rightarrow$ b and c $\rightarrow$ 1 rate coefficients have decreasing values from low temperatures with c $\rightarrow$ 1 only up to around 100 K.[a]

T (K)	$\alpha^{0\rightarrow1}$	$\alpha^{1\rightarrow0}$	$\alpha^{1\rightarrow2}$	α	α_{SLA}
10	4.77(-19)	4.79(-19)	4.79(-19)	1.44(-18)	1.43(-18)
20	3.56(-19)	3.57(-19)	3.57(-19)	1.07(-18)	1.07(-18)
30	3.03(-19)	3.03(-19)	3.03(-19)	9.10(-19)	9.09(-19)
50	2.53(-19)	2.54(-19)	2.54(-19)	7.61(-19)	7.60(-19)
100	2.16(-19)	2.16(-19)	2.16(-19)	6.49(-19)	6.49(-19)
200	2.25(-19)	2.25(-19)	2.25(-19)	6.75(-19)	6.75(-19)
500	4.15(-19)	4.15(-19)	4.15(-19)	1.25(-18)	1.25(-18)
1 000	9.98(-19)	9.98(-19)	9.98(-19)	2.99(-18)	2.99(-18)
2 000	2.27(-18)	2.27(-18)	2.27(-18)	6.81(-18)	6.81(-18)
2 500	2.70(-18)	2.70(-18)	2.70(-18)	8.10(-18)	8.10(-18)
3 000	2.98(-18)	2.98(-18)	2.98(-18)	8.93(-18)	8.93(-18)
4 000	3.19(-18)	3.20(-18)	3.20(-18)	9.59(-18)	9.58(-18)
6 000	3.00(-18)	3.01(-18)	3.01(-18)	9.02(-18)	9.01(-18)
8 000	2.61(-18)	2.61(-18)	2.61(-18)	7.83(-18)	7.83(-18)
10 000	2.24(-18)	2.24(-18)	2.24(-18)	6.71(-18)	6.71(-18)
16 000	1.46(-18)	1.46(-18)	1.46(-18)	4.38(-18)	4.37(-18)
20 000	1.15(-18)	1.15(-18)	1.15(-18)	3.44(-18)	3.44(-18)
25 000	8.85(-19)	8.86(-19)	8.87(-19)	2.66(-18)	2.66(-18)
32 000	6.54(-19)	6.54(-19)	6.55(-19)	1.96(-18)	1.96(-18)
50 000	3.65(-19)	3.66(-19)	3.66(-19)	1.10(-18)	1.10(-18)
64 000	2.61(-19)	2.61(-19)	2.62(-19)	7.84(-19)	7.83(-19)
100 000	1.40(-19)	1.40(-19)	1.40(-19)	4.19(-19)	4.19(-19)
200 000	5.14(-20)	5.14(-20)	5.15(-20)	1.54(-19)	1.54(-19)
500 000	1.33(-20)	1.33(-20)	1.33(-20)	4.00(-20)	3.99(-20)

[a] $x(-y) \equiv x \times 10^{-y}$

Table 2.7: Rate coefficients [$cm^3\,s^{-1}$] for the $1 \rightarrow 1$ radiative association process of the $HeLi^+$ molecular ion computed from the Ω-distinguished rate coefficients are illustrated. The rate coefficients are compared to the spinless rate coefficients. The values might seem different, however, all of them are smaller than 1.4×10^{-21}.[a]

T (K)	$\alpha^{0\rightarrow0}$	$\alpha^{1\rightarrow1}$	$\alpha^{2\rightarrow2}$	α	α_{SLA}
10	2.99(-23)	2.81(-23)	3.07(-23)	8.87(-23)	8.43(-23)
20	2.05(-22)	1.76(-22)	1.81(-22)	5.62(-22)	5.27(-22)
30	3.62(-22)	3.12(-22)	3.18(-22)	9.92(-22)	9.37(-22)
50	4.97(-22)	4.40(-22)	4.47(-22)	1.38(-21)	1.32(-21)
100	4.66(-22)	4.27(-22)	4.34(-22)	1.33(-21)	1.28(-21)
200	3.03(-22)	2.89(-22)	2.92(-22)	8.84(-22)	8.68(-22)
500	1.25(-22)	1.27(-22)	1.27(-22)	3.79(-22)	3.82(-22)
1 000	5.50(-23)	5.77(-23)	5.68(-23)	1.69(-22)	1.73(-22)
2 000	2.20(-23)	2.34(-23)	2.30(-23)	6.84(-23)	7.03(-23)
2 500	1.61(-23)	1.73(-23)	1.69(-23)	5.03(-23)	5.18(-23)
3 000	1.25(-23)	1.34(-23)	1.31(-23)	3.90(-23)	4.02(-23)
4 000	8.29(-24)	8.93(-24)	8.73(-24)	2.60(-23)	2.68(-23)
6 000	4.62(-24)	4.99(-24)	4.87(-24)	1.45(-23)	1.50(-23)
8 000	3.03(-24)	3.28(-24)	3.20(-24)	9.52(-24)	9.85(-24)
10 000	2.19(-24)	2.37(-24)	2.31(-24)	6.86(-24)	7.10(-24)
16 000	1.09(-24)	1.18(-24)	1.15(-24)	3.43(-24)	3.55(-24)
20 000	7.83(-25)	8.50(-25)	8.29(-25)	2.46(-24)	2.55(-24)
25 000	5.62(-25)	6.10(-25)	5.95(-25)	1.77(-24)	1.83(-24)
32 000	3.89(-25)	4.23(-25)	4.12(-25)	1.22(-24)	1.27(-24)
50 000	2.00(-25)	2.17(-25)	2.12(-25)	6.29(-25)	6.51(-25)
64 000	1.38(-25)	1.50(-25)	1.46(-25)	4.35(-25)	4.50(-25)
100 000	7.09(-26)	7.70(-26)	7.51(-26)	2.23(-25)	2.31(-25)
200 000	2.51(-26)	2.73(-26)	2.66(-26)	7.89(-26)	8.18(-26)
500 000	6.35(-27)	6.91(-27)	6.73(-27)	2.00(-26)	2.07(-26)

[a] $x(-y) \equiv x \times 10^{-y}$

Table 2.8: Spinless rate coefficients [cm^3s^{-1}] of all studied processes on the $HeLi^+$ molecular ion are summarised. The results of $1^3\Pi \rightarrow {}^3\Sigma^+$ and ${}^3\Sigma^+ \rightarrow {}^3\Sigma^+$ are taken from [30, 31].[a]

T(K)	$1 \rightarrow$ a	$1 \rightarrow$ b	$1 \rightarrow$ c	$1 \rightarrow 1$	c $\rightarrow$ a	c $\rightarrow$ b	c $\rightarrow$ c	c $\rightarrow 1$
10	2.67(-15)	7.92(-13)	6.30(-20)	8.43(-23)	3.63(-15)	5.27(-17)	8.13(-21)	1.43(-18)
20	1.86(-14)	5.59(-13)	4.40(-19)	5.27(-22)	3.22(-15)	2.62(-17)	6.52(-21)	1.07(-18)
30	3.81(-14)	4.61(-13)	9.02(-19)	9.37(-22)	3.01(-15)	1.66(-17)	5.57(-21)	9.09(-19)
50	7.18(-14)	3.66(-13)	1.68(-18)	1.32(-21)	2.77(-15)	8.86(-18)	4.36(-21)	7.60(-19)
100	1.26(-13)	2.66(-13)	2.85(-18)	1.28(-21)	2.41(-15)	3.58(-18)	2.77(-21)	6.49(-19)
200	1.75(-13)	1.80(-13)	3.81(-18)	8.68(-22)	1.96(-15)	1.38(-18)	1.49(-21)	6.75(-19)
500	2.01(-13)	8.62(-14)	4.05(-18)	3.82(-22)	1.28(-15)	3.72(-19)	5.30(-22)	1.25(-18)
1 000	1.80(-13)	4.07(-14)	3.00(-18)	1.73(-22)	8.29(-16)	1.35(-19)	2.14(-22)	2.99(-18)
2 000	1.37(-13)	1.69(-14)	1.65(-18)	7.03(-23)	4.83(-16)	4.83(-20)	8.14(-23)	6.81(-18)
2 500	1.21(-13)	1.25(-14)	1.30(-18)	5.18(-23)	3.97(-16)	3.47(-20)	5.91(-23)	8.10(-18)
3 000	1.08(-13)	9.75(-15)	1.05(-18)	4.02(-23)	3.35(-16)	2.64(-20)	4.54(-23)	8.93(-18)
4 000	8.71(-14)	6.52(-15)	7.40(-19)	2.68(-23)	2.53(-16)	1.72(-20)	2.99(-23)	9.58(-18)
6 000	6.08(-14)	3.65(-15)	4.38(-19)	1.50(-23)	1.65(-16)	9.39(-21)	1.65(-23)	9.01(-18)
8 000	4.53(-14)	2.41(-15)	2.97(-19)	9.85(-24)	1.19(-16)	6.10(-21)	1.08(-23)	7.83(-18)
10 000	3.53(-14)	1.74(-15)	2.18(-19)	7.10(-24)	9.17(-17)	4.37(-21)	7.73(-24)	6.71(-18)
16 000	2.00(-14)	8.71(-16)	1.12(-19)	3.55(-24)	5.13(-17)	2.16(-21)	3.84(-24)	4.37(-18)
20 000	1.50(-14)	6.26(-16)	8.10(-20)	2.55(-24)	3.85(-17)	1.55(-21)	2.75(-24)	3.44(-18)
25 000	1.12(-14)	4.50(-16)	5.86(-20)	1.83(-24)	2.86(-17)	1.11(-21)	1.97(-24)	2.66(-18)
32 000	7.97(-15)	3.12(-16)	4.08(-20)	1.27(-24)	2.05(-17)	7.65(-22)	1.36(-24)	1.96(-18)
50 000	4.27(-15)	1.60(-16)	2.11(-20)	6.51(-25)	1.10(-17)	3.92(-22)	7.00(-25)	1.10(-18)
64 000	3.00(-15)	1.11(-16)	1.47(-20)	4.50(-25)	7.75(-18)	2.71(-22)	4.84(-25)	7.83(-19)
100 000	1.57(-15)	5.68(-17)	7.55(-21)	2.31(-25)	4.07(-18)	1.39(-22)	2.48(-25)	4.19(-19)
200 000	5.67(-16)	2.01(-17)	2.68(-21)	8.18(-26)	1.47(-18)	4.90(-23)	8.77(-26)	1.54(-19)
500 000	1.45(-16)	5.10(-18)	6.81(-22)	2.07(-26)	3.78(-19)	1.24(-23)	2.22(-26)	3.99(-20)

[a] $x(-y) \equiv x \times 10^{-y}$

Figure 2.10: Depopulation rate coefficients of the $1^3\Pi$ and $c^3\Sigma^+$ continua of $HeLi^+$ are illustrated.

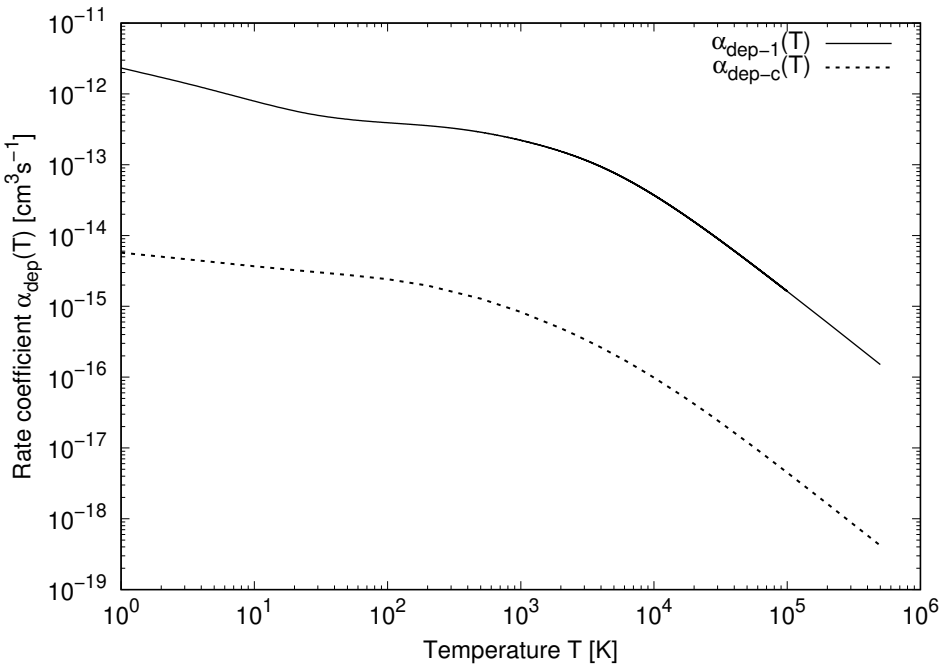

All the individual summands are also shown in Table 2.9. The depopulation of the $1^3\Pi$ continuum is around 2 or 3 orders more efficient than the depopulation from the $c^3\Sigma^+$ continuum. The sum of $\alpha_{\mathrm{dep-1}}(T)$ and $\alpha_{\mathrm{dep-c}}(T)$ gives $\alpha_{\mathrm{dep}}(T)$. From Table 2.9, it can be said that $\alpha_{\mathrm{dep}}(T) \approx \alpha_{\mathrm{dep-1}}(T)$. The depopulation rate coefficients for each symmetry are illustrated in Figure 2.10 and are denoted as $\alpha_{\mathrm{dep-1}}(T)$ and $\alpha_{\mathrm{dep-c}}(T)$.

The resonance contribution is typically small in comparison with the background contribution. This is true mainly for the narrow resonances and for continua with perhaps wide but scarce resonances. In the $1 \rightarrow$ a process, around 190 wide resonances can participate in the transition. If we look at their contribution $\alpha_{\mathrm{w}}(T)$, illustrated in the top panel of Figure 2.11, we can see it is larger than $\alpha_{\mathrm{bg}}(T)$ at low temperatures up to 200 K. In $1 \rightarrow$ b, however, the background contribution basically determines the value of the rate coefficient. This is depicted in the middle panel. The number of allowed wide shape resonances is 164 for the $0 \rightarrow 1$ transition and 163 for $1 \rightarrow 0$ and $2 \rightarrow 1$ transitions. Lastly, we show the individual contributions for a process with the least allowed shape resonances which is c $\rightarrow$ 1, in the bottom panel. Only 60 wide resonances for the $0 \rightarrow 1$ transition and 61 wide resonances for the $1 \rightarrow 0$ and $1 \rightarrow 2$ transitions contribute to the rate coefficient in this transition. It is not straightforward to compare $\alpha_{\mathrm{w}}(T)$ among these three RA transitions since each has a different number of the target bound states, $d_x(R)$ and ΔE, all of which enlarge the contribution. Then, the tunnelling widths also play a role since the resonance neighbourhood δ_{r_i} that is skipped in $\alpha_{\mathrm{bg}}(T)$ and added in the integration in $\alpha_{\mathrm{w}}(T)$ is equal to $E_{v_i,J_i,\Omega_i} - 5\Gamma^{\mathrm{tun}}_{v_i,J_i,\Omega_i}, E_{v_i,J_i,\Omega_i} + 5\Gamma^{\mathrm{tun}}_{v_i,J_i,\Omega_i}$, where E_{v_i,J_i,Ω_i} is the energy of the shape resonance with v_i, J_i, Ω_i. The narrow resonances contribute expectedly the least in all three cases.

Table 2.9: Depopulation rate coefficients [cm^3s^{-1}] for the continua of the $1^3\Pi$ and $c^3\Sigma^+$ states of the $HeLi^+$ molecular ion and of the continuum of the dissociation limit $He(2^3P)+Li^+(1^1S)$; $\alpha_{dep-1}(T)$ is computed from $\alpha(T)$ of $1 \to a$, $1 \to b$, $1 \to c$ and $1 \to 1$; α_{dep-c} is computed from the spinless $c \to a$, $c \to b$ and $c \to c$ rate coefficients and from $\alpha(T)$ of $c \to 1$. $\alpha_{dep}(T)$ is a sum of $\alpha_{dep-1}(T)$ and α_{dep-c}. The results of $1^3\Pi \to {}^3\Sigma^+$ and ${}^3\Sigma^+ \to {}^3\Sigma^+$ are taken from [30, 31].[a]

T(K)	$1 \to a$	$1 \to b$	$1 \to c$	$1 \to 1$	α_{dep-1}	$c \to a$	$c \to b$	$c \to c$	$c \to 1$	α_{dep-c}	α_{dep}
10	2.73(-15)	7.87(-13)	6.43(-20)	8.87(-23)	7.90(-13)	3.63(-15)	5.27(-17)	8.13(-21)	1.44(-18)	3.68(-15)	7.94(-13)
20	1.88(-14)	5.57(-13)	4.45(-19)	5.62(-22)	5.76(-13)	3.22(-15)	2.62(-17)	6.52(-21)	1.07(-18)	3.25(-15)	5.79(-13)
30	3.84(-14)	4.60(-13)	9.09(-19)	9.92(-22)	4.98(-13)	3.01(-15)	1.66(-17)	5.57(-21)	9.10(-19)	3.03(-15)	5.01(-13)
50	7.22(-14)	3.65(-13)	1.69(-18)	1.38(-21)	4.38(-13)	2.77(-15)	8.86(-18)	4.36(-21)	7.61(-19)	2.78(-15)	4.40(-13)
100	1.26(-13)	2.65(-13)	2.86(-18)	1.33(-21)	3.91(-13)	2.41(-15)	3.58(-18)	2.77(-21)	6.49(-19)	2.41(-15)	3.94(-13)
200	1.76(-13)	1.80(-13)	3.82(-18)	8.84(-22)	3.56(-13)	1.96(-15)	1.38(-18)	1.49(-21)	6.75(-19)	1.96(-15)	3.58(-13)
500	2.02(-13)	8.62(-14)	4.06(-18)	3.79(-22)	2.88(-13)	1.28(-15)	3.72(-19)	5.30(-22)	1.25(-18)	1.28(-15)	2.89(-13)
1 000	1.80(-13)	4.06(-14)	3.00(-18)	1.69(-22)	2.21(-13)	8.29(-16)	1.35(-19)	2.14(-22)	2.99(-18)	8.32(-16)	2.22(-13)
2 000	1.37(-13)	1.69(-14)	1.65(-18)	6.84(-23)	1.54(-13)	4.83(-16)	4.83(-20)	8.14(-23)	6.81(-18)	4.90(-16)	1.55(-13)
2 500	1.21(-13)	1.25(-14)	1.30(-18)	5.03(-23)	1.34(-13)	3.97(-16)	3.47(-20)	5.91(-23)	8.10(-18)	4.05(-16)	1.34(-13)
3 000	1.08(-13)	9.74(-15)	1.05(-18)	3.90(-23)	1.18(-13)	3.35(-16)	2.64(-20)	4.54(-23)	8.93(-18)	3.44(-16)	1.18(-13)
4 000	8.72(-14)	6.52(-15)	7.40(-19)	2.60(-23)	9.37(-14)	2.53(-16)	1.72(-20)	2.99(-23)	9.59(-18)	2.63(-16)	9.40(-14)
6 000	6.08(-14)	3.65(-15)	4.38(-19)	1.45(-23)	6.45(-14)	1.65(-16)	9.39(-21)	1.65(-23)	9.02(-18)	1.74(-16)	6.46(-14)
8 000	4.53(-14)	2.41(-15)	2.97(-19)	9.52(-24)	4.77(-14)	1.19(-16)	6.10(-21)	1.08(-23)	7.83(-18)	1.27(-16)	4.78(-14)
10 000	3.53(-14)	1.74(-15)	2.18(-19)	6.86(-24)	3.71(-14)	9.17(-17)	4.37(-21)	7.73(-24)	6.71(-18)	9.84(-17)	3.72(-14)
16 000	2.00(-14)	8.71(-16)	1.12(-19)	3.43(-24)	2.09(-14)	5.13(-17)	2.16(-21)	3.84(-24)	4.38(-18)	5.57(-17)	2.09(-14)
20 000	1.50(-14)	6.26(-16)	8.10(-20)	2.46(-24)	1.56(-14)	3.85(-17)	1.55(-21)	2.75(-24)	3.44(-18)	4.19(-17)	1.57(-14)
25 000	1.12(-14)	4.50(-16)	5.86(-20)	1.77(-24)	1.16(-14)	2.86(-17)	1.11(-21)	1.97(-24)	2.66(-18)	3.13(-17)	1.16(-14)
32 000	7.98(-15)	3.12(-16)	4.08(-20)	1.22(-24)	8.29(-15)	2.05(-17)	7.65(-22)	1.36(-24)	1.96(-18)	2.25(-17)	8.31(-15)
50 000	4.27(-15)	1.60(-16)	2.11(-20)	6.29(-25)	4.43(-15)	1.10(-17)	3.92(-22)	7.00(-25)	1.10(-18)	1.21(-17)	4.44(-15)
64 000	3.00(-15)	1.11(-16)	1.47(-20)	4.35(-25)	3.11(-15)	7.75(-18)	2.71(-22)	4.84(-25)	7.84(-19)	8.53(-18)	3.12(-15)
100 000	1.57(-15)	5.68(-17)	7.55(-21)	2.23(-25)	1.63(-15)	4.07(-18)	1.39(-22)	2.48(-25)	4.19(-19)	4.49(-18)	1.63(-15)
200 000	5.67(-16)	2.01(-17)	2.68(-21)	7.89(-26)	5.87(-16)	1.47(-18)	4.90(-23)	8.77(-26)	1.54(-19)	1.62(-18)	5.89(-16)
500 000	1.45(-16)	5.10(-18)	6.81(-22)	2.00(-26)	1.50(-16)	3.78(-19)	1.24(-23)	2.22(-26)	4.00(-20)	4.18(-19)	1.51(-16)

[a] $x(-y) \equiv x \times 10^{-y}$

Figure 2.11: Contributions to the rate coefficients are illustrated for 1 → a, 1 → b and c → 1 transitions on the $HeLi^+$ molecular ion.

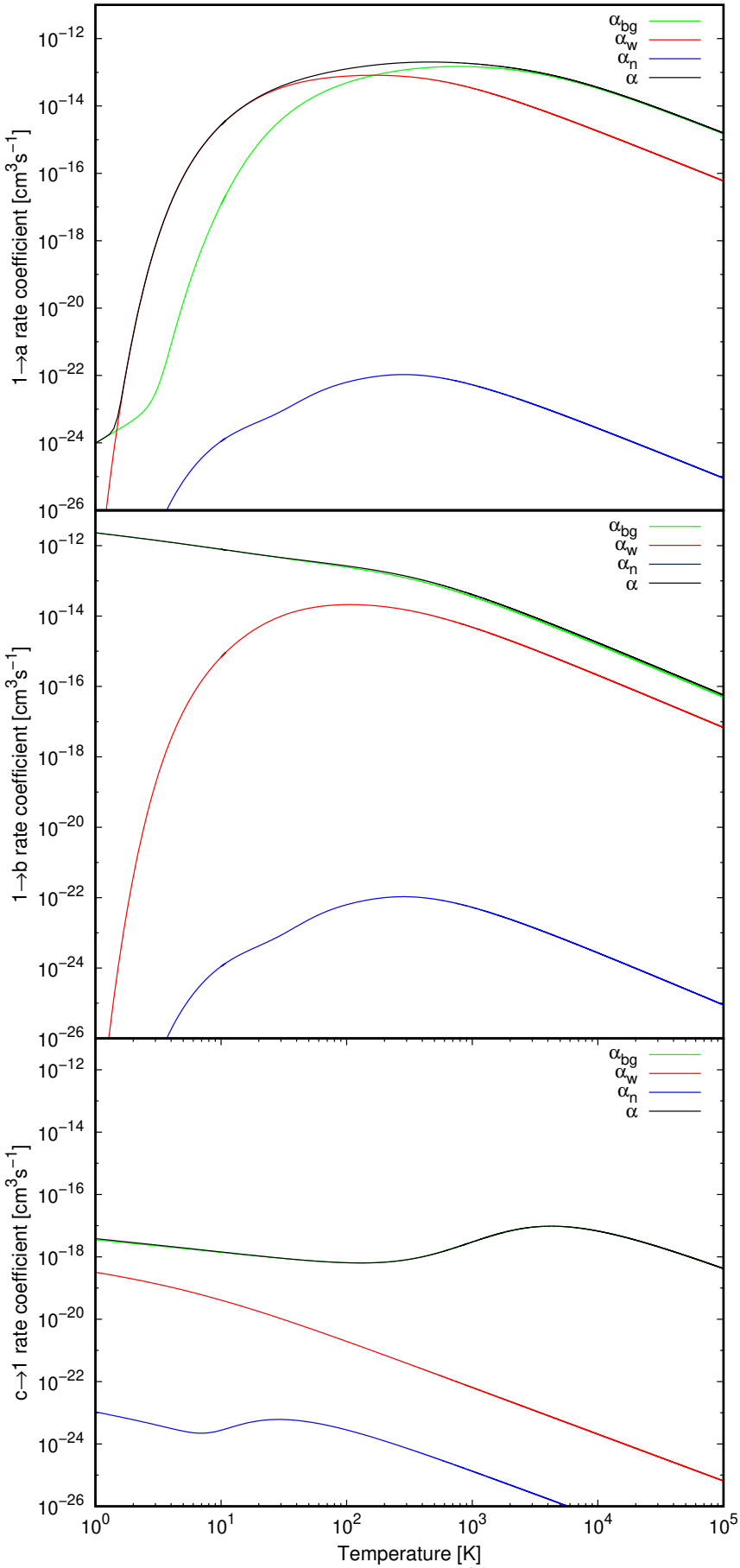

Figure 2.12: Cross sections for spontaneous and stimulated emission in $1^3\Pi \rightarrow c^3\Sigma^+$ radiative association process for $HeLi^+$ at several background temperatures: 500 K, 1 000 K, 2 000 K, 5 000 K and 10 000 K. They are compared with the cross section for the spontaneous emission $T_b = 0$ K. The shape resonances of $1^3\Pi$ with the radiative width larger than 0.1 cm^{-1} are depicted.

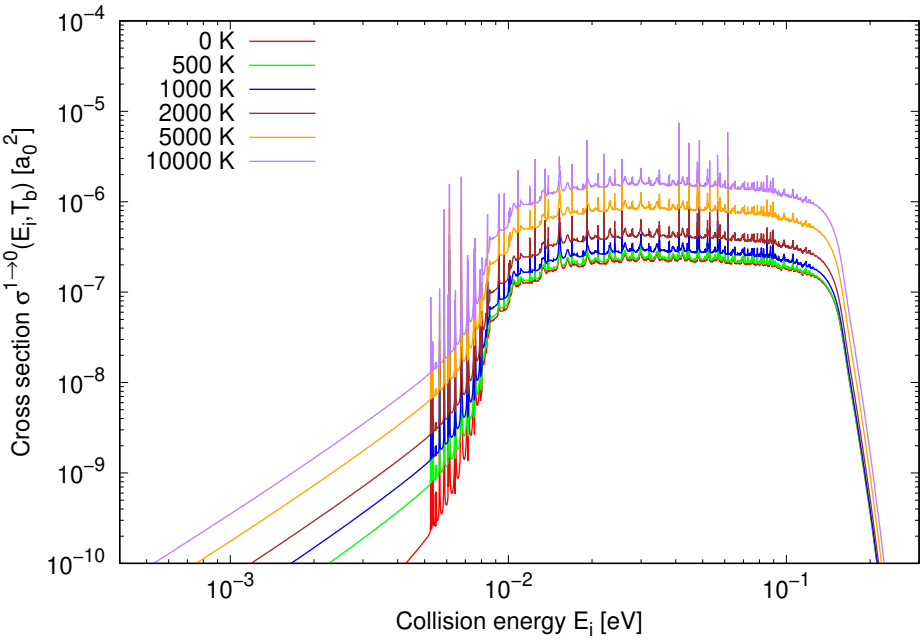

Stimulated and Spontaneous Emission

The cross sections of the $1^3\Pi \rightarrow c^3\Sigma^+$ process with $T_b \neq 0$ are illustrated in Figure 2.12. The shape resonances stem from the $1^3\Pi$ continua and only those are depicted which radiative widths are larger than 0.1 cm^{-1}. At low energies, the enhancement from the factor

$$\frac{1}{1 - e^{-\frac{E_i + \Delta E - E_f}{k_B T_b}}} \tag{2.19}$$

is the largest, which was also seen, e.g., in [51], [75]. Around 0.009 eV, the cross sections $\sigma(E_i, T)$ approach each other. At 0.01 eV, however, the cross sections are more apart from each other again. Their values approach each other again at collision energies above 0.1 eV.

The corresponding rate coefficients are illustrated in Figure 2.13. The nonzero background temperature enlarges the stimulated and spontaneous rate coefficients $\alpha(T, T_b)$ with increasing T_b through factor (2.19) in the energy integration. Typically, this enlargement for the stimulated emission is insignificant for two-electronic-state transitions up to a certain background temperature because factor (2.19) approaches 1, when $\Delta E \gg 0$. These $1^3\Pi$ and $c^3\Sigma^+$ states, however, have the same dissociation limit, hence $\Delta E = 0$.

In Figure 2.13, $\alpha(T = 1\,K, T_b = 500\,K)$ differs from $\alpha(T = 1\,K, T_b = 0\,K)$ more than $\alpha(T = 1\,K, T_b = 1\,000\,K)$ differs from $\alpha(T = 1\,K, T_b = 500\,K)$ although the difference in the background temperature is the same. Typically, the difference between $\alpha(T, T_b = 0\,K)$ and $\alpha(T, T_b = 500\,K)$ is the largest at low T. The above

Figure 2.13: Rate coefficients of stimulated emission in the $1^3\Pi \rightarrow c^3\Sigma^+$ radiative association in $HeLi^+$. This Figure was published in [31].

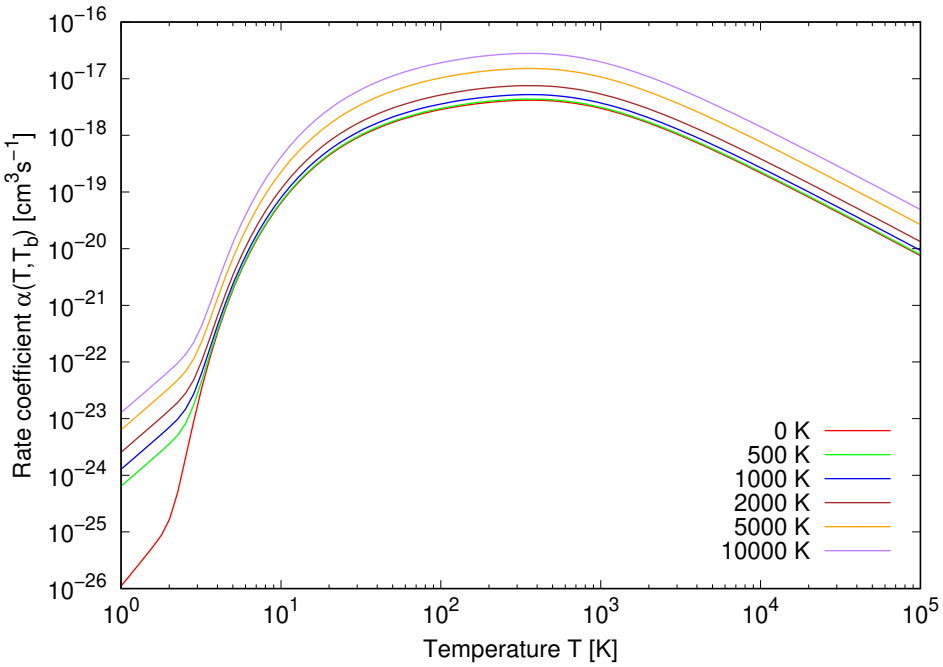

mentioned common features for $\alpha(T, T_b)$ were observed for instance in [30], [75], [16]. However, the largest difference between $\alpha(T, T_b)$ of different T_b can be observed at larger T, too, like it was in [76] for $HD(X^1\Sigma_g^+)$. There, they saw a similar phenomenon that can be seen in Figure 2.13: Around $T = 4$ K, all $\alpha(T, T_b)$ approach $\alpha(T, T_b = 0\,K)$ and each other, but around $T = 6$ K $\alpha(T, T_b \geq 1\,000\,K)$ enlarge the "distances" from $\alpha(T, T_b = 0\,K)$ and between each other. A similar enhancement for all T_b at a certain T was also shown in [55], where the rate coefficients are shown for $T \geq 50$ K.

2.2.2 CO^+

This Subsection shows the results from [34], which was devoted to RA of $O(2^3P)$ by $C^+(2^2P)$ through 7 channels:

$$A^2\Pi\ [O(2^3P) + C^+(2^2P)] \rightarrow CO^+(X^2\Sigma^+) + \hbar\omega, \tag{2.20}$$
$$D^2\Pi\ [O(2^3P) + C^+(2^2P)] \rightarrow CO^+(A^2\Pi\ ) + \hbar\omega, \tag{2.21}$$
$$D^2\Pi\ [O(2^3P) + C^+(2^2P)] \rightarrow CO^+(X^2\Sigma^+) + \hbar\omega, \tag{2.22}$$
$$1^2\Sigma^-[O(2^3P) + C^+(2^2P)] \rightarrow CO^+(A^2\Pi\ ) + \hbar\omega, \tag{2.23}$$
$$C^2\Delta\ [O(2^3P) + C^+(2^2P)] \rightarrow CO^+(A^2\Pi\ ) + \hbar\omega, \tag{2.24}$$
$$X^2\Sigma^+[O(2^3P) + C^+(2^2P)] \rightarrow CO^+(A^2\Pi\ ) + \hbar\omega, \tag{2.25}$$
$$2^2\Sigma^-[O(2^3P) + C^+(2^2P)] \rightarrow CO^+(A^2\Pi\ ) + \hbar\omega. \tag{2.26}$$

All involved PECs are illustrated in Figure 1.9 (from [34]) together with the $3^2\Pi$ state that has an avoided crossing with $D^2\Pi$ around 2.745 a_0. The $3^2\Pi$ state is depicted only for $R \leq 2.745\,a_0$. The leading term in RP-RKHS extrapolation

Table 2.10: The D_3 RP-RKHS extrapolation coefficients for the electronic states $X^2\Sigma^+$, $A^2\Pi$, $C^2\Delta$, $D^2\Pi$ (also $\widetilde{D}^2\Pi$), $1^2\Sigma^-$, and $2^2\Sigma^-$ of CO^+. The values are taken from [34, 64].

Electronic state	D_3 $[E_\mathrm{h}a_0^3]$
$X^2\Sigma^+$	0.460 387
$A^2\Pi$	−0.899 665
$C^2\Delta$	0.463 807
$D^2\Pi$, $\widetilde{D}^2\Pi$	0.475 589
$1^2\Sigma^-$	−1.109 83
$2^2\Sigma^-$	0.422 799

Table 2.11: Approximate Hönl-London factors for the processes involving the $^2\Pi$ and $^2\Sigma^\pm$ symmetries and also for the $^2\Delta \to {}^2\Pi$ process are summarised.

Process	$J_f = J_i + 1$	$J_f = J_i$	$J_f = J_i - 1$
$^2\Pi \to {}^2\Sigma^+$	$\frac{J_i}{2}$	$\frac{2J_i+1}{2}$	$\frac{J_i+1}{2}$
$^2\Sigma^\pm \to {}^2\Pi$	$J_i + 2$	$2J_i + 1$	$J_i - 1$
$^2\Pi \to {}^2\Pi$	$\frac{J_i(J_i+2)}{J_i+1}$	$\frac{2J_i+1}{J_i(J_i+1)}$	$\frac{(J_i+1)(J_i-1)}{J_i}$
$^2\Delta \to {}^2\Pi$	$\frac{J_i}{2}$	$\frac{2J_i+1}{2}$	$\frac{J_i+1}{2}$

of all electronic states involved in the RA study is

$$U(R \text{ large}) = \frac{D_3}{R^3} + \frac{D_4}{R^4}. \tag{2.27}$$

The D_3 values for the electronic states are summarised in Table 2.10.

The transition dipole-moment functions for all processes are illustrated in the bottom panel of Figure 1.9 (from [34]). Only for the D → A process,

$$T_q^1\left[\mathbf{d}(R)\right] = T_0^1\left[\mathbf{d}(R)\right] = d_z(R). \tag{2.28}$$

For the rest of the processes,

$$T_q^1\left[\mathbf{d}(R)\right] = T_{\pm1}^1\left[\mathbf{d}(R)\right] = \mp\frac{1}{\sqrt{2}}\left[d_x(R) \pm d_y(R)\right], \tag{2.29}$$

for which $d_x(R)$ or $d_y(R)$ are needed since $d_x(R) = d_y(R)$ for diatomic systems.

The Hönl-London factors for the $^2\Pi \to {}^2\Sigma^+$ and opposite transitions are summarised in [77] (Table I and explained in Table IV). The Hönl-London factors for the $^2\Pi \to {}^2\Pi$ process were introduced in [78] (Table I and Table II). Here, we show the Hönl-London factors in Table 2.11. The Hönl-London factors for the $^2\Delta \to {}^2\Pi$ transitions are taken the same as for $^2\Pi \to {}^2\Sigma^+$. The reason for it is explained in [34] (Appendix). The collision probability is $p_i = 2/27$ for all processes starting in either $^2\Pi$ or $^2\Delta$ states. For 1 → A and X → A, $p_i = 1/27$.

The process characteristics are summarised in Table 2.12. The number of target states is large for all considered processes. The ground state, $X^2\Sigma^+$, has the largest number of resonances (1 724). The $A^2\Pi$ state has the second largest number of resonances (1 188). The number of resonances that play a role in the studied processes, are, however, almost the same from both the states due to the

Table 2.12: Process characteristics for CO^+ radiative association processes are summarised, energies are in cm^{-1}.[a,b,c]

Process	n_{tot}	n_r	$\mathcal{D}_{\Lambda_f}$	n_v	n_{rv}
A → X	1 188	1 082	66 944.2	53	6 328
D → A	817	817	46 787.5	97	8 418
$\widetilde{D}$ → A	263	263	46 787.5	97	8 418
D → X	817	817	66 944.2	53	6 328
$\widetilde{D}$ → X	263	263	66 944.2	53	6 328
1 → A	285	285	46 787.5	97	8 418
C → A	226	226	46 787.5	97	8 418
X → A	1 724	1 089	46 787.5	97	8 418
2 → A	482	482	46 787.5	97	8 418

[a] According to the definitions of [8]: n_{tot} is the total number of orbital resonances supported by the initial electronic state, from which n_r is the number of symmetry-allowed shape resonances, i.e. the number of resonances which have a bound partner in the corresponding target electronic state allowed by the dipole-moment selection rules; $\mathcal{D}_{\Lambda_f}$ is the dissociation energy of the target electronic state from the ground $(v_f = 0, J_f = \Lambda_f)$ ro-vibrational state, n_v is the number of bound vibrational $(J_f = \Lambda_f)$ states of the target electronic state, n_{rv} is the total number of bound ro-vibrational states of the target electronic state $(J_f = \Lambda_f)$. Since the involved electronic states have the same dissociation limit: $\Delta E = 0$.
[b] The number of resonances are found by LEVEL 8.0. Some resonances for double-minimum states may have not been found.
[c] The $\widetilde{D}$ state denotes the approximative diabate illustrated in Figure 1.9.

Hönl-London factors. The $D^2\Pi$ and $2^2\Sigma^-$ states have also quite a few of them (more than we saw for the $HeLi^+$ continua). LEVEL 8.0 could not find more than 285 and 226 shape resonances for the $1^2\Sigma^-$ and $C^2\Delta$ continua. It is possible there are more shape resonances, which would be supported by Figure 2.14 where the found bound and quasibound states of $1^2\Sigma^-$ are shown. In the top panel, the mixing of the states from the inner and outer well is obvious. LEVEL 8.0 had difficulties to find $J > 0$ for $v = 10, 11$ and could not find any state at $v = 9$. Despite the irrelevance of mixing the bound states from the two wells of this electronic state, we should mention it here since this mixing influences also the search of shape resonances. From the bottom panel, it can be seen that not all resonances were found. Similarly, not all resonances may have been found for $C^2\Delta$ or even $D^2\Pi$ and $2^2\Sigma^-$ continua either.

This time, the wide or narrow resonances are not distinguished since the cross sections were calculated semiclassically and all resonances were taken into account by the Cauchy distribution formula (1.104). Because of the usage of the Cauchy distribution for all resonances, the exact n_{tot} is preferable. The resonance contribution may play a role at low temperatures. The number of significant shape resonances, however, can be checked by plotting energy levels, similarly as in Figure 2.14 or by comparison with a quantal calculation.

Figure 2.14: Bound and quasibound states of $CO^+(1^2\Sigma^-)$ show difficulties of finding the states with double minimum potential energy curves.

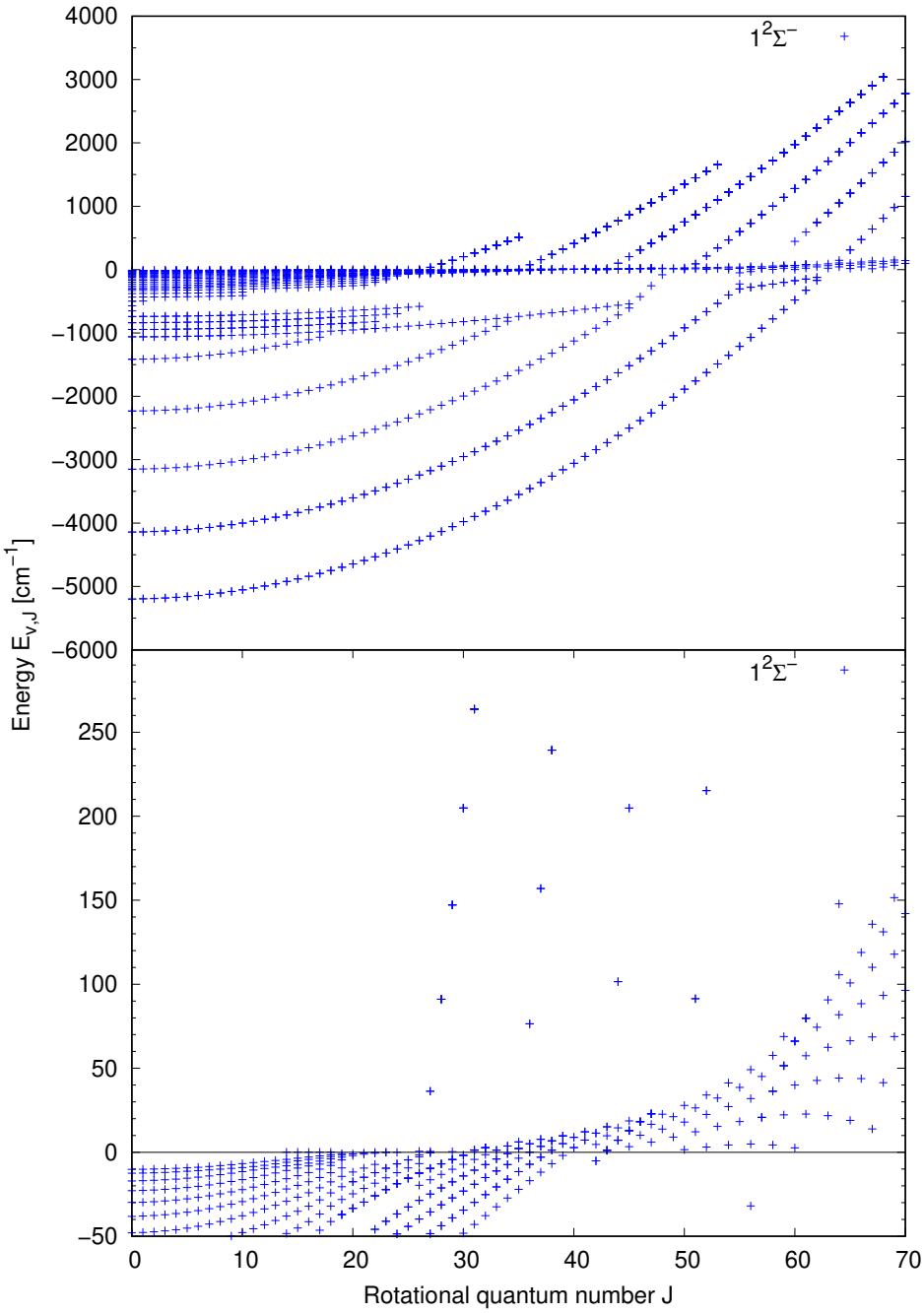

Figure 2.15: The cross sections of D → X of CO^+ calculated quantum mechanically (QM) and semiclassically (SC).

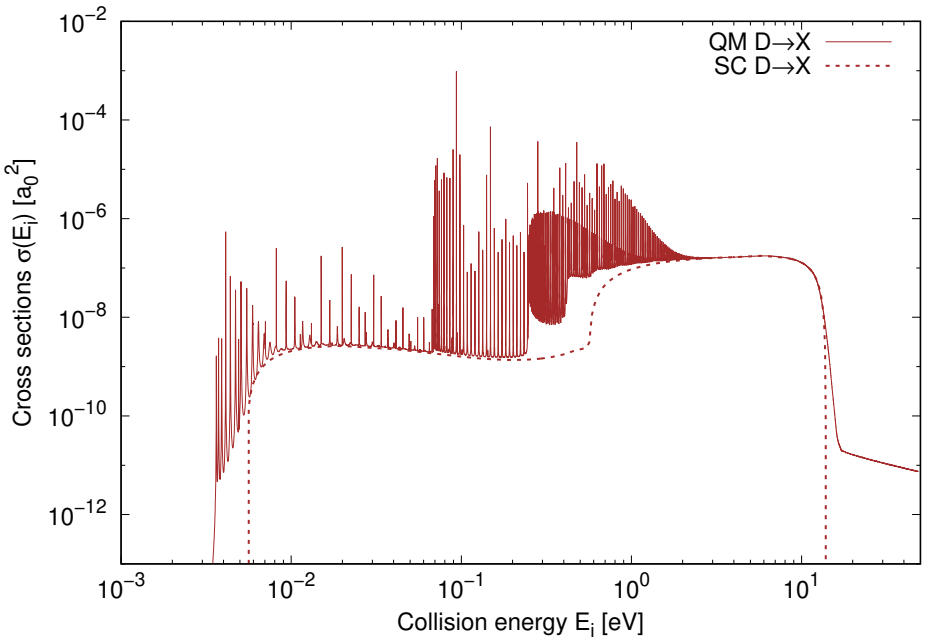

Cross Sections

The dynamics of processes that involve a double-minimum state need to be treated carefully. Usually, the Born-Oppenheimer (BO) approximation is valid, but in the states that have an avoided crossing with another electronic state, the BO approximation may fail. The $D^2\Pi$ state has a sharp avoided crossing with $3^2\Pi$. Therefore, the validity of the BO approximation in the D → X and D → A processes needs to be checked.

In Figure 2.15, the cross sections of D → X within the BO approximation are illustrated. Here we show only the quantal (QM) and semiclassical (SC) results. The resonance structure is rich and dense from energies slightly above 0.56 eV because of the two minima. This energy corresponds to the $U(R)$ at around the internuclear distance of the avoided crossing. From the energy-spacing of the resonances, it can be determined from which well they stem. The energy difference between two rotational levels of the same vibration is approximately

$$E_{v,J+1} - E_{v,J} = \frac{\hbar^2}{\mu R^2}(J+1) = 2B_0(J+1), \tag{2.30}$$

which can be deduced from the theory for rotational-vibrational spectroscopy that can be found, for instance, in [79]. Further, the two-minima effect can be viewed from the SC cross section, where the values increase rapidly. This is also noticable in the QM cross section, but it is more obvious in the SC one. This impact on the cross section suggests that the BO approximation fails and the diabatic representation is necessary.

The diabatic representation for CO^+ is, however, a very demanding task. Due to the presence of many electronic states of $^2\Pi$ symmetry that mix with $D^2\Pi$ and $3^2\Pi$, it is too complicated to derive the full diabatic representation. Hence, only

Figure 2.16: The quantal (QM) $\widetilde{\mathrm{D}} \to \mathrm{X}$ cross sections are compared to the QM $\mathrm{D} \to \mathrm{X}$ cross sections. The studied system is the CO^+ molecular ion.

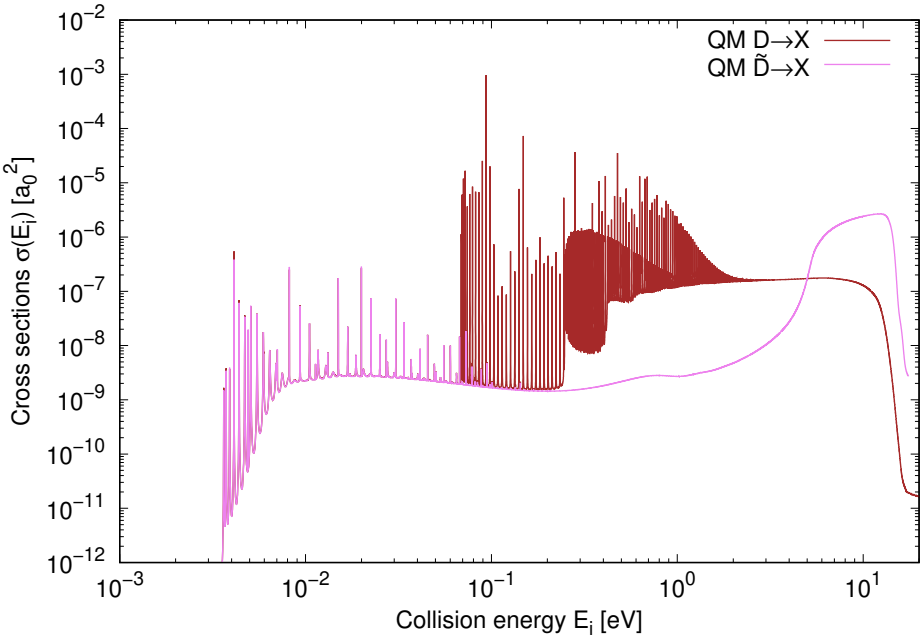

a sort of diabatisation of the $\mathrm{D}^2\Pi$ and $3^2\Pi$ states was performed, resulting in what we call a "quasidiabatic approximation" described in detail in [34]. We will denote this approximative diabate $\widetilde{\mathrm{D}}^2\Pi$ which is also illustrated in Figure 1.9. This $\widetilde{\mathrm{D}}^2\Pi$ state was used not only for the transition to $\mathrm{X}^2\Sigma^+$ but also for the transition to $\mathrm{A}^2\Pi$. We can add to processes (2.20)-(2.26)

$$\widetilde{\mathrm{D}}^2\Pi \;\; [\mathrm{O}(2^3\mathrm{P}) + \mathrm{C}^+(2^2\mathrm{P})] \to \mathrm{CO}^+(\mathrm{A}^2\Pi\;) + \hbar\omega, \tag{2.31}$$

$$\widetilde{\mathrm{D}}^2\Pi \;\; [\mathrm{O}(2^3\mathrm{P}) + \mathrm{C}^+(2^2\mathrm{P})] \to \mathrm{CO}^+(\mathrm{X}^2\Sigma^+) + \hbar\omega. \tag{2.32}$$

The corresponding TDMs are illustrated for both the processes in Figure 1.9.

The difference in the $\widetilde{\mathrm{D}} \to \mathrm{X}$ and $\mathrm{D} \to \mathrm{X}$ cross sections are remarkable and can be seen in Figure 2.16. The inner-well shape resonances expectedly vanished. The abrupt increase of the cross sections at $E_i > 0.56$ eV is gone too. That the diabatic representation is only approximative is perhaps seen around 0.7 eV by the very small, almost unnoticable, "hump". For $E > 0.7$ eV, the $\widetilde{\mathrm{D}} \to \mathrm{X}$ cross sections increase slowly until they overcome the $\mathrm{D} \to \mathrm{X}$ cross sections. This is due to the larger TDM of $\widetilde{\mathrm{D}} \to \mathrm{X}$ around 2 a_0.

The influence of the avoided crossing was small in $\mathrm{D} \to \mathrm{A}$, which can be seen in Figure 2.17. This is because of large TDM in the internuclear distances corresponding to the outer well. Therefore, the inner well was not favoured as it was in the case of $\mathrm{D} \to \mathrm{X}$ where the TDM in the outer well was very small. The $\widetilde{\mathrm{D}} \to \mathrm{A}$ cross sections are compared with the $\mathrm{D} \to \mathrm{A}$ ones in the Figure. The lack of the inner-well resonances can be seen here, too. The small change at larger collision energies suggests a different PEC of the initial state and different TDM. The TDM values of $\widetilde{\mathrm{D}} \to \mathrm{A}$ and $\mathrm{D} \to \mathrm{A}$ do not differ as much in their absolute values as it was in the case of $\widetilde{\mathrm{D}} \to \mathrm{X}$ and $\mathrm{D} \to \mathrm{X}$. Hence the smaller difference

Figure 2.17: The quantal (QM) $\widetilde{\mathrm{D}} \rightarrow \mathrm{A}$ cross sections are compared to the QM $\mathrm{D} \rightarrow \mathrm{A}$ cross sections. The studied system is the CO^+ molecular ion.

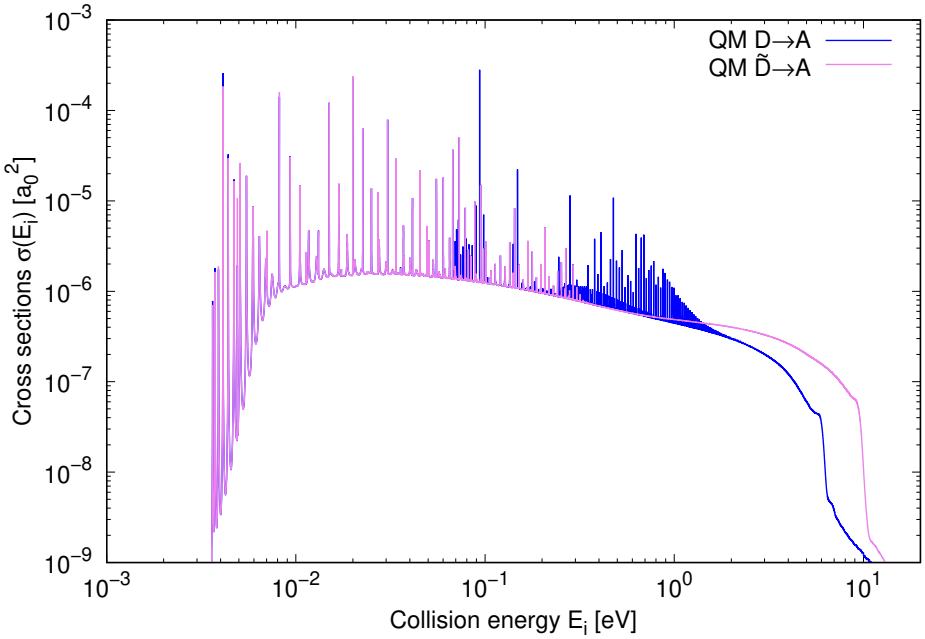

in the cross sections in the inner-well energies. In further calculations only the diabate $\widetilde{\mathrm{D}}$ was taken into account.

The cross sections of all processes of the interest, calculated by the semiclassical (SC) method, are illustrated in Figure 2.18 [34]. The resonance contribution is added to the SC cross sections and shown by the SC+BW curves. These are compared to the quantal (QM) cross sections. The Figure shows that the relevant resonances were found by LEVEL 8.0 for all the processes. At low energies, the Breit-Wigner (BW) theory adds an artificial decrease from larger cross-section values. This comes from the denominator in Equation (1.114). This, however, causes an insignificant error in rate coefficients due to the averaging in the rate-coefficient formula (1.82). The factor

$$E_i e_i^{-\frac{E_i - E_{v_f, J_f}}{k_\mathrm{B} T}} \tag{2.33}$$

is very small for such small E_i.

The cross sections of $\widetilde{\mathrm{D}} \rightarrow \mathrm{A}$ unexpectedly exceed the $\mathrm{A} \rightarrow \mathrm{X}$ ones. The $\mathrm{A}^2\Pi$ and $\mathrm{X}^2\Sigma^+$ states have only a shift of minima equal to 0.243 a_0, and the $\mathrm{X}^2\Sigma^+$ state as a ground state is expected to have the largest number of bound states. However, it has 6 328 bound states and the $\mathrm{A}^2\Pi$ state has 8 418. This is because the well of $\mathrm{A}^2\Pi$ is wider than the well of the ground state. In addition, the impact of the $\mathrm{A} \rightarrow \mathrm{X}$ TDM is smaller than of the $\widetilde{\mathrm{D}} \rightarrow \mathrm{A}$ TDM, which has larger values at more internuclear distances. As a consequence of all mentioned, the $\widetilde{\mathrm{D}} \rightarrow \mathrm{A}$ cross sections turn out to be larger than the $\mathrm{A} \rightarrow \mathrm{X}$ cross sections from $E_i \approx 0.015$ eV.

The $\widetilde{\mathrm{D}} \rightarrow \mathrm{X}$ process achieves the largest cross sections above around 6 eV. This is mainly because of the large TDM at small R (we have mentioned this earlier). Otherwise, the values are quite small, even comparable to the $\mathrm{X} \rightarrow \mathrm{A}$

cross sections that are the second smallest or smallest ones. Similar values can be seen also for the $1 \rightarrow$ A process for 0.01 eV$< E_i < 1$ eV. Although the TDM of $1 \rightarrow$ A is very small at almost all R, it achieves similar values at these energies as $\widetilde{\mathrm{D}} \rightarrow$ X. The explanation may be due to the favourable FC overlap (the shift of minima is 0.212 a_0 and the minima are shallower than in the ground state). Another reason may be the large number of the target bound states in $\mathrm{A}^2\Pi$.

The $1 \rightarrow$ A process has something in common with A $\rightarrow$ X: The cross section values start from larger values and decrease. This is not an artificial addition from the BW theory since this feature is present also in the QM cross sections. This is because both the processes start in an electronic state that is attractive in the long range. The rest of the initial states are repulsive in the long range (they have a barrier).

The $\mathrm{C}^2\Delta$ state looks very similar to $1^2\Sigma^-$. Since from both the states RA into the same state ($\mathrm{A}^2\Pi$) was calculated and the TDMs also resemble each other, one would expect very similar cross sections. The C $\rightarrow$ A cross sections, however, are a bit larger and the $1 \rightarrow$ A cross sections resemble more those from $\widetilde{\mathrm{D}} \rightarrow$ X and X $\rightarrow$ A at $0.01 < E_i < 1$ eV. The reason may be a small difference in the TDMs of C $\rightarrow$ A and $1 \rightarrow$ A around the wells' internuclear distances. The TDM of C $\rightarrow$ A is a bit larger.

Up to around 1 eV, the $2 \rightarrow$ A cross sections are the smallest. At 0.9 eV $\leq E_i \leq 2$ eV, a rich resonance structure from the inner well can be seen. Between 0.9 eV and 2 eV, the cross sections rapidly increase from the smallest values amongst all the processes to the largest up to 6 eV.

Although $2^2\Sigma^-$ has obviously an avoided crossing too (from Figure 1.9), the BO approximation must suffice because the *ab initio* calculations revealed another upper state having an avoided crossing with the diabate. This complicates all the calculations and the effort would be too costly for such a less important process when compared to the rest of the considered processes.

Rate Coefficients

The rate coefficients of all processes are illustrated in Figure 2.19. At low temperatures, A $\rightarrow$ X is the most efficient process. At around 136 K, the $\widetilde{\mathrm{D}} \rightarrow$ A process prevails up to around 20 000 K when $\widetilde{\mathrm{D}} \rightarrow$ X starts to have the largest rate coefficients. At low temperatures, the third most efficient process is $1 \rightarrow$ A up to around 136 K where the C $\rightarrow$ A process exceeds it. The C $\rightarrow$ A process is then overcome by $2 \rightarrow$ A at around 2 860 K. The $2 \rightarrow$ A process has larger rate coefficients than A $\rightarrow$ X at $T \geq 7\,150$ K. At 16 700 K $\leq T \leq$ 24 200 K, $2 \rightarrow$ A is the most efficient process. At $T >$ 24 200 K, $\widetilde{\mathrm{D}} \rightarrow$ X is the most efficient. At low temeperatures, C $\rightarrow$ A and X $\rightarrow$ A have similar rate-coefficient values. At these temperatures, $2 \rightarrow$ A is the least efficient process up to around 2 000 K. For $T >$ 2 000 K, X $\rightarrow$ A is the least efficient process.

The rate coefficient for the depopulation of the continuum of the dissociation limit $[\mathrm{C}^+(2^2\mathrm{P}) + \mathrm{O}(2^3\mathrm{P})]$ is shown in Table 2.13. It was obtained as a sum of the rate coefficients for A $\rightarrow$ X, X $\rightarrow$ A, $\widetilde{\mathrm{D}} \rightarrow$ A, $\widetilde{\mathrm{D}} \rightarrow$ X, C $\rightarrow$ A, $1 \rightarrow$ A and $2 \rightarrow$ A. The rate coefficients of all the processes and D $\rightarrow$ A and D $\rightarrow$ X are summarised in Table 2.13.

Figure 2.20 (from [64]) compares the rate coefficients of $\widetilde{\mathrm{D}} \rightarrow$ X with D $\rightarrow$ X in the top panel and of $\widetilde{\mathrm{D}} \rightarrow$ A with D $\rightarrow$ A in the bottom panel. They are

Figure 2.18: The semiclassical cross sections (SC) with (+BW) and without the resonance contribution are compared to the quantal (QM) cross sections. The studied system is the CO^+ molecular ion. [34, 64].

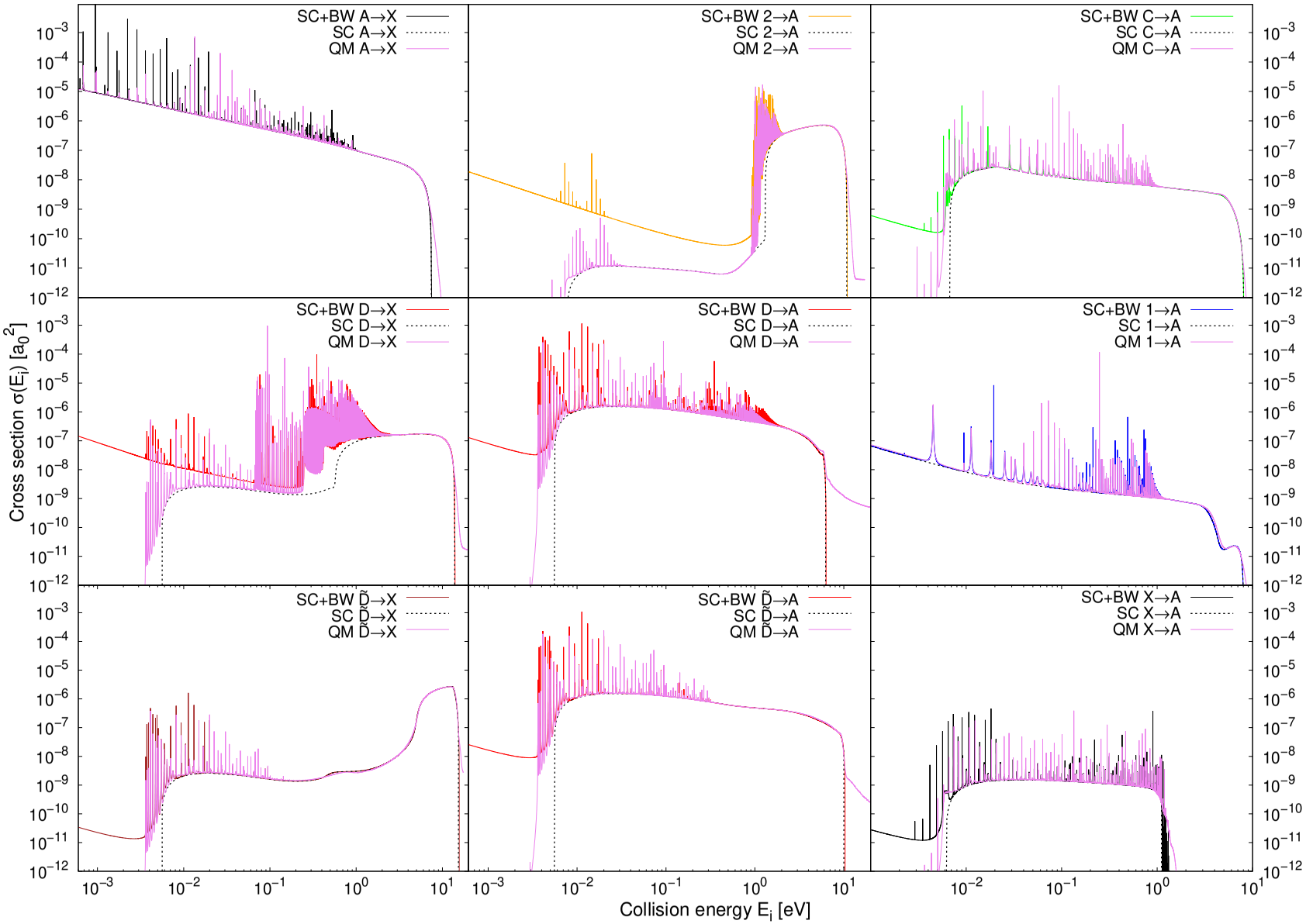

Table 2.13: Rate coefficients [cm^3s^{-1}] for the CO^+ molecular ion calculated by the SC+BW method. Rate coefficient for the depopulation for the continuum [$C^+(2^2P)+O(2^3P)$] obtained as a sum of $A \to X$, $X \to A$, $\widetilde{D} \to A$, $\widetilde{D} \to X$, $C \to A$, $1 \to A$ and $2 \to A$. The results up to 10 000 K are taken from [34, 64].[a]

T(K)	$A \to X$	$X \to A$	$D \to A$	$\widetilde{D} \to A$	$D \to X$	$\widetilde{D} \to X$	$C \to A$	$1 \to A$	$2 \to A$	α_{dep}
10	7.30(-18)	1.91(-22)	7.52(-20)	7.52(-20)	2.69(-22)	2.67(-22)	2.83(-22)	7.20(-20)	3.09(-24)	7.45(-18)
20	6.62(-18)	8.12(-22)	5.89(-19)	5.89(-19)	1.62(-21)	1.61(-21)	2.62(-21)	6.43(-20)	9.77(-24)	7.28(-18)
30	6.27(-18)	1.46(-21)	1.24(-18)	1.24(-18)	3.01(-21)	2.99(-21)	7.46(-21)	5.78(-20)	1.48(-23)	7.58(-18)
50	5.90(-18)	2.63(-21)	2.43(-18)	2.43(-18)	5.17(-21)	5.15(-21)	2.08(-20)	4.94(-20)	2.12(-23)	8.41(-18)
100	5.37(-18)	4.54(-21)	4.29(-18)	4.29(-18)	9.66(-21)	7.88(-21)	4.71(-20)	3.98(-20)	2.53(-23)	9.76(-18)
200	4.82(-18)	6.69(-21)	6.20(-18)	6.18(-18)	7.66(-20)	9.87(-21)	7.06(-20)	3.36(-20)	2.87(-23)	1.11(-17)
500	4.27(-18)	9.82(-21)	8.58(-18)	8.43(-18)	5.36(-19)	1.17(-20)	8.98(-20)	2.89(-20)	4.76(-23)	1.28(-17)
1 000	3.90(-18)	1.23(-20)	9.95(-18)	9.57(-18)	1.22(-18)	1.40(-20)	9.92(-20)	2.71(-20)	1.15(-22)	1.36(-17)
2 000	3.52(-18)	1.47(-20)	1.07(-17)	1.02(-17)	1.84(-18)	2.19(-20)	1.10(-19)	2.65(-20)	1.63(-20)	1.40(-17)
2 500	3.39(-18)	1.52(-20)	1.09(-17)	1.04(-17)	1.99(-18)	2.65(-20)	1.14(-19)	2.64(-20)	5.88(-20)	1.40(-17)
3 000	3.27(-18)	1.53(-20)	1.09(-17)	1.06(-17)	2.11(-18)	3.13(-20)	1.17(-19)	2.64(-20)	1.45(-19)	1.42(-17)
4 000	3.09(-18)	1.49(-20)	1.10(-17)	1.08(-17)	2.35(-18)	4.15(-20)	1.22(-19)	2.63(-20)	4.75(-19)	1.46(-17)
6 000	2.82(-18)	1.30(-20)	1.09(-17)	1.13(-17)	2.82(-18)	7.59(-20)	1.31(-19)	2.61(-20)	1.73(-18)	1.61(-17)
8 000	2.63(-18)	1.09(-20)	1.07(-17)	1.17(-17)	3.28(-18)	2.06(-19)	1.36(-19)	2.57(-20)	3.50(-18)	1.82(-17)
10 000	2.47(-18)	9.23(-21)	1.04(-17)	1.19(-17)	3.72(-18)	6.05(-19)	1.40(-19)	2.49(-20)	5.52(-18)	2.07(-17)
16 000	2.11(-18)	5.91(-21)	9.24(-18)	1.21(-17)	4.91(-18)	4.80(-18)	1.43(-19)	2.17(-20)	1.15(-17)	3.06(-17)
20 000	1.91(-18)	4.62(-21)	8.41(-18)	1.18(-17)	5.54(-18)	1.02(-17)	1.39(-19)	1.95(-20)	1.46(-17)	3.87(-17)
25 000	1.69(-18)	3.56(-21)	7.45(-18)	1.13(-17)	6.14(-18)	1.85(-17)	1.32(-19)	1.70(-20)	1.74(-17)	4.91(-17)
32 000	1.44(-18)	2.62(-21)	6.31(-18)	1.05(-17)	6.64(-18)	3.06(-17)	1.19(-19)	1.41(-20)	1.95(-17)	6.22(-17)
50 000	9.98(-19)	1.46(-21)	4.31(-18)	8.33(-18)	6.78(-18)	5.25(-17)	8.98(-20)	9.34(-21)	1.98(-17)	8.17(-17)
64 000	7.84(-19)	1.04(-21)	3.36(-18)	6.97(-18)	6.36(-18)	5.96(-17)	7.30(-20)	7.18(-21)	1.82(-17)	8.56(-17)
100 000	4.79(-19)	5.56(-22)	2.02(-18)	4.66(-18)	4.99(-18)	5.92(-17)	4.65(-20)	4.24(-21)	1.36(-17)	7.80(-17)

[a] $x(-y) \equiv x \times 10^{-y}$

Figure 2.19: Rate coefficients of radiative association processes for CO^+ are illustrated. These results are taken from [34, 64].

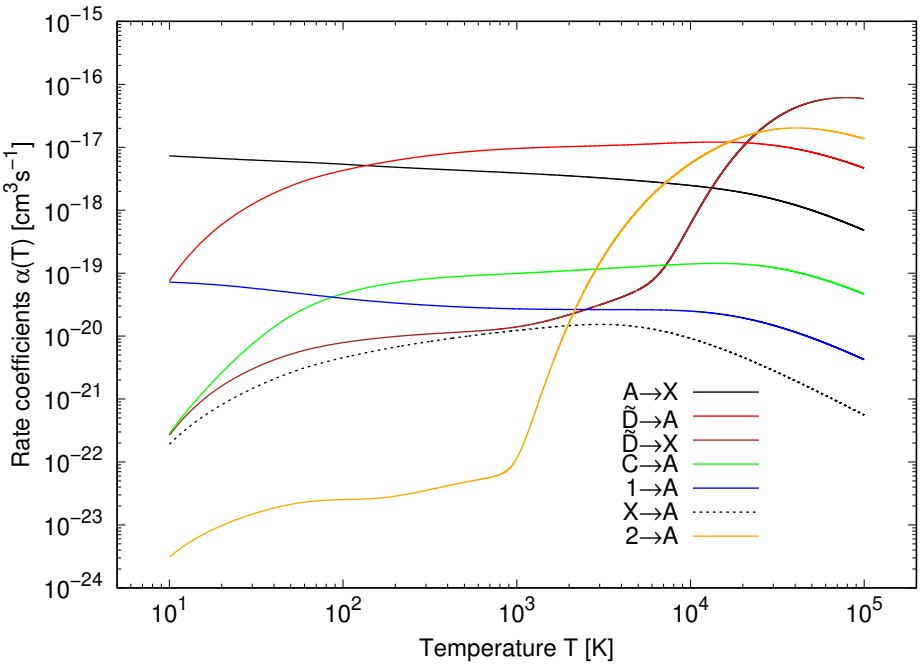

also summarised in Table 2.13. The results are in agreement with what has been said earlier: The influence of the inner well of $D^2\Pi$ is strong in D → X and it is suppressed by the large values of TDM in D → A. The TDM of D → A is large not only at R corresponding to the inner well, but also at R of the outer well. Actually, the TDM is here the largest among all TDMs shown in Figure 1.9. This enhances the influence of the outer well in D → A. The TDM of D → X is, on the other hand, very small in comparison to the inner-well values. Thus, the influence of the inner well is amplified in D → X.

Typically, resonance contribution to rate coefficients is small. This is discussed in Subsection 2.2.1. There, however, we used dense grids for wide resonances and the Cauchy distribution only for narrow resonances. Here, since the SC method does not deal with any resonances, all the resonances have to be treated by the approximative formula. As a consequence, wide resonances' contribution may be overestimated and the error brought by this depends on the number of wide resonances and their widths. Figure 2.21 shows the resonance $\alpha_{\mathrm{r}}(T)$ and background (from SC) $\alpha_{\mathrm{bg}}(T)$ contributions for 6 transitions. In all shown cases, $\alpha_{\mathrm{r}}(T)$ is larger than $\alpha_{\mathrm{bg}}(T)$ at low temperatures.

In the two top panels of Figure 2.21, the transition with the most resonances, X → A, is compared to the transition with the least found resonances, C → A. Although $\alpha_{\mathrm{r}}(T)$ is larger than $\alpha_{\mathrm{bg}}(T)$ for X → A up to larger temperatures than it is for C → A, the values of $\alpha_{\mathrm{r}}(T)$ for C → A are larger than those for X → A. The reason may be that in Equation (1.104) the values of J_i and E_{v_i,J_i,Λ_i} play a role and may influence the results.

In the two middle panels of Figure 2.21, we compare the $\widetilde{\mathrm{D}}$ → A and D → A results. The resonance contribution for $\widetilde{\mathrm{D}}$ → A misses the inner-well resonances, which correspond to higher collision energies and, thus, $\alpha_{\mathrm{r}}(T)$ is smaller at larger temperatures. The background contribution differs slightly. The main reason is

Figure 2.20: Top panel: rate coefficients of $\widetilde{D} \rightarrow X$ and $D \rightarrow X$; bottom panel: rate coefficients of $\widetilde{D} \rightarrow A$ and $D \rightarrow A$. The studied system is the CO^+ molecular ion. These results are taken from [64].

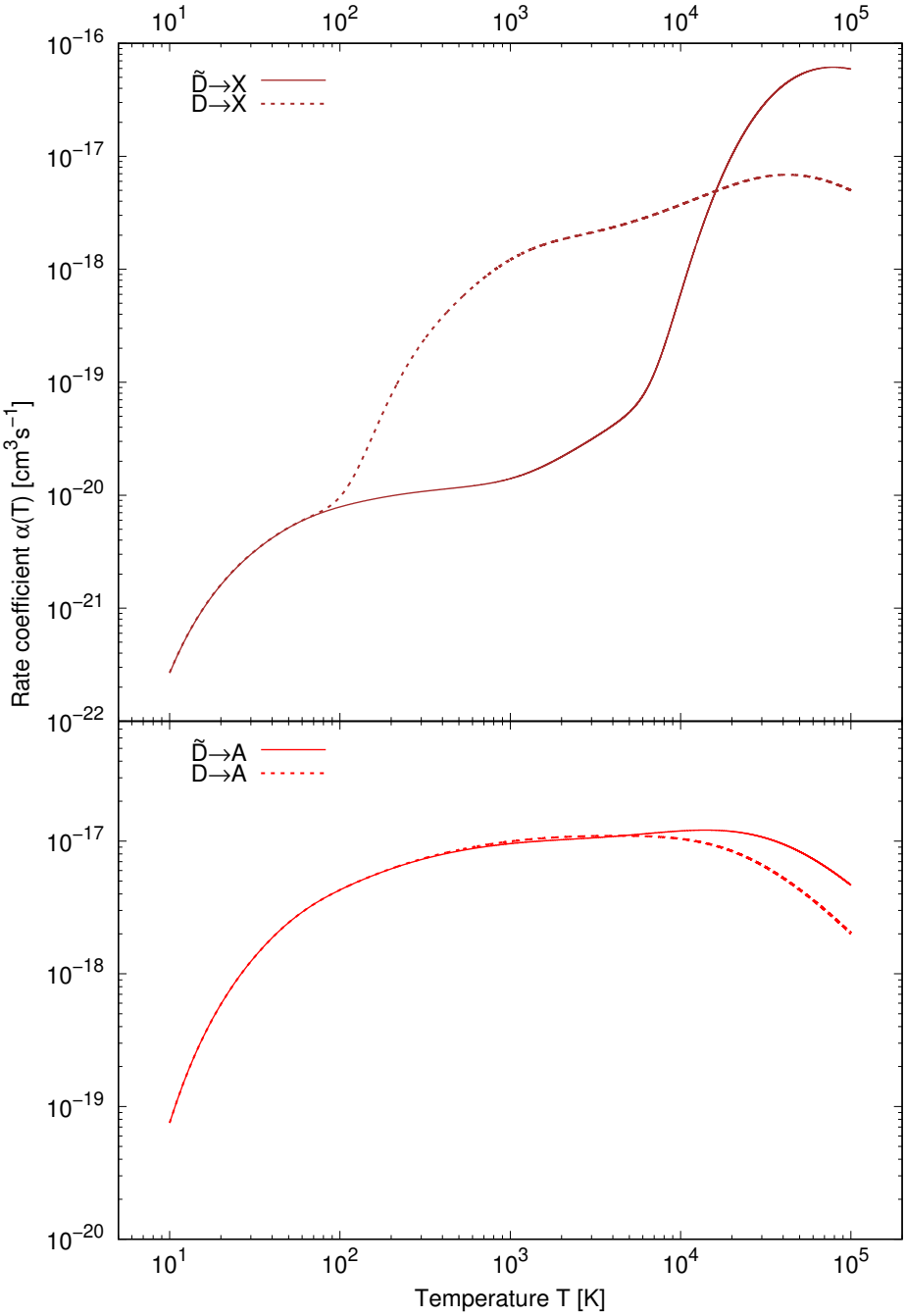

the shape of the transition-dipole moment function for D $\rightarrow$ A.

Lastly, the two bottom panels of Figure 2.21 show $\alpha_{\mathrm{r}}(T)$ and $\alpha_{\mathrm{bg}}(T)$ for $\widetilde{\mathrm{D}} \rightarrow$ X and D $\rightarrow$ X. The resonance contribution is very different in these two transitions. For $\widetilde{\mathrm{D}} \rightarrow$ X, it resembles $\alpha_{\mathrm{r}}(T)$ for $\widetilde{\mathrm{D}} \rightarrow$ A. The $\alpha_{\mathrm{r}}(T)$ of D $\rightarrow$ X, however, does not resemble $\alpha_{\mathrm{r}}(T)$ of D $\rightarrow$ A although the same resonances contribute. The reason is in different radiative widths because of the different target bound states (different PECs and TDMs, in other words). The background contributions for $\widetilde{\mathrm{D}} \rightarrow$ X and D $\rightarrow$ X are different, which has been already explained earlier. The reason is the combination of the different initial PEC and the shape of TDMs of $\widetilde{\mathrm{D}} \rightarrow$ X and D $\rightarrow$ X, especially the TDM values in the inner- and outer-well values.

2.3 Radiative Charge Transfer

The radiative charge transfer (RCT) process was examined between continuum states of $\mathrm{b}^3\Sigma^+$ and $\mathrm{a}^3\Sigma^+$ of HeLi^+. Similarly, as in Section 2.1, SLA was used here. Thus, we omit Ω_i and Ω_f indices and $\Omega = \Lambda = 0$ for both the states. Equation (2.1) and Equation (2.2) are valid, too. This Section discusses the study published also in [33].

The PECs and b $\rightarrow$ a transition dipole-moment function are illustrated in Figure 1.8. The energy difference of the dissociation limits is the same as in the case of the RLT calculations in Section 2.1 ($\Delta E = 0.623\,941$ eV$\approx 5\,032.4$ cm^{-1}) and the positions of the minima of the two electronic states (shifted by $\approx 7.056\, a_0$) play a role in the values of the Einstein coefficients for spontaneous emission and consequently also in the values of cross sections. As it was mentioned in Section 2.1, the maximum of $d_z(R)$ around the minimum of the initial electronic state and a nonzero value around the minimum of the final one can enhance the values of Einstein coefficients and, thus, of cross sections, too.

The $\mathrm{b}^3\Sigma^+$ state has 214 shape resonances (the lowest rotational quantum number is 6 and the largest is 102). The $\mathrm{a}^3\Sigma^+$ state has 707 shape resonances (the lowest rotational quantum number is 4 and the largest one is 166). This entails the resonance contribution must be taken into account in order to obtain cross sections and rate coefficients with satisfactory precision for low energies and low temperatures. The resonances of both the states play a role. In order to treat them correctly, the cross section was divided into terms

$$\sigma_{\mathrm{b}}(E_i) \approx \sigma_{\mathrm{b-b}}(E_i) + \sigma_{\mathrm{b-w}}(E_i), \tag{2.34}$$

$$\sigma_{\mathrm{w}}(E_i) \approx \sigma_{\mathrm{w-b}}(E_i) + \sigma_{\mathrm{w-w}}(E_i), \tag{2.35}$$

$$\sigma_{\mathrm{n}}(E_{v_i,J_i}) \approx \sigma_{\mathrm{n-b}}(E_{v_i,J_i}) + \sigma_{\mathrm{n-w}}(E_{v_i,J_i}), \tag{2.36}$$

where $\sigma_{\mathrm{b}}(E_i)$ denotes the background cross sections comprising the pure free-free transitions $\sigma_{\mathrm{b-b}}(E_i)$ and also free-quasibound transitions $\sigma_{\mathrm{b-w}}(E_i)$ where only wide resonances ($\Gamma^{\mathrm{tun}}_{v_f,J_f}/E_{v_f,J_f} > 10^{-10}$) are taken into account. Equation (2.35) is for the wide-resonance contribution $\sigma_{\mathrm{w}}(E_i)$ comprising quasibound-free $\sigma_{\mathrm{w-b}}(E_i)$ transitions and quasibound-quasibound $\sigma_{\mathrm{w-w}}(E_i)$ transitions where again only wide resonances ($\Gamma^{\mathrm{tun}}_{v_m,J_m}/E_{v_m,J_m} > 10^{-10}$, $m = i, f$) are taken into account. Finally, $\sigma_{\mathrm{n}}(E_{v_i,J_i})$ is the narrow-resonance contribution that includes the

Figure 2.21: Rate coefficients for six radiative association processes studied on CO^+ are illustrated with their background α_{bg} and resonance α_r contributions. Top panels - X $\rightarrow$ A and C $\rightarrow$ A; middle panels - $\widetilde{D} \rightarrow$ A and D $\rightarrow$ A; bottom panels - $\widetilde{D} \rightarrow$ X and D $\rightarrow$ X.

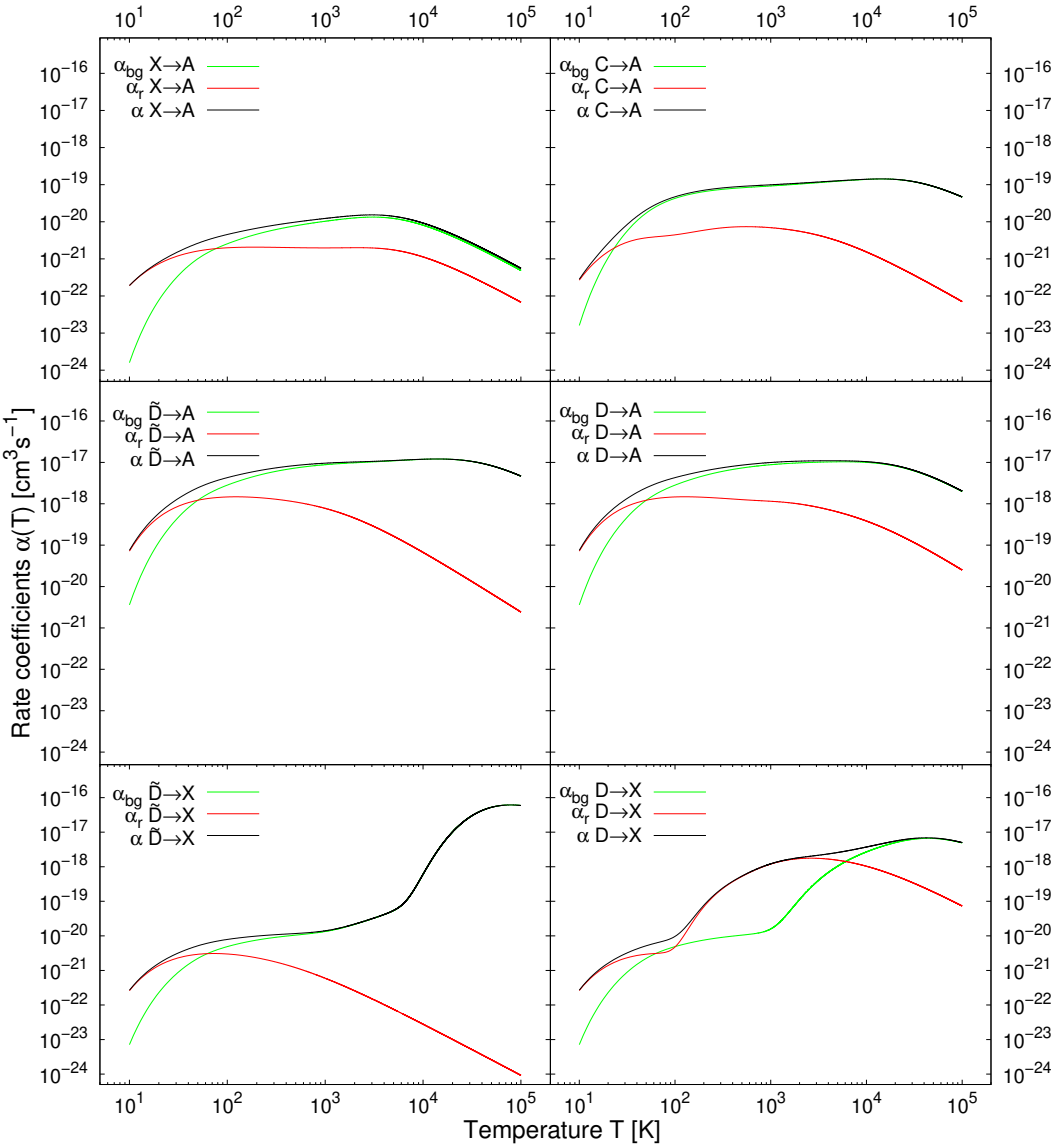

Figure 2.22: The wide contribution to cross sections $\sigma_{\mathrm{w}}(E_i)$ of HeLi^+ illustrated around ($\pm 5\Gamma^{\mathrm{tun}}_{0,94}$) a wide resonance with $E_{0,94} = 244.398\,268\,2\ \mathrm{cm}^{-1}$. The wide-background contribution $\sigma_{\mathrm{w-b}}(E_i)$ is shown by the green colour and the wide-wide contribution $\sigma_{\mathrm{w-w}}(E_i)$ by the red colour.

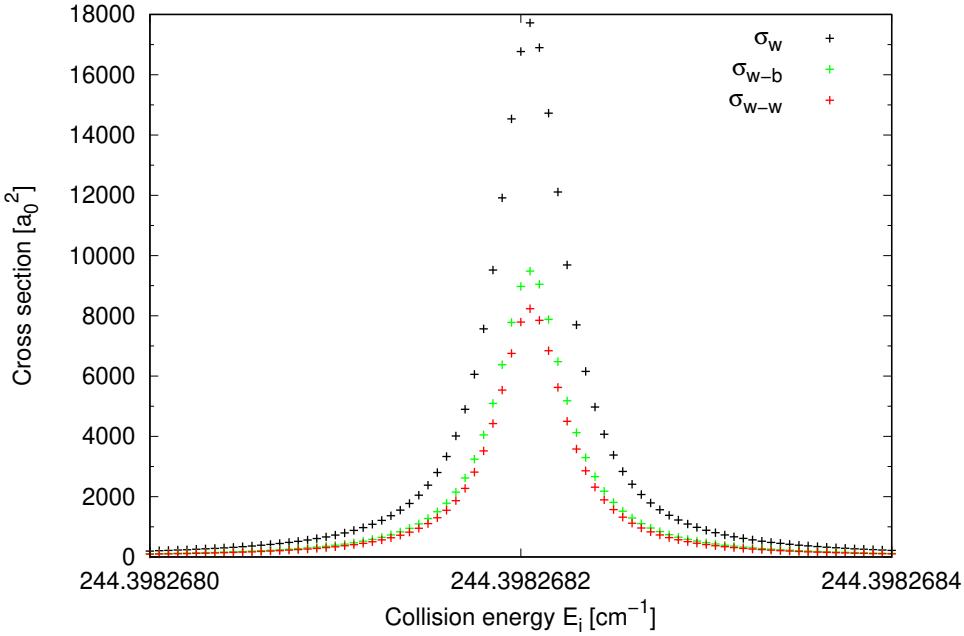

quasibound-free $\sigma_{\mathrm{n-b}}(E_{v_i,J_i})$ transitions and quasibound-free $\sigma_{\mathrm{n-w}}(E_{v_i,J_i})$ transitions. Both narrow and wide initial-state resonances are considered, while from the final continuum only the wide resonances are taken into account. The approximation sign indicates that the contribution from the final narrow resonances is neglected.

During the background contribution calculation, neighbourhoods of all resonances of the initial continuum are skipped. In $\sigma_{\mathrm{b-b}}(E_i)$, also the neighbourhoods of final continuum resonances are skipped. The integration over resonance neighbourhoods (either from the initial or final continuum) needs a significantly smaller integration step; therefore, the terms $\sigma_{\mathrm{b-w}}(E_i)$, $\sigma_{\mathrm{w-b}}(E_i)$ and $\sigma_{\mathrm{w-w}}(E_i)$ treat the neighbourhoods separately.

In Figure 2.22, the cross sections around a shape resonance in the initial continnum with $E_{0,94} \approx 244.398\ \mathrm{cm}^{-1}$ is illustrated. By the black colour, $\sigma_{\mathrm{w}}(E_{0,94} - \delta E, E_{0,94} + \delta E)$ is plotted, where $\delta E = 1\ \mathrm{cm}^{-1}$ for $0.001\ \mathrm{cm}^{-1} \leq \Gamma^{\mathrm{tun}}_{v,J} \leq 0.5\ \mathrm{cm}^{-1}$, otherwise $\delta E = 5\Gamma^{\mathrm{tun}}_{v,J}$. For this resonance, $\Gamma^{\mathrm{tun}}_{0,94} = 3.773\,739 \times 10^{-8}\ \mathrm{cm}^{-1}$ and, thus, $\delta_{r_i} = (E_{0,94} - 5\Gamma^{\mathrm{tun}}_{0,94}, E_{0,94} + 5\Gamma^{\mathrm{tun}}_{0,94})$. The terms $\sigma_{\mathrm{w-b}}(E_i)$ and $\sigma_{\mathrm{w-w}}(E_i)$ are shown by the green and blue colour. Surprisingly, both the contributions are comparable. This is caused by the large number of the final shape resonances ($n_{\mathrm{tot}} = 707$). If the final electronic state had few resonances, $\sigma_{\mathrm{w-b}}(E_i)$ would be much larger than $\sigma_{\mathrm{w-w}}(E_i)$.

The narrow-resonance contribution, as it is suggested in Equation (2.36), is evaluated only at energies of the narrow resonances. The rate coefficient for

Figure 2.23: The partial cross section of radiative charge transfer on $HeLi^+$ at $E_i = 0.362$ meV are illustrated and divided into two terms: the resonant at $J_i = 30$ and nonresonant $J_i \neq 30$.

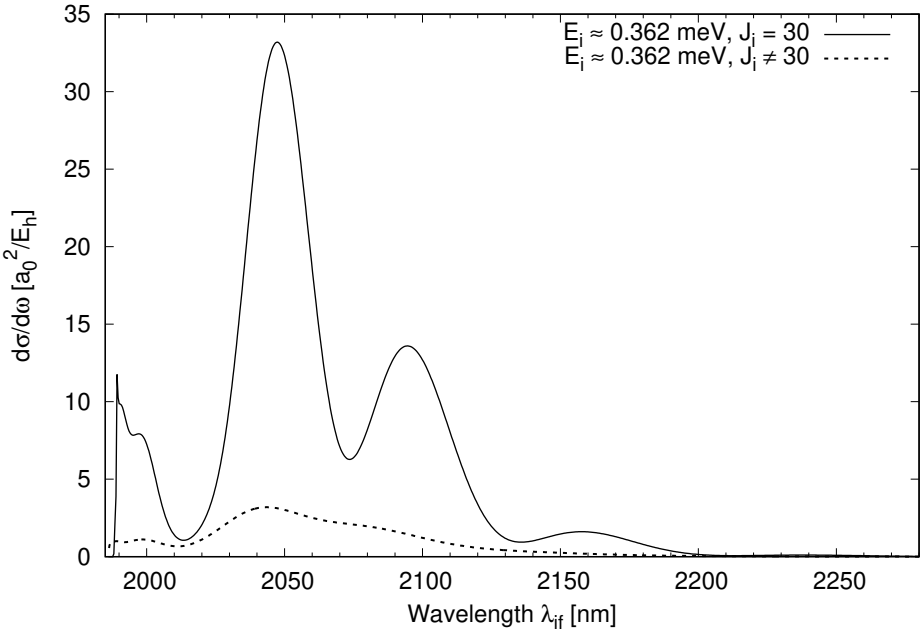

narrow resonances is then approximated as

$$\alpha_{\mathrm{n}}(T) = \sqrt{\frac{8}{\mu\pi}}\sqrt{\left(\frac{1}{k_{\mathrm{B}}T}\right)^3}\sum_i{}' 2\Gamma^{\mathrm{tun}}_{v_i,J_i} E_{v_i,J_i}\sigma_{\mathrm{n}}(E_{v_i,J_i})e^{-E_{v_i,J_i}/k_{\mathrm{B}}T}, \tag{2.37}$$

where the sum is over all initial narrow resonances.

Partial Cross Sections

In order to show the resonance contribution in comparison with the nonresonant part, collision energy $E_i = 0.362$ meV was chosen and Equation (1.116) divided into two terms: to a partial wave $J_i = 30$, which corresponds to a resonance $v_i = 20, J_i = 30$; and to all partial waves except for $J_i = 30$. These two terms are illustrated in Figure 2.23 (the right-top panel of Fig. 2 in [33]). The sum of these two terms gives the partial cross section at $E_i = 0.362$ meV. The resonant part is noticably larger than the nonresonant part. Some peaks can be seen in the resonant part $J_i = 30$ that do not correspond to resonances, neither from the final, nor from the initial continuum. If E_i, J_i are fixed, the values of $M_{E_i,J_i;E_f,J_f}$ oscillates because of the changes in the phase of the final wave function when E_f is changed [29]. The sum over J_i in Equation (1.116) goes up to $J_i = 56$ at this energy in order to obtain a convergence.

Because RCT is a free-free process, the sum should, in principle, include all the rotational quantum numbers. In practice, the infinite summation is approximated by a finite sum according to the required convergence of unchanging five digits with increasing J_i. The convergence is achieved at $J_i = 700$ at $E_i = 0.4$ eV,1 eV, $J_i = 900$ at $E_i = 5$ eV and $J_i = 1\,200$ at $E_i = 10$ eV. The partial cross sections at

Figure 2.24: The partial cross sections $\mathrm{d}\sigma/\mathrm{d}\omega_{if}$ of $HeLi^+$ are plotted at different initial collision energies: $E_i = 400$ meV, 1 eV, 5 eV, and 10 eV.

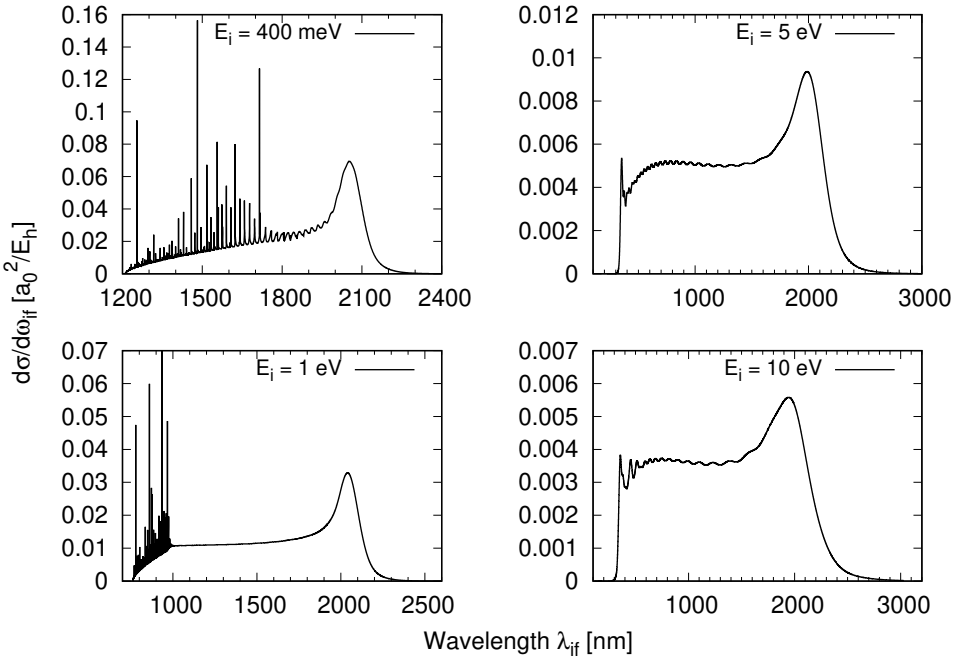

these energies are illustrated in Figure 2.24 as functions of wavelength of emitted photon. With increasing E_i, the partial cross sections achieve smaller values but larger range in wavelength. The resonance structure in $\mathrm{d}\sigma/\mathrm{d}\omega_{if}(E_i, \omega_{if})$ stems from the final continuum. The lack of the resonance structure in the right-hand panels is due to the short heights of resonance peaks at these collision energies. A kind of a "hump" is around 2 053 nm, 2 040 nm and 1 944 nm at $E_i = 0.7$ eV, 1 eV and 10 eV, respectively. Origin is nonresonant and stems from an interplay of phase differences of the wave functions at R where $d_z(R)$ is not negligible [80]. In [29] for HeH^+, the "hump" was at the wavelength corresponding to the energy difference of the dissociation limits. In our case, it is similar since $\Delta E = 5\,032.4$ cm^{-1}, which corresponds to $\lambda_{if} \approx 1\,987$ nm.

Figure 2.25 shows the resonances from the final continuum at 10 eV that cannot be seen in Figure 2.24 due to very low values of the resonance peaks. The heights of the peaks are decreasing with rising E_i as it can be seen in the multiplot. At 5 eV, they can be seen only after zooming in, which is the case also for 10 eV.

Cross Sections

The RCT cross sections are illustrated in Figure 2.26 [33]. A rich resonance structure is noticable up to around 0.05 eV from the initial continuum. With increasing E_i, the cross sections initially decrease but then in the nonresonant part they increase. This rise of the values are explained, for instance, in [81] on the semiclassical (SC) method for $NaHe^+$. In the SC method, RCT cross sections are obtained from Equation (1.109), which we have for RA. The only difference between RA and RCT SC theory is in the definition of Einstein coefficients $A_{0,0}(R)$. In Subsection 1.6.2, the focus is on free-bound transitions, while here it is on

Figure 2.25: Partial cross sections for $HeLi^+$ are plotted at 10 eV for low wavelengths with resonance structure.

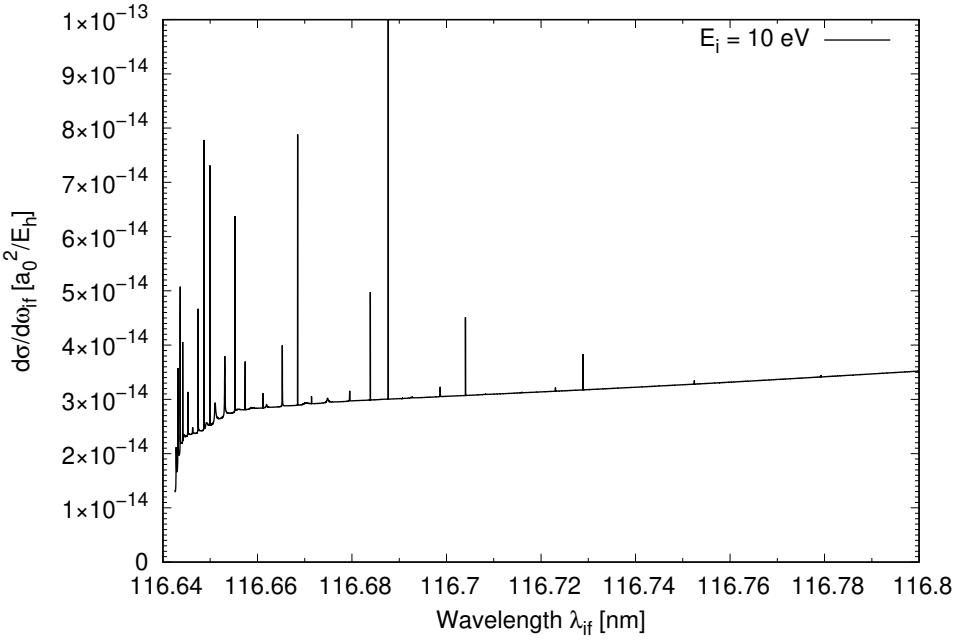

free-free transitions. In [81], $A_{0,0}(R)$ is plotted and it can be seen there a fast increase with decreasing R. This rise entails a faster rise of Equation (1.109) than the characteristic $\sigma(E_i) = C/\sqrt{E_i}$ behaviour for very large E_i. This is true for increase in E_i and, thus, also for decrease of the classical turning point of the initial state. As a result, the RCT cross sections increase. When the collision energy E_i is so large that the classical turning point is too small, the Einstein coefficient rapidly drops. As a consequence, the $\sigma(E_i) = C/\sqrt{E_i}$ behaviour prevails and the cross section decreases.

The threshold energy from which Equation (1.119) is valid for the b $\rightarrow$ a transition is around $E_i = 200\,000$ cm^{-1}. Then, $C = 3.399\,5 \times 10^{-18}$ cm$^{3/2}$. In order to achieve the convergence, $J_i = 1\,400$ is needed at these energies.

Rate Coefficients

The calculated rate coefficients with the individual contributions (background up to 200 000 cm^{-1}, $\alpha_{\mathrm{fin}}(T)$, and from 200 000 cm^{-1} with the asymptotic behaviour for $\sigma(E_i)$, $\alpha_{\mathrm{inf}}(T)$; then, from wide resonances, $\alpha_{\mathrm{w}}(T)$, and narrow resonances, $\alpha_{\mathrm{n}}(T)$) are illustrated in Figure 2.27 and summarised in Table 2.14 [33]. Resonance contribution is important mainly for low temperatures. In our case, the contribution from narrow resonances is at least one order smaller than from wide resonances. $\alpha_{\mathrm{inf}}(T)$ is negligible for low temperatures. It starts to contribute from temperatures around 50 000 K and becomes the most significant above 200 000 K. This is more obvious from Figure 2.27. The term $\alpha_{\mathrm{fin}}(T)$ contributes the most up to around 200 000 K. At this temperature, this term is already decreasing with increasing temperature. The term $\alpha_{\mathrm{inf}}(T)$, on the other hand, increases with increasing temperature and should converge to the asymptote 3.294×10^{-14} cm^3/s determined from Equation (1.121).

Figure 2.26: Radiative charge transfer cross sections of $HeLi^{+}i$ are plotted with depicted resonances that have their widths larger than 0.1 cm^{-1}. This Figure is taken from [33].

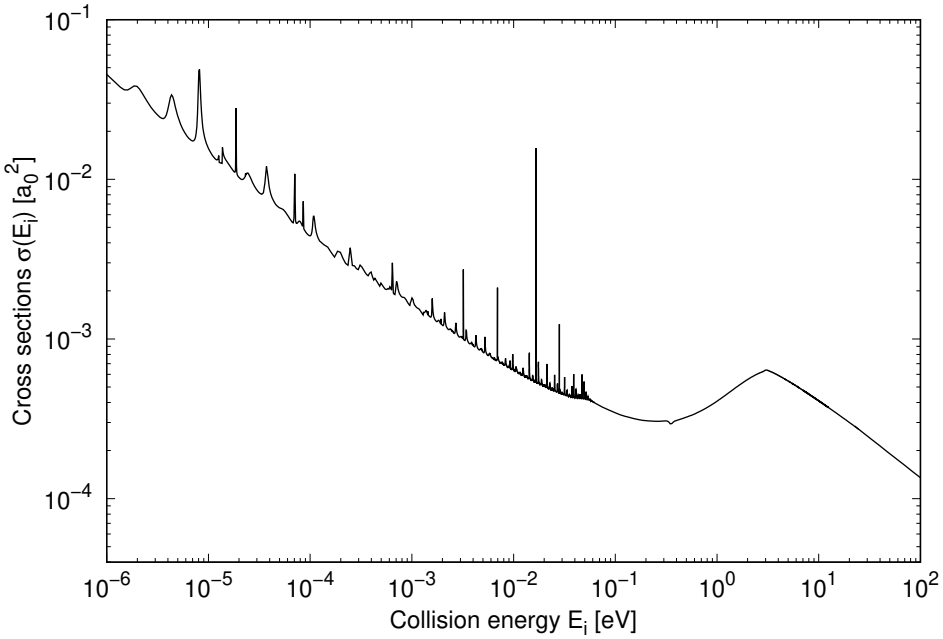

Figure 2.27: The radiative charge transfer rate coefficients for $HeLi^{+}$ are illustrated with the background and resonance contributions. The results were published in [33].

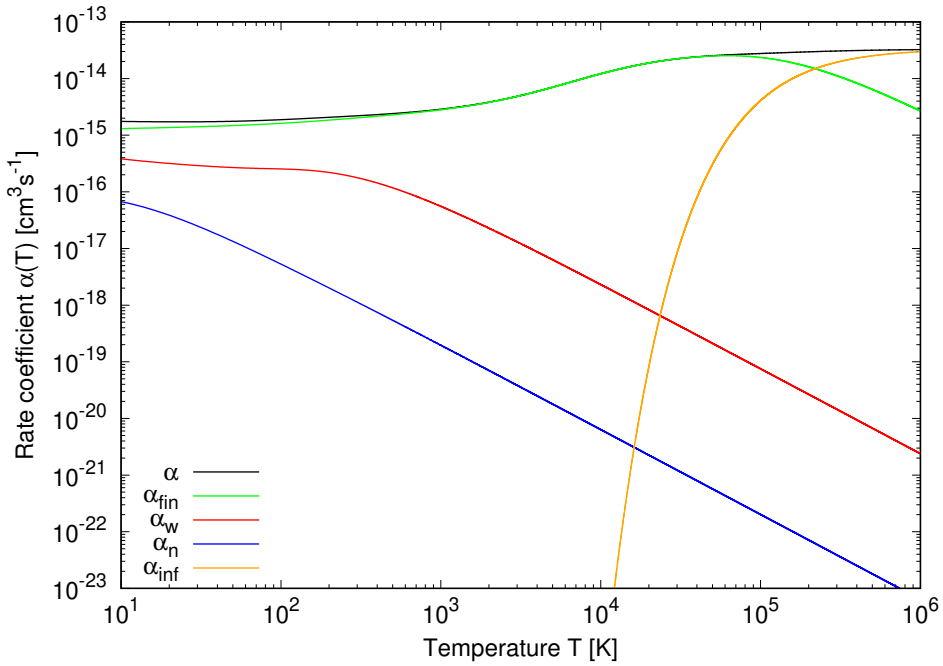

Table 2.14: The radiative charge transfer rate coefficients $\alpha(T)$ for $HeLi^+$ are summarised with their background and resonance contributions ($\alpha_{\rm fin}(T)$, $\alpha_{\rm w}(T)$, $\alpha_{\rm n}(T)$, and $\alpha_{\rm inf}(T)$) at selected temperatures. Temperature is given in K and rate coefficients in cm^3s^{-1}.[a] [33]

T	$\alpha_{\rm fin}$	$\alpha_{\rm w}$	$\alpha_{\rm n}$	$\alpha_{\rm inf}$	α
10	1.30(-15)	3.82(-16)	6.70(-17)	0	1.75(-15)
20	1.37(-15)	3.17(-16)	3.86(-17)	0	1.72(-15)
30	1.41(-15)	2.91(-16)	2.50(-17)	0	1.72(-15)
50	1.48(-15)	2.69(-16)	1.34(-17)	0	1.76(-15)
100	1.62(-15)	2.54(-16)	5.30(-18)	0	1.88(-15)
200	1.85(-15)	2.20(-16)	2.01(-18)	0	2.07(-15)
500	2.29(-15)	1.18(-16)	5.40(-19)	0	2.41(-15)
800	2.61(-15)	7.20(-17)	2.72(-19)	0	2.68(-15)
1 000	2.81(-15)	5.55(-17)	1.96(-19)	0	2.87(-15)
2 000	3.80(-15)	2.28(-17)	7.02(-20)	0	3.82(-15)
2 500	4.31(-15)	1.68(-17)	5.04(-20)	0	4.32(-15)
3 000	4.83(-15)	1.31(-17)	3.84(-20)	0	4.85(-15)
4 000	5.91(-15)	8.71(-18)	2.50(-20)	0	5.92(-15)
6 000	8.11(-15)	4.87(-18)	1.37(-20)	3.86(-34)	8.11(-15)
8 000	1.02(-14)	3.20(-18)	8.88(-21)	5.40(-29)	1.02(-14)
10 000	1.21(-14)	2.31(-18)	6.36(-21)	6.46(-26)	1.21(-14)
16 000	1.67(-14)	1.15(-18)	3.15(-21)	2.50(-21)	1.67(-14)
20 000	1.88(-14)	8.30(-19)	2.25(-21)	8.22(-20)	1.88(-14)
25 000	2.08(-14)	5.95(-19)	1.61(-21)	1.32(-18)	2.08(-14)
32 000	2.27(-14)	4.12(-19)	1.11(-21)	1.46(-17)	2.27(-14)
50 000	2.50(-14)	2.12(-19)	5.70(-22)	3.05(-16)	2.53(-14)
56 000	2.52(-14)	1.79(-19)	4.81(-22)	5.39(-16)	2.57(-14)
64 000	2.53(-14)	1.46(-19)	3.94(-22)	9.68(-16)	2.62(-14)
80 000	2.48(-14)	1.05(-19)	2.82(-22)	2.17(-15)	2.70(-14)
100 000	2.36(-14)	7.51(-20)	2.02(-22)	4.09(-15)	2.76(-14)
140 000	2.04(-14)	4.54(-20)	1.22(-22)	8.23(-15)	2.86(-14)
200 000	1.61(-14)	2.66(-20)	7.13(-23)	1.35(-14)	2.96(-14)
500 000	6.42(-15)	6.74(-21)	1.80(-23)	2.52(-14)	3.16(-14)

[a] $x(-y) \equiv x \times 10^{-y}$; $10^{-40} > \alpha_{\rm inf}(T) \equiv 0$

Conclusion

Radiative processes of astrochemical relevance were studied. Concretely:

- radiative lifetimes of ro-vibrational states of $HeLi^+(b^3\Sigma^+)$ [32],
- radiative association of $He(2^3P)$ in collisions with $Li^+(1^1S)$ [30, 31],
- radiative association of $O(2^3P)$ in collisions with $C^+(2^2P)$ [34, 64],
- and radiative charge transfer in collisions of $He(2^3S)$ with $Li^+(1^1S)$ [33]

were the subject of this thesis.

Radiative lifetimes of vibrational level $v = 0$ for $J = 0, 1, 2$ of $HeLi^+(b^3\Sigma^+)$ is 1.30×10^{-6} s. They increase with increasing v. For $J = 0$, the radiative lifetimes of $v = 0$ and $v = 32$ differ by two orders of magnitude. They differ for vibrational levels $v > 0$ for different J. The larger J is, the larger radiative lifetime becomes.

The radiative lifetimes were obtained as a sum of bound-bound

$$b^3\Sigma^+ \to a^3\Sigma^+ + \text{photon},$$

and bound-free transitions

$$b^3\Sigma^+ \to a^3\Sigma^+ \left[He(2^3P) + Li^+(1^1S)\right] + \text{photon}.$$

The bound-bound transitions contribute more to the total radiative width than the bound-free transitions; however, the bound-free contribution becomes more significant with increasing v.

Radiative association of $He(2^3P)$ in collisions with $Li^+(1^1S)$ involves eight processes

$$\begin{aligned}
c^3\Sigma^+ \left[He(2^3P) + Li^+(1^1S)\right] &\to HeLi^+(a^3\Sigma^+) + \text{photon},\\
&\to HeLi^+(b^3\Sigma^+) + \text{photon},\\
&\to HeLi^+(c^3\Sigma^+) + \text{photon},\\
&\to HeLi^+(1^3\Pi\ ) + \text{photon},\\
1^3\Pi\ \left[He(2^3P) + Li^+(1^1S)\right] &\to HeLi^+(a^3\Sigma^+) + \text{photon},\\
&\to HeLi^+(b^3\Sigma^+) + \text{photon},\\
&\to HeLi^+(c^3\Sigma^+) + \text{photon},\\
&\to HeLi^+(1^3\Pi\ ) + \text{photon}.
\end{aligned}$$

The cross sections and rate coefficients for spontaneous emission were obtained for all the listed processes. Up to around 200 K, the $1 \to a$ rate coefficient has the largest values. From 200 K, the $1 \to b$ rate coefficient exceeds it and becomes the most efficient radiative association process. The least efficient process is $1 \to 1$ and from 1 000 K the $c \to c$ rate coefficients have very similar values to the $1 \to 1$ values.

The rate coefficient for the depopulation of the continua of the $c^3\Sigma^+$ and $1^3\Pi$ states were calculated, too. The depopulation rate coefficient for the $1^3\Pi$

continuum is two or three orders of magnitude larger than for the $c^3\Sigma^+$ continuum. These processes could occur during the recombination era of the Universe. The temperature was expected to be from around 50 000 K at the beginning of the era and around 3 000 K at the end. The depopulation rate coefficient for the dissociation limit is equal to 1.18×10^{-13} cm^{3}s^{-1} at 3 000 K and 4.44×10^{-15} cm^{3}s^{-1} at 50 000 K, respectively. This means that at the end of the recombination era, the formation of the $HeLi^+$ molecular ion could be more efficient.

The spontaneous and stimulated cross sections were also calculated at several background temperatures for the $1 \rightarrow c$ process. The corresponding rate coefficients were calculated, too. The larger the background temperature, the more efficient the process becomes.

Radiative association of $O(2^3P)$ in collisions with $C^+(2^2P)$ involves seven processes

$$\begin{aligned}
A^2\Pi \ \left[O(2^3P) + C^+(2^2P)\right] &\rightarrow CO^+(X^2\Sigma^+) + \text{photon},\\
D^2\Pi \ \left[O(2^3P) + C^+(2^2P)\right] &\rightarrow CO^+(A^2\Pi\ ) + \text{photon},\\
&\rightarrow CO^+(X^2\Sigma^+) + \text{photon},\\
1^2\Sigma^- \left[O(2^3P) + C^+(2^2P)\right] &\rightarrow CO^+(A^2\Pi\ ) + \text{photon},\\
C^2\Delta \ \left[O(2^3P) + C^+(2^2P)\right] &\rightarrow CO^+(A^2\Pi\ ) + \text{photon},\\
X^2\Sigma^+ \left[O(2^3P) + C^+(2^2P)\right] &\rightarrow CO^+(A^2\Pi\ ) + \text{photon},\\
2^2\Sigma^- \left[O(2^3P) + C^+(2^2P)\right] &\rightarrow CO^+(A^2\Pi\ ) + \text{photon}.
\end{aligned}$$

The cross sections and rate coefficients for spontaneous emission were obtained for the all the above processes. The cross sections and rate coefficients were calculated also for two processes starting in an electronic state obtained by a quasidiabatic approximation, as we call it here. Those processes are

$$\begin{aligned}
\widetilde{D}^2\Pi \ \left[O(2^3P) + C^+(2^2P)\right] &\rightarrow CO^+(A^2\Pi\ ) + \text{photon},\\
&\rightarrow CO^+(X^2\Sigma^+) + \text{photon}.
\end{aligned}$$

Up to around 136 K, the $A \rightarrow X$ process has the largest rate coefficients. Between around 136 K and 16 700 K, the $\widetilde{D} \rightarrow A$ process is the most efficient process. At temperatures between 16 700 K and 24 200 K, $2 \rightarrow A$ achieves the largest rate coefficients among the other processes. At temperatures above 24 200 K, $\widetilde{D} \rightarrow X$ is the most efficient process. At the temperatures relevant for SN 1987A (between 2 000 K and 10 000 K), the rate coefficient for the depopulation of the continuum of $[O(2^3P) + C^+(2^2P)]$ are around one order of magnitude larger than those from [21], where they considered only the $A \rightarrow X$ channel [34]. It seems that the formation of CO^+ in SN 1987A is performed mainly through

$$CO + O^+ \rightarrow CO^+ + O,$$

which is preceded by a formation of CO by radiative association (discussed in Conclusions of [34]).

The radiative charge transfer cross sections and rate coefficients were calculated for this process

$$\mathrm{b}^3\Sigma^+\left[\mathrm{He}(2^3\mathrm{S}) + \mathrm{Li}^+(1^1\mathrm{S})\right] \rightarrow \mathrm{a}^3\Sigma^+\left[\mathrm{He}^+(1^2\mathrm{S}) + \mathrm{Li}(2^2\mathrm{S})\right] + \mathrm{photon}.$$

The rate coefficient is equal to 4.85×10^{-15} $\mathrm{cm}^3\mathrm{s}^{-1}$ and 2.53×10^{-14} $\mathrm{cm}^3\mathrm{s}^{-1}$ at 3 000 K and 50 000 K, respectively. This suggests that at the beginning of the recombination era, the radiative charge transfer was more efficient than the corresponding radiative association process

$$\mathrm{b}^3\Sigma^+\left[\mathrm{He}(2^3\mathrm{S}) + \mathrm{Li}^+(1^1\mathrm{S})\right] \rightarrow \mathrm{a}^3\Sigma^+ + \mathrm{photon},$$

which was studied in [71] and compared in [33]. At around 3 000 K the rate coefficients of radiative association and radiative charge transfer of the studied process have similar values [33]. Thus, at the end of the era, these two processes may have been comparable.

Bibliography

[1] COSMIC ESCAPES. Did the Universe start with a Big Bang? http://www.cosmicescapes.com/big-bang/. Accessed: 11/06/2019.

[2] M. A. Dopita and R. S. Sutherland. *Astrophysics of the Diffuse Universe*. Springer-Verlag Berlin Heidelberg, 1 edition, 2003. Section 7.6.

[3] P. Schneider. *Extragalactic Astronomy and Cosmology. An Introduction*. Springer-Verlag Berlin Heidelberg, 2 edition, 2015. Subsection 4.4.7.

[4] THECURIOUSASTRONOMER Life, the Universe, and everything. The temperature of the Universe at recombination (decoupling). https://thecuriousastronomer.wordpress.com/2016/06/13/the-temperature-of-the-universe-at-recombination-decoupling/. Accessed: 11/06/2019.

[5] A. Dalgarno. Molecular processes in the early universe. *Journal of Physics Conference Series*, 4:10–16, 2005.

[6] K. M. Ferrière. The interstellar environment of our galaxy. *Reviews of Modern Physics*, 73:1031–1066, 2001.

[7] D. Flower. *Molecular Collisions in the Interstellar Medium*. Cambridge University Press, The Edinburgh Building, Cambridge CB2 8RU, UK, 2 edition, 2007. Chapter 1.

[8] L. Augustovičová, V. Špirko, W. P. Kraemer, and P. Soldán. Radiative association of $LiHe^+$. *Chemical Physics Letters*, 531:59–63, 2012.

[9] M. Juřek, V. Špirko, and W. P. Kraemer. Ab initio determination of the rate coefficient for radiative assocation of $He(^1S)+H^+$. *Chemical Physics*, 193:287–296, 1995.

[10] W. P. Kraemer, V. Špirko, and M. Juřek. Formation of HeH^+ by radiative assocation of He^++H. *Chemical Physics Letters*, 236:177–183, 1995.

[11] L. Augustovičová, W. P. Kraemer, and P. Soldán. Depopulation of metastable helium $He(2^1S)$ by radiative association with hydrogen and lithium cations. *Journal of Quantitative Spectroscopy & Radiative Transfer*, 148:27–37, 2014.

[12] L. Augustovičová, W. P. Kraemer, and P. Soldán. Depopulation of metastable helium by radiative association with hydrogen and lithium ions. *The Astrophysical Journal*, 782:46–7, 2014.

[13] J. Loreau, S. Vranckx, M. Desouter-Lecomte, N. Vaeck, and A. Dalgarno. Photodissociation and radiative association of HeH^+ in the metastable triplet state. *The Journal of Physical Chemistry A*, 117:9486–9492, 2013.

[14] B. Zygelman, P. C. Stancil, and A. Dalgarno. Stimulated radiative association of He and H^+. *The Astrophysical Journal*, 508:151–156, 1998.

[15] L. Augustovičová, V. Špirko, W. P. Kraemer, and P. Soldán. Radiative association of He_2^+: the role of quartet states. *Monthly Notices of the Royal Astronomical Society*, 435:1541–1546, 2013.

[16] L. Augustovičová, V. Špirko, W. P. Kraemer, and P. Soldán. Radiative association of He_2^+ revisited. *Astronomy & Astrophysics*, 553:A42–5, 2013.

[17] L. Augustovičová. *Quantum Dynamics of Small Molecules.* PhD thesis, Charles University in Prague, 2014. Supervisor P. Soldán.

[18] B. T. Draine. *Physics of the Interstellar and Intergalactic Medium.* Princeton University Press, 41 William Street, Princeton, New Jersey 08540, 2011. Subsection 33.2.1.

[19] W. B. Latter, C. K. Walker, and P. R. Maloney. Detection of the carbon monoxide ion (CO^+) in the interstellar medion and planetary nebula. *The Astrophysical Journal*, 419:L97–L100, 1993.

[20] S. C. O. Glover, C. Federrath, M.-M. Mac Low, and R. S. Klessen. Modelling CO formation in the turbulent interstellar medium. *Monthly Notices of the Royal Astronomical Society*, 404:2–29, 2010.

[21] A. Dalgarno, M. L. Du, and J. H. You. The radiative association of C and O and C^+ and O. *The Astrophysical Journal*, 349:675–677, 1990.

[22] R. A. Gearhart, J. C. Wheeler, and D. A. Swartz. Carbon monoxide formation in SN 1987A. *The Astrophysical Journal*, 510:944–966, 1999.

[23] S. J. Petuchowski, E. Dwek, J. E. Jr. Allen, and J. A. III Nuth. CO formation in the metal-rich ejecta of SN 1987a. *The Astrophysical Journal*, 342:406–415, 1989.

[24] J. Franz, M. Gustafsson, and G. Nyman. Formation of carbon monoxide by radiative association: a quantum dynamical study. *Monthly Notices of the Royal Astronomical Society*, 414:3547–3550, 2011.

[25] M. Gustafsson and G. Nyman. Radiative association rate constant for the formation of CO: the importance of the first excited $^1\Sigma^+$ state. *Monthly Notices of the Royal Astronomical Society*, 448:2562–2565, 2015.

[26] S. V. Antipov, M. Gustafsson, and G. Nyman. Isotope effect in the formation of carbon monoxide by radiative association. *Monthly Notices of the Royal Astronomical Society*, 430:946–950, 2013.

[27] M. I. Chibisov, F. B. Yousif, P. J. T. van der Donk, and J. B. A. Mitchell. Radiative decay of the $HeH^+(b^3\Sigma^+)$ molecular ion. *Physical Review A*, 54:4997–5003, 1996.

[28] J. Loreau, J. Liévin, and N. Vaeck. Radiative lifetimes of the $a^3\Sigma^+$ state of HeH^+ from ab initio calculations. *The Journal of Chemical Physic*, 133:114302–7, 2010.

[29] B. Zygelman, A. Dalgarno, M. Kimura, and N. F. Lane. Radiative and nonradiative charge transfer in He^++H collisions at low energy. *Physical Review A*, 40:2340–2345, 1989.

[30] L. Augustovičová, M. Zámečníková, W. P. Kraemer, and P. Soldán. Radiative association of He(2^3P) with lithium cations. *Chemical Physics*, 462:65–70, 2015.

[31] M. Zámečníková, W. P. Kraemer, and P. Soldán. Radiative association of He(2^3P) with lithium cations: $\Pi \rightarrow \Sigma$ processes. *Journal of Quantitative Spectroscopy & Radiative Transfer*, 191:88–95, 2017.

[32] M. Zámečníková and P. Soldán. Radiative decay of $HeLi^+(b^3\Sigma^+)$. *Chemical Physics*, 500:1–6, 2018.

[33] M. Zámečníková, W. P. Kraemer, and P. Soldán. Radiative charge transfer between metastable helium and lithium cations. *The Astrophysical Journal*, 867:157–162, 2018.

[34] M. Zámečníková, P. Soldán, M. Gustafsson, and G. Nyman. Formation of CO^+ by radiative association. submitted to MNRAS, 2019.

[35] P. Soldán and J. M. Hutson. Near-dissociation states and coupled potential curves for the HeN^+ complex. *The Journal of Chemical Physics*, 117(7):3109–3119, 2002.

[36] J. Zamastil and J. Benda. *Quantum Mechanics and Electrodynamics*. Springer, 2017.

[37] V. Kapsa. Lecture notes to Teoretické základy molekulární spektroskopie. Unpublished, 2013.

[38] H. Haken. *Quantum Field Theory of Solids*. North-Holland Physics Publishing, 2 edition, 1983.

[39] NIST: National Institute of Standards and Technology. The NIST reference on constants, units, and uncertainty. Fundamental physics constants. https://physics.nist.gov/cgi-bin/cuu/Value?e. Accessed: 27/06/2019.

[40] H. Lefebvre-Brion and R. W. Field. *The Spectra and Dynamics of Diatomic Molecules*. Elsevier Academic Press, 525 B Street, Suite 1900, San Diego, CA 92101-4495, USA, 2004. Sections 3.1 and 3.2.

[41] J. Z. H. Zhang. *Theory and Application of Quantum Molecular Dynamics*. World Scientific Publishing Co. Pte. Ltd., 1999.

[42] I. G. Kaplan. *Intermolecular Interactions: Physics Picture, Computational Methods and Model Potentials*. John Wiley & Sons, Ltd, 2006.

[43] A. J. Stone. *The Theory of Intermolecular Forces*. Oxford University Press Inc., New York, 2002.

[44] A. Szabó and N. S. Ostlund. *Modern Quantum Chemistry (Introduction to Advanced Electronic Structure Theory)*. New York: Dover Publications, Inc., 2 edition, 1996.

[45] Bjoern O. Roos, editor. *Lecture Notes in Quantum Chemistry: European Summer School in Quantum Chemistry*. Berlin: Springer-Verlag, 1992.

[46] B. V. Numerov. Méthode nouvelle de la détermination des orbites et le calcul des éphémé rides en tenant compte des perturbations. *Trudy Glavnoi Rossiiskoi Astrofizicheskoi Observatorii*, 2:188–202, 1923.

[47] J. W. Cooley. An improved eigenvalue corrector formula for solving the Schroedinger equation for central fields. *Mathematics of Computations*, 15:363–374, 1961.

[48] G. Nyman, M. Gustafsson, and S. V. Antipov. Computational methods to study the formation of small molecules by radiative association. *International Reviews in Physical Chemistry*, 34:385–428, 2015.

[49] R. J. Le Roy. *LEVEL 7.7: A computer program for solving the radial Schroedinger equation*. University of Waterloo, Waterloo, Ontario N2L 3G1, Canada, Chemical Physics Research Report - 661 edition, 2005.

[50] M. Agúndez and V. Wakelam. Chemistry of dark clouds: Databases, networks, and models. *Chemical Reviews*, 113:8710–8737, 2013.

[51] P. C. Stancil and A. Dalgarno. Stimulated radiative association of Li and H in the early universe. *The Astrophysical Journal*, 479:543–546, 1997.

[52] S. Kotochigova and E. Tiesinga. Ab initio relativistic calculation of the RbCs molecule. *The Journal of Chemical Physics*, 123:174304–11, 2005.

[53] L. I. Schiff. *Quantum Mechanics*. McGraw-Hill Book Company, 3 edition, 1968. Page 336.

[54] R. A. Bain and J. N. Bardsley. Shape resonances in atom-atom collisions. I. Radiative association. *Journal of Physics B: Atomic and Molecular Physics*, 5:277–285, 1972.

[55] O. J. Bennett, A. S. Dickinson, T. Leininger, and F. X. Gadéa. Radiative association in Li+H revisited: the role of quasi-bound states. *Monthly Notices of the Royal Astronomical Society*, 341:361–368, 2003.

[56] G. Breit and E. Wigner. Capture of slow neutrons. *Physical Review*, 49:519–531, 1936.

[57] B. Zygelman and A. Dalgarno. Radiative quenching of He(2^1S) induced by collisions with ground-state helium atoms. *Physical Review A*, 38:1877–1884, 1988.

[58] J. R. Taylor. *Scattering Theory. The Theory of Nonrelativistic Collisions*. Dover Publications, Inc., 1 edition, 2006. Section 3-c.

[59] P. C. Stancil and B. Zygelman. Radiative charge transfer in collisions of Li with H^+. *The Astrophysical Journal*, 472:102–107, 1996.

[60] T.-S. Ho and H. Rabitz. A general method for constructing multidimensional molecular potential energy surfaces from ab initio calculations. *The Journal of Chemical Physics*, 104(7):2584, 1996.

[61] P. Soldán and J. M. Hutson. On the long-range and short-range behavior of potentials from reproducing kernel hilbert space interpolation. *The Journal of Chemical Physics*, 112(9):4415, 2000.

[62] T.-S. Ho and H. Rabitz. Proper construction of ab initio global potential surfaces with accurate long-range interactions. *The Journal of Chemical Physics*, 113(10):3960, 2000.

[63] R. J. Le Roy. *LEVEL 8.0: A computer program for solving the radial Schroedinger equation for Bound and Quasibound Levels*. University of Waterloo, Waterloo, Ontario N2L 3G1, Canada, Chemical Physics Research Report - 663 edition, 2007.

[64] M. Zámečníková, P. Soldán, M. Gustafsson, and G. Nyman. Formation of CO^+ by radiative association II. in preparation, 2019.

[65] W. H. Press, S. A. Teukolsky, W. T. Vetterling, and B. P. Flannery. *Numerical Recipes in Fortran 77. The Art of Scientific Computing*, volume 1. Cambridge University Press, 40 West 20th Street, New York, NY 10011-4211, USA, 2 edition, 1992. Chapter 4.

[66] E. W. Weisstein. Newton-Cotes formulas. From MathWorld–A Wolfram web source. http://mathworld.wolfram.com/Newton-CotesFormulas.html. Accessed: 27/02/2019.

[67] J. K. G. Watson. Hönl-London factors for multiplet transitions in Hund's case *a* or *b*. *Journal of Molecular Spectroscopy*, 252:5–8, 2008.

[68] L. Augustovičová. Radiative association of atoms. Master's thesis, Czech Technical University in Prague, 2011. Supervisor P. Soldán.

[69] P. Soldán and W. P. Kraemer. Molecular ion $LiHe^+$: ab initio study. *Chemical Physics*, 393:135–139, 2012.

[70] K. Okada and S. Iwata. Accurate potential energy and transition dipole moment curves for several electronic states of CO^+. *The Journal of Chemical Physics*, 112(4):1804–1808, 2000.

[71] L. Augustovičová, W. P. Kraemer, and P. Soldán. Depopulation of metastable helium by radiative association with hydrogen and lithium ions. *The Astrophysical Journal*, 782:46–52, 2014.

[72] Z.-C. Yan and J. F. Babb. Long-range interactions of metastable helium atoms. *Physical Review A*, 58(2):1247–1252, 1998.

[73] L. W. Wansbeek, B. K. Sahoo, R. G. E. Timmermans, B. P. Das, and D. Mukherjee. Ab initio determination of polarizabilities and van der waals coefficients of Li atoms using the relativistic coupled-cluster method. *Physical Review A*, 78(2):012515–7, 2008.

[74] NIST: National Institute of Standards and Technology. NIST Atomic spectra database levels. https://physics.nist.gov/PhysRefData/ASD/levels_form.html. Accessed: 04/12/2015.

[75] S. Bovino, M. Tacconi, and F. A. Gianturco. Photon-induced evolutionary rates of $LiHe^+(^1\Sigma^+)$ in early Universe from accurate quantum computations. *The Astrophysical Journal*, 740:101–108, 2011.

[76] A. S. Dickinson. Radiative association of H and D. *Journal of Physics B: Atomic and Molecular Physics*, 38:4329–4334, 2005.

[77] M. Gustafsson, S. V. Antipov, J. Franz, and G. Nyman. Refined theoretical study of radiative association: Cross sections and rate constants for the formation of SiN. *The Journal of Chemical Physics*, 137:104301–7, 2012.

[78] S. K.-M. Svensson, M. Gustafsson, and G. Nyman. Formation of the hydroxyl radical by radiative association. *The Journal of Physical Chemistry A*, 119:12263–12269, 2015.

[79] J. Tennyson. *Astronomical Spectroscopy.* World Scientific Publishing Co. Pte. Ltd., 2 edition, 2011.

[80] L. B. Zhao, P. C. Stancil, J. P. Gu, H.-P. Liebermann, Y. Li, P. Funke, R. J. Buenker, and B. Zygelman. Radiative charge transfer in collisions of O with He^+. *The Astrophysical Journal*, 615:1063–1072, 2004.

[81] C. H. Liu, Y. Z. Qu, B. J. Xiao, C. H. Zhou, J. G. Wang, and R. J. Buenker. Radiative charge transfer and radiative association in He^++Na collisions. *Physics Review A*, 81:022717–7, 2010.

[82] NIST: National Institute of Standards and Technology. Fundamental physical constants. Search results matching "atomic units"... . https://physics.nist.gov/cgi-bin/cuu/Results?search_for=atomic+unit. Accessed: 08/07/2019.

List of Abbreviations

BB - bound-bound (transition)
BF - bound-free (transition)
BO - Born-Oppenheimer (approximation)
BW - Breit-Wigner (theory)
DM(s) - dipole moment(s)
DVR - Discrete variable representation
FC - Franck-Condon (overlaps)
ISM - interstellar medium
PEC(s) - potential energy curve(s)
PT - perturbation theory
QM - quantum-mechanical (approach) or quantum mechanics
RA - radiative association
RCT - radiative charge transfer
RP-RKHS - reciprocal-power reproducing kernel Hilbert space
RLT(s) - radiative lifetime(s)
SC - semiclassical (method)
SLA - spinless approximation
TDM(s) - transition dipole moment(s)

Conversions of Atomic Units

The conversion factors are taken from [82].

$1\ E_\mathrm{h} = 4.359\,744\,650 \times 10^{-18}$ J
$1\ a_0 = 5.291\,772\,109\,03 \times 10^{-11}$ m
$1\ m_e = 9.109\,383\,701\,5 \times 10^{-31}$ kg
$1\ e = 1.602\,176\,634 \times 10^{-19}$ C
$1\ ea_0 = 8.478\,353\,625\,5 \times 10^{-30}$ Cm
$1\ e^2a_0^2/E_\mathrm{h} = 1.648\,777\,274\,36 \times 10^{-41}$ $\mathrm{C^2m^2J^{-1}}$
$1\ \hbar/E_\mathrm{h} = 2.418\,884\,326\,585\,7 \times 10^{-17}$ s

List of publications

Lucie Augustovičová, Martina Zámečníková, Wolfgang P. Kraemer, and Pavel Soldán. Radiative association of He(2^3P) with lithium cations. *Chemical Physics*, 462:65-70, 2015.

Martina Zámečníková, Wolfgang P. Kraemer, and Pavel Soldán. Radiative association of He(2^3P) with lithium cations: $\Pi \rightarrow \Sigma$ processes. *Journal of Quantitative Spectroscopy & Radiative Transfer*, 191:88-95, 2017.

Martina Zámečníková, and Pavel Soldán. Radiative decay of $HeLi^+(b^3\Sigma^+)$. *Chemical Physics*, 500: 1-6, 2018.

Martina Zámečníková, Wolfgang P. Kraemer, and Pavel Soldán. Radiative charge transfer between metastable helium and lithium cations. *The Astrophysical Journal*, 867:157-162, 2018.

Martina Zámečníková, Pavel Soldán, Magnus Gustafsson, and Gunnar Nyman. Formation of CO^+ by radiative association. *Monthly Notices of the Royal Astronomical Society*, 2019, submitted.

Martina Zámečníková, Pavel Soldán, Magnus Gustafsson, and Gunnar Nyman. Formation of CO^+ by radiative association II. In preparation.